PGD-TO: A Scalable Alternative to MMA Using Projected Gradient Descent for Multi-Constraint Topology Optimization

Amin Heyrani Nobari^{1*} and Faez Ahmed¹

¹Department of Mechanical Engineering, Massachusetts Institute of Technology, 77 Massachusetts Ave., Cambridge, 02139, MA, USA.

*Corresponding author(s). E-mail(s): ahnobari@mit.edu;

Abstract

Projected Gradient Descent (PGD) methods offer a simple and scalable approach to topology optimization (TO), yet they often struggle with nonlinear and multi-constraint problems due to the complexity of active-set detection. This paper introduces PGD-TO, a framework that reformulates the projection step into a regularized convex quadratic problem, eliminating the need for active-set search and ensuring well-posedness even when constraints are infeasible. The framework employs a semismooth Newton solver for general multi-constraint cases and a binary search projection for single or independent constraints, achieving fast and reliable convergence. It further integrates spectral step-size adaptation and nonlinear conjugate-gradient directions for improved stability and efficiency. We evaluate PGD-TO on four benchmark families representing the breadth of TO problems: (i) minimum compliance with a linear volume constraint, (ii) minimum volume under a nonlinear compliance constraint, (iii) multi-material minimum compliance with four independent volume constraints, and (iv) minimum compliance with coupled volume and center-ofmass constraints. Across these single- and multi-constraint, linear and nonlinear cases, PGD-TO achieves convergence and final compliance comparable to the Method of Moving Asymptotes (MMA) and Optimality Criteria (OC), while reducing per-iteration computation time by 10-43x on general problems and 115-312x when constraints are independent. Overall, PGD-TO establishes a fast, robust, and scalable alternative to MMA, advancing topology optimization toward practical large-scale, multi-constraint, and nonlinear design problems. Public code available at: https://github.com/ahnobari/pyFANTOM

Keywords: Topology Optimization, Projected Gradient Descent, Minimum Compliance, Nonlinear Optimization

1 Introduction

With the advent of large computational capacity and modern manufacturing capabilities, most notably additive manufacturing, the optimal geometric/topological design of parts and structures under different physics-based and geometric constraints and objectives has emerged as a prominent problem in computational design. Specifically, the problem of structural Topology Optimization (TO) aims to optimally distribute material in a physical domain to maximize performance with respect to some physical or geometric objective while adhering to constraints. In many TO approaches, the search problem is solved using gradient-based optimization methods that rely on Finite Element Analysis (FEA), which can be expensive in high-fidelity scenarios. Beyond the expensive simulations, the nonlinear and often nonconvex nature of the problem makes it challenging to solve efficiently; many nonlinear optimizers incur high computational costs in high-fidelity settings. Several efforts have been made to introduce different

algorithms for TO. The most popular among these efforts are the Method of Moving Asymptotes (MMA) [1] and Optimality Criteria (OC) [2]. Despite their popularity, these approaches suffer from a few drawbacks, such as lack of generalizability to multiple constraints in OC and a large number of optimizer parameters in MMA complicating the overall process, which have given rise to many alternative algorithms such as Sequential Linear Programming (SLP) [3], Sequential Quadratic Programming (SQP) [4], or Interior Point Method (IPM) [5]. Recently, however, many have focused on Projected Gradient Descent (PGD) methods for topology optimization [6–8]. With a much simpler overall approach and computational efficiency, PGD has promising features that make it a great choice for TO problems.

However, PGD can become problematic in many situations. For example, nonlinear geometric constraints such as overhang angle constraints [9–11] in TO problems can cause PGD to become unstable or converge poorly. Moreover, projected gradient descent approaches often handle a single constraint relatively efficiently, yet they face a complexity issue when faced with multiple constraints. This stems from the fact that a general convex Quadratic Program (QP) arises in the projection step, which can be costly to solve, requiring potentially computationally intensive algorithms just to solve the projection itself. Some efforts have been made to solve this problem more efficiently using sophisticated active set methods [8, 12, 13], which focus on quickly finding the active constraints in a problem and solving the projection problem based on this information. Recently, Barbeau et al. [8] proposed using the active set method specifically in TO problems. However, switching among active sets during projection remains a limitation and increases complexity for multi-constraint problems. Moreover, the PGD approach has yet to be thoroughly tested on complex problems with multiple nonlinear constraints and to be made robust to them.

Given these limitations in PGD, considering the potential for PGD as a highly scalable and much faster **general** TO platform, we develop a scalable, efficient framework for applying PGD in TO problems and show that this approach scales much better than existing general TO optimizers while exhibiting similar convergence. In our work, we introduce a PGD optimizer, which analyzes many different aspects of the optimization to introduce robustness heuristics as well as advanced optimization techniques such as nonlinear conjugate gradient and spectral step size adjustment to improve PGD for TO and make the overall optimizer robust. Most notably, we overcome the active-set search required for PGD by exploring a regularized sub-problem and demonstrate that this sub-problem exhibits properties that enable us to solve the projection problem without any active-set search, using a semi-smooth Newton iteration method with superlinear convergence, which makes the solutions to the projection sub-problem expeditious. We then test this approach in a slew of test problems to benchmark the algorithm in tough and complex nonlinear scenarios and demonstrate how the optimizers remain robust even in challenging problems and impressively perform on par with the commonly used quadratic MMA solver.

Contributions.

This work advances the use of PGD for topology optimization through a general, efficient, and theoretically grounded framework. Its key contributions are:

- Active-set-free projection. We solve the projection step as a strictly convex, always-feasible quadratic program with slack variables. This removes the need for active-set detection and guarantees a unique projection solution, enabling stable and scalable constrained optimization.
- Unified projection solvers. The framework employs a semismooth Newton method for general multi-constraint problems. It leverages the Symmetric Positive Definite (SPD) Jacobian for superlinear local convergence and a binary-search algorithm for projection in single or independent constraints, providing substantial computational savings.
- Theoretically supported PGD algorithm. We use insights from the $\mathcal{O}(1/\sqrt{K})$ convergence rate and analysis of PGD for automatic step-size relaxation with linearized constraints in our overall framework, and integrate spectral step-size adaptation without line search, and Polak-Ribiére nonlinear conjugate gradient directions to improve convergence behaviour.
- Empirical validation at scale. Across four benchmark TO problems shown in Fig. 1 encompassing linear, nonlinear, and multi-constraint scenarios, the proposed method achieves accuracy comparable to MMA and OC while reducing per-iteration computation by one to two orders of magnitude. Code and benchmarks are publicly available.

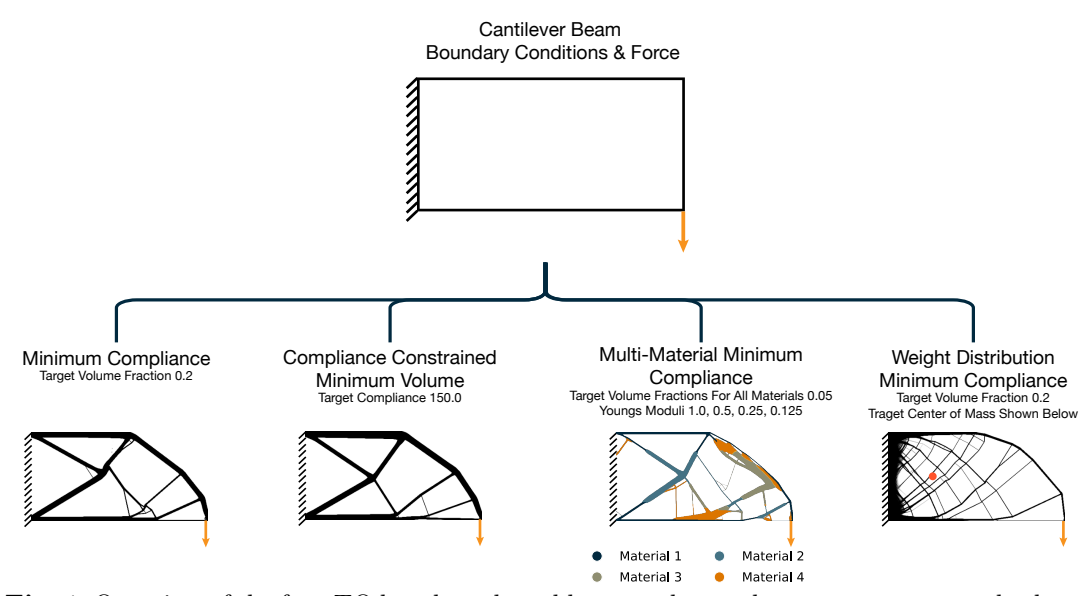


Fig. 1: Overview of the four TO benchmark problems used to evaluate convergence and robustness across solvers. Each problem is solved at three mesh resolutions, with detailed results provided in Appendix A.5.

2 Background & Related Works

In this section, we will briefly discuss the scope of the TO problems we tackle, formulate the general problem concretely, and discuss some related works and nonlinear optimizers that have been developed for a similar class of problems.

2.1 Formalizing The Topology Optimization Problems

Structural topology optimization (TO) seeks the optimal distribution of material within a prescribed design domain to maximize or minimize a given physics-based or geometric performance metric, subject to a set of constraints. A common formulation of TO operates over a continuous domain, which is the focus of this work. Let $\bar{\Omega} \subset \mathbb{R}^d$ represent a bounded design domain with boundary $\Gamma = \partial \bar{\Omega}$. In these approaches, a material density field, $\rho(x): \bar{\Omega} \to \{0,1\}$, becomes the design we seek to optimize. While an ideal binary solution yields a clear structural layout, obtaining such discrete solutions directly is computationally intractable. Thus, a more relaxed mapping, $\rho(x): \bar{\Omega} \to [0,1]$, is used where the density values represent the amount of material in a given part of the domain. This continuous representation requires evaluating physical and geometric responses over $\bar{\Omega}$, typically governed by partial differential equations describing the relevant physics. Because these PDEs rarely admit closed-form solutions for arbitrary domains, TO algorithms usually employ a discretized approximation and solve the governing equations via finite element analysis (FEA). In its general discrete form, the topology optimization problem can be written as:

$$\min_{\boldsymbol{\rho} \in R^{N}} f(\boldsymbol{\rho})$$
s.t. $l \le \rho_{i} \le u, \quad \forall i \in [N]$

$$g_{j}(\boldsymbol{\rho}) \le G_{j} \quad \forall j \in [m],$$

$$(1)$$

Where $\rho \in \mathbb{R}^n$ represents the N design variables (for a discretized domain mesh with N elements) and l and u are the bounds on the design variables and f is a general linear or nonlinear function of the design variables (e.g. $\mathbf{f}^T \mathbf{K}^{-1}(\rho) \mathbf{f}$ in minimum compliance, where $K(\rho)$ is the FEA stiffness matrix and f is the forcing term), and g_j are linear or nonlinear functions of the design variable with upper bound G_j (e.g. $\sum_{i=1}^N A_i \rho_i \leq V$ for volume constraint in many TO problems).

This general formulation makes no assumptions about the form of f or g_j beyond their dependence on the design variables and the presence of simple bounds on ρ_i . Equality constraints can be accommodated within the same framework and are omitted here only for brevity.

2.2 Nonlinear Optimizers For TO

Many prior works have focused on solving specific TO problems where the particular problem involves a specific structure or a single constraint (e.g., only volume constraint). A popular example of this is the optimality criteria approach developed for solving problems with only design variable bounds and a single volume constraint [14]. More general approaches, such as Sequential Linear Programming (SLP) [3], Sequential Quadratic Programming (SQP) [4], or Interior Point Method (IPM) [5] have attempted to tackle the general problem in (1).

Among these, the *Method of Moving Asymptotes* (MMA) [1] has emerged as the most widely used optimizer in TO due to its scalability and robustness across large problem instances [15, 16]. Despite its success, MMA requires the solution of a subproblem that involves updating asymptotes for all design variables. As a result, its computational complexity scales primarily with the number of design variables, rather than with the typically smaller number of constraints. In contrast, the OC method is more efficient in single-constraint settings, since it reduces the optimization to a dual problem with only one dual variable. However, MMA also demands careful tuning of multiple algorithm-specific hyperparameters, which can make setup and convergence control cumbersome in practice.

More recently, *Projected Gradient Descent* methods have gained attention as promising alternatives for TO due to their simplicity and favorable computational scaling, especially in large-scale or single-constraint problems [6–8]. The most recent advance by Barbeau et al. [8] extends PGD to multi-constraint TO problems using a modified active-set projection strategy. While effective, active-set-based projections can be difficult to solve and may lead to slow or cyclic convergence when the active set changes frequently.

In this work, we propose a different approach: a regularized projection formulation that eliminates the need for active-set identification entirely. Our method solves the projection subproblem directly through a convex regularization scheme, resulting in improved robustness and scalability—particularly for problems with a small number of nonlinear constraints.

3 Projected Gradient Descent For Topology Optimization

This section details the proposed Projected Gradient Descent framework for topology optimization and motivates our formulation's design choices.

3.1 Projected Gradient Descent

Given the general formulation of the problem in (1), we will now formulate the projected gradient descent optimization approach for this problem. In projected gradient descent, we would compute the gradients of the objective function and take a step in that direction, and project the resulting design variables onto the feasible subset of \mathbb{R}^N . Let $\Pi_{\Omega}(\tilde{\boldsymbol{\rho}})$ be the projection operator that projects any given $\tilde{\boldsymbol{\rho}} \in \mathbb{R}^N$ onto the feasible set $\Omega \triangleq \{\boldsymbol{\rho} \mid l \leq \boldsymbol{\rho} \leq u, g_j(\boldsymbol{\rho}) \leq G_j \quad \forall j \in [m]\} \subseteq \mathbb{R}^N$, then the update rule for projected gradient descent will be:

$$\boldsymbol{\rho}_{t+1} = \Pi_{\Omega} \left(\boldsymbol{\rho}_t - \alpha \nabla f \right). \tag{2}$$

If the projection operator Π_{Ω} can be evaluated efficiently, this scheme provides a simple and scalable method for solving a wide range of TO problems. Moreover, the framework naturally accommodates alternative descent directions or acceleration schemes, such as momentum, conjugate gradients, or spectral updates, making PGD a versatile approach for nonlinear constrained optimization. In this work, we focus on the practically relevant regime where the number of constraints $m \ll N$ is much smaller than the number of design variables. Under this assumption, we introduce an efficient and robust formulation for solving the projection subproblem, which serves as the key computational component of our PGD-based topology optimization framework.

3.2 Solving The Projection Problem

To formulate the projection problem, let's start with an updated design variable set/vector $\tilde{\boldsymbol{\rho}} = \boldsymbol{\rho}_t - \alpha \nabla f(\boldsymbol{\rho}_t)$, which is obtained by performing a gradient descent update on the design variables. Let $\boldsymbol{\delta}$ be an adjustment vector which, when added to $\tilde{\boldsymbol{\rho}} \notin \Omega$, will bring it into the feasible set Ω . We can formulate the projection problem in Euclidean projection as:

$$\min_{\boldsymbol{\delta} \in \mathbb{R}^{N}} \quad \|\tilde{\boldsymbol{\rho}} + \boldsymbol{\delta} - \tilde{\boldsymbol{\rho}}\|_{2}^{2} = \|\boldsymbol{\delta}\|_{2}^{2}$$
s.t.
$$l \leq \tilde{\rho}_{i} + \delta_{i} \leq u, \quad \forall i \in [N]$$

$$g_{j}(\tilde{\boldsymbol{\rho}} + \boldsymbol{\delta}) \leq G_{j} \quad \forall j \in [m],$$
(3)

The problem in (3) is a strictly convex quadratic program with a convex objective. However, the feasible set Ω may not be convex or even non-empty, which complicates direct computation. To address this, we adopt a simplification inspired by Sequential Linear Programming methods commonly used in topology optimization. Specifically, we linearize the nonlinear constraint functions locally, assuming that both the gradient descent update and the projection adjustment are small.

$$\|\alpha \frac{\partial f}{\partial \rho_t}\| \ll \|\rho_t\|, \qquad \|\delta\| \ll \|\rho_t\|.$$

Under these conditions, it is reasonable to approximate nonlinear constraints using their first-order Taylor expansion around ρ_t . This assumption is particularly valid near local optima, where convergence behavior is stable and step sizes are small.

Applying this linearization yields the following simplified projection subproblem:

$$\min_{\boldsymbol{\delta} \in \mathbb{R}^{N}} \quad \|\boldsymbol{\delta}\|_{2}^{2}$$
s.t. $l \leq \tilde{\rho}_{i} + \delta_{i} \leq u, \quad \forall i \in [N]$

$$g_{j}(\boldsymbol{\rho}_{t}) + (\boldsymbol{\delta} - \alpha \nabla f(\boldsymbol{\rho}_{t}))^{T} \nabla g_{j}(\boldsymbol{\rho}_{t}) \leq G_{j} \quad \forall j \in [m],$$
(4)

This formulation leads to a convex QP with a linear constraint set, which we will show can be solved in an efficient manner in most cases. We can do this by analyzing the optimality conditions of the above problem. The key insight we achieve by analyzing the optimality criterion is the fact that the solution to the projection problem only depends on a small number, m, of dual parameters. Theorem 1 characterizes the form of this solution.

Theorem 1 (Solution to the Linearized Projection Problem) Let the linearized projection problem be defined as in (4). A vector $\boldsymbol{\delta}^* \in \mathbb{R}^N$ is the unique optimal solution to this problem if and only if there exists a unique vector of dual variables $\mathbf{y}^* \in \mathbb{R}^m$ satisfying $\mathbf{y}^* \leq \mathbf{0}$, such that for all $i \in \{1, ..., N\}$:

$$\delta_{i}^{*} = \begin{cases} l - \tilde{\rho}_{i} & \text{if } \sum_{j} y_{j}^{*}(\nabla g_{j}(\boldsymbol{\rho_{t}}))_{i} < l - \tilde{\rho}_{i}, \\ \sum_{j} y_{j}^{*}(\nabla g_{j}(\boldsymbol{\rho_{t}}))_{i} & \text{if } l - \tilde{\rho}_{i} \leq \sum_{j} y_{j}^{*}(\nabla g_{j}(\boldsymbol{\rho_{t}}))_{i} \leq u - \tilde{\rho}_{i}, \\ u - \tilde{\rho}_{i} & \text{if } \sum_{j} y_{j}^{*}(\nabla g_{j}(\boldsymbol{\rho_{t}}))_{i} > u - \tilde{\rho}_{i}, \end{cases}$$

$$(5)$$

and for all $j \in \{1, \ldots, m\}$:

$$g_j(\tilde{\boldsymbol{\rho}}) + (\boldsymbol{\delta} - \alpha \nabla f(\boldsymbol{\rho}_t))^T \nabla g_j(\tilde{\boldsymbol{\rho}}) \le G_j$$
 (6)

$$y_j \left(g_j(\tilde{\boldsymbol{\rho}}) + (\boldsymbol{\delta} - \alpha \nabla f(\boldsymbol{\rho}_t))^T \nabla g_j(\tilde{\boldsymbol{\rho}}) - G_j \right) = 0$$
 (7)

Proof The proof follows directly from the KKT conditions, derived in detail in Appendix A. The expressions for δ^* and \mathbf{y}^* , along with their feasibility conditions, are exact restatements of the KKT optimality system for this convex problem.

The notable observation that emerges is how the constraint functions behave with respect to the dual variables, \mathbf{y} , which we will detail in the following sections, and discuss how we can solve the projection problem efficiently in different scenarios.

3.2.1 Solving Problems With A Single Constraint

Many TO problems involve only a single constraint, most commonly a volume constraint, a single stress constraint, or a compliance constraint. In such cases, the optimization problem in (4) reduces to a single constraint, and therefore, only one dual variable y appears in the KKT system.

It can be shown that for this case, the linearized constraint function

$$g(\tilde{\boldsymbol{\rho}}) + (\boldsymbol{\delta} - \alpha \nabla f(\boldsymbol{\rho}_t))^T \nabla g(\tilde{\boldsymbol{\rho}})$$

is a monotone non-decreasing function of the dual variable y (see Appendix A.1). This monotonicity property enables an efficient solution of the projection subproblem through a one-dimensional binary search.

If the constraint is inactive, then a value of y = 0 will yield a valid solution; thus, in our algorithm, we start by checking if this is the case, and if not, we perform a binary search to find y^* such that the constraint is met at equality. Algorithm 1, shows how this binary search can be performed to find the optimal projection for the linearized problem.

Algorithm 1 Single Constraint Projection Binary Search

```
Require: \tilde{\boldsymbol{\rho}}, \nabla \mathbf{g}(\boldsymbol{\rho}_t), tol, l, u
  1: if \delta(0) is feasible then
             y^* = 0
  2:
             Return y^*
  3:
  4:
             y_l = \min_i \left\{ \min \left( \frac{l - \tilde{\rho}_i}{(\nabla g(\boldsymbol{\rho}_t))_i}, \frac{u - \tilde{\rho}_i}{(\nabla g(\boldsymbol{\rho}_t))_i} \right) \right\}
  5:
  6:
             y_m = \frac{y_u + y_l}{2}
  7:
              while |y_u - y_l| > \text{tol do}
  8:
                    if (\delta(y) - \alpha \nabla f(\rho_t))^T \nabla g(\tilde{\rho}) - G + g(\tilde{\rho}) > 0 then
  9:
                          y_u = y_m
10:
                    else
11:
12:
                           y_l = y_m
                    end if
13:
                    y_m = \frac{y_u + y_l}{2}
14:
              end while
15:
              y^* = y_m
16:
             Return y^*
17:
18: end if
```

This approach is closely related to the work of Nishioka and Kanno [7], who addressed topology optimization problems involving only a single volume constraint. In contrast, our goal is to develop a formulation that generalizes to the full class of problems described in Theorem 1. To this end, we next consider two additional cases in which the solution form of the projection can be explicitly determined.

3.2.2 Solving Problems With Independent Constraints

In many TO problems, multiple independent constraints arise, for instance, in multi-material designs where each material is subject to its own volume constraint. In such cases, each constraint depends on a distinct subset of design variables that are independent of one another. Consequently, each constraint can be solved using the same binary search procedure introduced for the single-constraint case (Algorithm 1).

Because the subproblems are independent, binary searches for the corresponding dual variables can be executed separately and efficiently in parallel too. This property enables significant computational acceleration, which we exploit in our implementation.

3.2.3 Solving The General Projection Problem Efficiently

We now turn to the most general case, where multiple *non-independent* constraints are present. Prior work typically addresses this setting by identifying the active set of constraints and then

solving for the corresponding dual variables based on the solution form in Theorem 1. However, active-set methods can be computationally expensive and may require several iterations to determine the correct set of active constraints. Moreover, such approaches lack convergence guarantees when the problem becomes locally infeasible.

To overcome the issues of active-set finding and local infeasibility, we propose a reformulation of the projection problem, which enables us to not only find a projection by solving only one subproblem but also overcome the issue of local infeasibility. To do this, we propose a Newton-based root-finding method that can uniquely determine an optimal projection even when the feasible set is null. To do this, we adjust the projection problem by introducing regularization parameters to the problem:

$$\min_{\boldsymbol{\delta} \in \mathbb{R}^{N}, \mathbf{s} \in \mathbb{R}^{m}} \quad \frac{1}{2} \|\boldsymbol{\delta}\|_{2}^{2} + \frac{C}{2} \|\mathbf{s}\|_{2}^{2}$$
s.t. $l \leq \tilde{\rho}_{i} + \delta_{i} \leq u, \quad \forall i \in [N]$

$$g_{j}(\boldsymbol{\rho}_{t}) + (\boldsymbol{\delta} - \alpha \nabla f(\boldsymbol{\rho}_{t}))^{T} \nabla g_{j}(\boldsymbol{\rho}_{t}) - s_{j} \leq G_{j} \quad \forall j \in [m]$$

$$s_{j} \geq 0 \quad \forall j \in [m],$$
(8)

where C>0 is a large penalty parameter. This problem is a strictly convex Quadratic Program (QP) and is always feasible, and the solution of this problem becomes identical to the original projection as $C\to\infty$. If we perform the same optimality criteria analysis for this projection problem, we can show that a similar form of solution based on m dual variables exists with relaxed conditions on the constraints. Theorem 2 demonstrates how this regularization formulation changes the form of the solution

Theorem 2 (Solution to the Regularized Projection Problem) Let the linearized projection problem be defined as in (8). A vector $\mathbf{\delta}^* \in \mathbb{R}^N$ is the unique optimal solution to this problem if and only if there exists a unique vector of dual variables $\mathbf{y}^* \in \mathbb{R}^m$ satisfying $\mathbf{y}^* \leq \mathbf{0}$, such that for all $i \in \{1, ..., N\}$:

$$\delta_{i}^{*} = \begin{cases} l - \tilde{\rho}_{i} & \text{if } \sum_{j} y_{j}^{*}(\nabla g_{j}(\boldsymbol{\rho}_{t}))_{i} < l - \tilde{\rho}_{i}, \\ \sum_{j} y_{j}^{*}(\nabla g_{j}(\boldsymbol{\rho}_{t}))_{i} & \text{if } l - \tilde{\rho}_{i} \leq \sum_{j} y_{j}^{*}(\nabla g_{j}(\boldsymbol{\rho}_{t}))_{i} \leq u - \tilde{\rho}_{i}, \\ u - \tilde{\rho}_{i} & \text{if } \sum_{j} y_{j}^{*}(\nabla g_{j}(\boldsymbol{\rho}_{t}))_{i} > u - \tilde{\rho}_{i}, \end{cases}$$
(9)

and for all $j \in \{1, \ldots, m\}$:

$$g_j(\tilde{\boldsymbol{\rho}}) + \boldsymbol{\delta}^T \nabla g_j(\tilde{\boldsymbol{\rho}}) + \frac{2y_j}{C} \le G_j$$
 (10)

$$y_j \left(g_j(\tilde{\boldsymbol{\rho}}) + (\boldsymbol{\delta} - \alpha \nabla f(\boldsymbol{\rho}_t))^T \nabla g_j(\tilde{\boldsymbol{\rho}}) + \frac{2y_j}{C} - G_j \right) = 0$$
 (11)

Proof The proof follows from the detailed KKT analysis in Appendix A. The form of δ^* and the conditions on \mathbf{y}^* and the feasibility of δ^* are an exact restatement of the KKT conditions for this convex problem.

It can be seen that when $C \to \infty$, the solution in Theorem 2 becomes identical to the form in Theorem 1. Thus, for a sufficiently large C, solving this problem will yield a solution which is identical to the true projection problem. This problem is guaranteed to be feasible, and as we will show, can be solved with just one root-finding step.

The key observation that we highlight in this problem is the fact that the Jacobian of constraint functions, $\mathbf{h}(\mathbf{y})$, defined as $h_j(\mathbf{y}) = g_j(\tilde{\boldsymbol{\rho}}) + (\boldsymbol{\delta} - \alpha \nabla f(\boldsymbol{\rho}_t))^T \nabla g_j(\tilde{\boldsymbol{\rho}}) + \frac{2y_j}{C} - G_j$, will be symmetric positive definite and thus invertible, and well behaved. This allows us to solve the problem using a semismooth Newton method and obtain a projection solution directly and with the superlinear convergence associated with the Newton method. To this, we define a system of semismooth nonlinear functions, $\Phi(\mathbf{y})$, whose roots we obtain using a semismooth Newton iteration. These functions are defined as:

$$\Phi_j(\mathbf{y}) = \max(h_j(\mathbf{y}), 0) + \operatorname{sign}(\max(-h_j(\mathbf{y}), 0))y_j.$$
(12)

We detail this choice and why the SPD (symmetric positive definite) nature of the Jacobian of $\mathbf{h}(\mathbf{y})$ guarantees convergence to a solution in a superlinear manner in Appendix A.2.3. Suffice it to say that for a system with a small number of constraints, $m \ll N$, obtaining the Jacobian, $\mathbf{J}_{\Phi}(\mathbf{y})$ and its inverse will be computationally inexpensive. Still, one may not need to solve this

projection problem in most cases anyway. It is expected that in many real-world numerical problems with complex constraint functions, we commonly observe only one active constraint while other constraints remain inactive. Given the simplicity and computational efficiency of solving a single constraint problem, in our algorithm, we propose solving the single constraint case for all constraints in parallel using binary search, and if the solution is found, avoiding the iterative semismooth Newton solver altogether. In this manner, we ensure that in many of the iterations where only one active constraint plays a role, we obtain the solution quickly and efficiently without the need for a more complex smooth Newton method. Algorithm 2, shows the full projection algorithm for the general case. Note that in practice, we set $C=10^9$ by default. Note that this value can be adjusted depending on the problem and constraint gradients. Note that the idea of avoiding active-set finding by regularization has been explored in similar manners [17, 18], and here we provide one such framework with a line search-based stepsize determination for solving this problem.

Algorithm 2 General Multi-Constraint Projection Solver

```
Require: \tilde{\boldsymbol{\rho}}, \nabla \mathbf{g}(\tilde{\boldsymbol{\rho}}), \mathbf{g}(\tilde{\boldsymbol{\rho}}), \mathbf{G}, l, u, C, tol_B, tol_N, maxiter
       - Stage 1: Attempt to solve by assuming a single active constraint -
 1: for j \in \{1, ..., m\} do
                                                                                           ▶ This loop can be executed in parallel
           Let \mathbf{y}_{\text{trial}} = \mathbf{0} \in \mathbb{R}^m.
            Use Algorithm 1 to find a candidate y_i^* for constraint j with tolerance tol<sub>B</sub>.
 3:
 4:
           Set y_{\text{trial},j} = y_i^*.
            Compute \delta_{\text{trial}} = \delta(\mathbf{y}_{\text{trial}}) using Equation (A12).
  5:
           is\_feasible = true
  6:
            for k \in \{1, ..., m\} do
  7:
                 if g_k(\tilde{\boldsymbol{\rho}}) + \boldsymbol{\delta}_{\text{trial}}^T \nabla g_k(\tilde{\boldsymbol{\rho}}) > G_k + \text{tol}_N then
 8:
                       is\_feasible = false; break
 9:
                 end if
10:
            end for
11:
           if is_feasible then
12:
                 return \delta_{	ext{trial}}
                                                                                                                ▶ Feasible projection found
13:
            end if
14:
15:
       — Stage 2: Solve the regularized problem via Semismooth Newton —
16: Initialize \mathbf{y}^{(0)} = \mathbf{0}, set k = 0.
     while \|\mathbf{\Phi}(\mathbf{y}^{(k)})\|_{\infty} > \text{tol}_N and k < \text{maxiter do}
Compute \boldsymbol{\delta}(\mathbf{y}^{(k)}) using Equation (A35).
17:
18:
            Compute \mathbf{h}(\mathbf{y}^{(k)}) using Equation (A37).
19:
           Compute \Phi(\mathbf{y}^{(k)}) = \min(-\mathbf{y}^{(k)}, \mathbf{h}(\mathbf{y}^{(k)})).
20:
            Compute the Jacobian \mathbf{J}_{\Phi}(\mathbf{y}^{(k)}) as per Appendix A.2.3.
21:
           Solve the linear system \mathbf{J}_{\Phi}(\mathbf{y}^{(k)})\mathbf{\Delta} = \mathbf{\Phi}(\mathbf{y}^{(k)}) for \mathbf{\Delta}.
22:
           Find \alpha^* \in (0,1] via line search to ensure reduction in M = \frac{1}{2} \|\mathbf{\Phi}\|_2^2 (Appendix A.2.3).
23:
           \mathbf{y}^{(k+1)} = \mathbf{y}^{(k)} - \alpha^* \mathbf{\Delta}.
24.
           k \leftarrow k + 1.
25:
26: end while
     \mathbf{y}^* = \mathbf{y}^{(k)}.
28: Compute \delta^* = \delta(\mathbf{y}^*) using Equation (A35).
29: return \delta^*
```

3.2.4 A Note On Equality Constraints

Thus far, we have considered only inequality constraints. In practice, the main challenge across all cases lies in identifying the active constraints. Equality constraints can be naturally incorporated by treating them as always active. Consequently, they are handled identically to active inequality constraints within our framework. In the single-constraint and independent multi-constraint cases, this treatment requires no modification to the solution procedure. For the regularized projection problem, equality constraints are enforced directly by setting $\Phi_j(\mathbf{y}) = h_j(\mathbf{y})$ and requiring this quantity to be zero, thereby ensuring that the equality constraint is always active. These adjustments integrate seamlessly with the existing formulation

and introduce no additional complexity. For brevity, we omit further discussion of equality constraints and focus on inequality-constrained problems in the main body of the paper.

3.3 Convergence Analysis And Dynamic Step Size

Here, we will lay out the details of the convergence analysis for the projected gradient descent optimization problem we defined for TO. Theorem 3, shows that for a small enough step size α , the proposed projected gradient descent approach will converge at a rate $O(1/\sqrt{K})$, if the objective function is assumed to be L-smooth. In appendix A.3, we argue that in most cases for TO problems based on FEA analysis, the assumption of L-smoothness is reasonable, so long as the resulting systems of equations are near-singular.

Theorem 3 (Convergence of Projected Gradient Descent with Linearized Constraints) Let the objective function $f: \mathbb{R}^N \to \mathbb{R}$ be bounded from below by f_{inf} and be L-smooth with a Lipschitz constant $L_f > 0$. Consider the iterative algorithm:

$$\boldsymbol{\rho}_{t+1} = \Pi_{\hat{\Omega}_{t+1}} \left(\boldsymbol{\rho}_t - \alpha \nabla f(\boldsymbol{\rho}_t) \right)$$

where $\Pi_{\hat{\Omega}_{t+1}}$ is the Euclidean projection onto the linearized feasible set $\hat{\Omega}_{t+1}$ defined in Equation (4), and the step size α is constant.

If the step size satisfies $0 < \alpha < \frac{2}{L_f}$ and each iterate satisfies the condition $\rho_t \in \hat{\Omega}_{t+1}$ for all $t \geq 0$, then the algorithm guarantees that the norm of the updates converges to zero, with a sublinear rate of:

$$\min_{t=0,...,K-1} \| \boldsymbol{\rho}_{t+1} - \boldsymbol{\rho}_{t} \|_{2} \leq \sqrt{\frac{f(\boldsymbol{\rho}_{0}) - f_{inf}}{L \cdot K}} = O\left(\frac{1}{\sqrt{K}}\right)$$

where $L = \frac{1}{\alpha} - \frac{L_f}{2}$ is a positive constant.

Proof The full derivation, including the required assumptions on the iterates and objective function, is provided in Appendix A.3. This proof mostly follows the commonly established convergence in PGD approaches [19]. \Box

Based on the convergence analysis, we propose a dynamic step size assignment for the algorithm based on a local estimate of the Lipschitz constant for the objective function. The overall proposed step size will be estimated by tracking the gradients of the objective function to estimate the Lipschitz constant [19]:

$$\alpha_t = \frac{\|\boldsymbol{\rho}_t - \boldsymbol{\rho}_{t-1}\|_2}{\|\nabla f(\boldsymbol{\rho}_t) - \nabla f(\boldsymbol{\rho}_{t-1})\|_2}$$
(13)

For the first step, we choose $\alpha_0 = \frac{\alpha_{\text{fallback}}}{\|\nabla f(\rho_0)\|_{\infty}}$ so as to cap the maximum change in design variables in the first step to α_{fallback} . This can be adjusted based on the requirements of the problem, the problem's behavior, and the design variable bounds. For our results and experiments, we use a default value of $\alpha_{\text{fallback}} = 0.2$. Over the entire process, we set an overall higher limit on the step size, denoted as α_{max} , which brings us to the final expression:

$$\alpha_t = \min\left(\frac{\|\boldsymbol{\rho}_t - \boldsymbol{\rho}_{t-1}\|_2}{\|\nabla f(\boldsymbol{\rho}_t) - \nabla f(\boldsymbol{\rho}_{t-1})\|_2}, \alpha_{\max}\right). \tag{14}$$

3.4 The Full PGD Algorithm For TO

In this section, we detail the complete algorithm we use in our experiments and discuss the full dynamic step size we use, as well as the full framework with all of the different aspects of the approach put together.

3.4.1 Spectral Dynamic Step Size

Although a local Lipschitz estimation can be effective in most stable problems, it is well known that in PGD approaches in nonlinear optimization, spectral methods are effective at improving convergence and overall stability of the algorithm [20]. Given this, we further adapt the dynamic step size in our algorithm by incorporating a relatively simple spectral step size adjustment as proposed by Birgin et al. [20] in their algorithm 2.1. Let $\mathbf{s}_{t+1} = \boldsymbol{\rho}_t - \boldsymbol{\rho}_{t-1}$ and $\mathbf{y}_{t+1} = \nabla f(\boldsymbol{\rho}_t) - \nabla f(\boldsymbol{\rho}_{t-1})$. When $\mathbf{s}_{t+1}^T \mathbf{y}_{t+1} \leq 0$, then we set α_{t+1} based on (14), and when this does not hold we adjust the stepsize by setting $\alpha = \frac{\mathbf{s}_{t+1}^T \mathbf{s}_{t+1}}{\mathbf{s}_{t+1}^T \mathbf{y}_{t+1}}$. We also make sure that this value does

not exceed either α_{max} or $\frac{2}{L_f}$, as convergence analysis tells us a step size above $\frac{2}{L_f}$ will not have convergence guarantees. This brings us to the final spectral step size expression:

$$\hat{\alpha}_{t} = \begin{cases} \min\left(\frac{\|\boldsymbol{\rho}_{t} - \boldsymbol{\rho}_{t-1}\|_{2}}{\|\nabla f(\boldsymbol{\rho}_{t}) - \nabla f(\boldsymbol{\rho}_{t-1})\|_{2}}, \alpha_{\max}\right) & \text{if } \mathbf{s}_{t+1}^{T} \mathbf{y}_{t+1} \leq 0\\ \min\left(\frac{\mathbf{s}_{t+1}^{T} \mathbf{s}_{t+1}}{\mathbf{s}_{t+1}^{T} \mathbf{y}_{t+1}}, \frac{2 \times \|\boldsymbol{\rho}_{t} - \boldsymbol{\rho}_{t-1}\|_{2}}{\|\nabla f(\boldsymbol{\rho}_{t}) - \nabla f(\boldsymbol{\rho}_{t-1})\|_{2}}, \alpha_{\max}\right) & \text{if } \mathbf{s}_{t+1}^{T} \mathbf{y}_{t+1} > 0 \end{cases}$$

$$(15)$$

This is the final expression for the dynamic step size we use in our approach. Note that in practice, rather than checking $\mathbf{s}_{t+1}^T \mathbf{y}_{t+1} > 0$, we check for $\mathbf{s}_{t+1}^T \mathbf{y}_{t+1} > \epsilon_{\alpha}$ and use $\epsilon_{\alpha} = 10^{-6}$.

3.5 Projection Independence from Gradients

The proposed PGD framework separates the projection operation from the gradient computation. This independence allows the search direction to be replaced with higher-order or quasi-Newton updates, such as BFGS, when appropriate. However, since topology optimization problems typically involve very large and sparse Hessians, we employ a nonlinear conjugate gradient approach, which avoids explicit Hessian computation. Specifically, we adopt the popular conjugation scheme proposed by Polak and Ribiere [21], with a reset by adjusting the search direction with the following scheme:

$$\mathbf{d}_{0} = \nabla f(\boldsymbol{\rho}_{t})$$

$$\beta_{t} = \max \left(\frac{\nabla f(\boldsymbol{\rho}_{t})^{T} (\nabla f(\boldsymbol{\rho}_{t}) - \nabla f(\boldsymbol{\rho}_{t-1}))}{\|\nabla f(\boldsymbol{\rho}_{t-1}\|_{2}^{2}}, 0 \right)$$

$$\mathbf{d}_{t} = -\nabla f(\boldsymbol{\rho}_{t}) + \beta_{t} \, \mathbf{d}_{t-1}$$
(16)

These search directions provide faster convergence than raw gradient descent while maintaining low computational cost.

3.6 Ensuring Convergence

We saw in Theorem 3 that convergence is only guaranteed at the rate in Theorem 3 if the iterates remain feasible across iterations. Thus, to ensure stable convergence, we revert to $\alpha_{t+1} = \frac{\alpha_{\text{fallback}}}{\|\nabla f\|_{\infty}}$ when the iterate has constraint violation above the tolerance in the Newton projection. However, conceding that initial iterations will likely violate this, given the large changes in initial steps, we only apply this heuristic after the first $t_{\text{warmup}} = 50$ steps. Moreover, to make adjusting algorithm stability easy, we include an overall relaxation variable ω , which we set to 1.0, meaning no relaxation, to relax all step sizes if a problem is ill-conditioned and requires smaller steps. We detail this in the whole algorithm presented in later sections.

Algorithm 3 Full PGD Algorithm for Topology Optimization

```
Require: \rho_0 \in [l, u]^N, tol<sub>B</sub>, tol<sub>N</sub>, tol, C, l, u, K_{\max}, \alpha_{\max}, \alpha_{\text{fallback}}, t_{\text{warmup}}, \omega
Ensure: Optimized design variable \rho^*
   1: Set step size \alpha_0 = \min\left(\alpha_{\max}, \frac{\alpha_{\text{fallback}}}{\|\nabla f(\boldsymbol{\rho}_0)\|_{\infty}}\right)
   2: for t = 0 to K_{\text{max}} - 1 do
                 Compute f(\boldsymbol{\rho}_t), \mathbf{g}(\boldsymbol{\rho}_t), \nabla \mathbf{g}(\boldsymbol{\rho}_t), \nabla f(\boldsymbol{\rho}_t) if (t \geq t_{\text{warmup}} and \|\mathbf{g}(\boldsymbol{\rho}_t)\|_{\infty} > \text{tol}_N) or t = 0 then
   4:
                         \alpha_t = \min\left(\alpha_{\max}, \frac{\alpha_{\text{fallback}}}{\|\nabla f(\boldsymbol{\rho}_t)\|_{\infty}}\right)
   5:
   6:
                          Compute \alpha_t based on Equation 15
   7:
                  end if
   8:
                 Compute \mathbf{d}_t from Equation 16
                                                                                                             ▶ Alternates like other CG, BFGS, etc. possible
   9:
                  \tilde{\boldsymbol{\rho}} = \boldsymbol{\rho}_t - \omega \, \alpha_{t+1} \, \mathbf{d}_t
 10:
                  if m=1 or constraints are independent then
 11:
                          \boldsymbol{\delta}^* \leftarrow \text{Algorithm } \mathbf{1}(\tilde{\boldsymbol{\rho}}, \nabla \mathbf{g}, \mathbf{g}, \mathbf{G}, l, u, \text{tol}_B)
 12:
 13:
                          \boldsymbol{\delta}_t \leftarrow \text{Algorithm } \mathbf{2}(\tilde{\boldsymbol{\rho}}, \nabla \mathbf{g}, \mathbf{g}, \mathbf{G}, l, u, C, \text{tol}_B, \text{tol}_N)
 14:
 15:

\boldsymbol{\rho}_{t+1} = \tilde{\boldsymbol{\rho}} + \boldsymbol{\delta}_t

 16:
                 if \frac{\|oldsymbol{
ho}_{t+1}-oldsymbol{
ho}_t\|_2}{\|oldsymbol{
ho}_{t+1}\|_2} \leq 	ext{tol then}
 17:
 18:
                          return \rho_{t+1}
                  end if
 19:
 20: end for
 21: return 
ho_{K_{
m max}}
```

Algorithm 3 summarizes the complete PGD framework for topology optimization. The algorithm integrates the proposed projection solvers, spectral step-size adaptation, and nonlinear conjugate-gradient directions into a single optimization loop. While the current implementation employs a basic descent update with adaptive step sizing, more advanced update rules incorporating momentum or higher-order information can be seamlessly integrated. We will briefly discuss this in experiments, but keep the simpler scheme above as our main algorithm and leave further development of more advanced update schemes to future work. In our experiments, we use default parameters $C = 10^{12}$, $\alpha_{\text{max}} = 10^2$, $\text{tol}_B = 10^{-8}$, and $\text{tol}_N = 10^{-6}$.

In the section that follows, we will perform numerical experiments on common TO problems and toy TO problems, and compare our method with the most commonly used algorithms in the literature in terms of both computational efficiency and convergence behavior.

4 Numerical Verification and Experiments

In this section, we evaluate the proposed PGD optimizer against the widely used MMA, which serves as the standard solver in many TO applications. We compare convergence behavior and computational efficiency, showing that the proposed PGD algorithm achieves convergence rates comparable to MMA while offering substantially improved computational performance.

To measure efficiency, we report wall-clock time per iteration as our primary metric, as the advantages of parallelization in the proposed PGD projection solver and implementation-specific details are not easily captured by FLOP counts or memory operations. For completeness, we also benchmark the *Optimality Criteria* (OC) method in single-constraint problems to demonstrate that PGD matches OC in computational cost while achieving convergence trends similar to MMA—highlighting its balance between simplicity and scalability.

We conduct four classes of benchmark experiments:

• Single Linear Constraints: We run the typical minimum compliance problem with a volume fraction constraint. This problem represents how each algorithm we test performs with respect to problems with a single constraint, which is linear. In this scenario, the projection is exact, and the special case of only binary search for projection stands. These

experiments highlight performance in cases with a single linear constraint, which is very common in TO.

- Single nonlinear Constraints: In this scenario we run the inverted problem. That is to minimize volume under compliance constraints. This is a special case where the projection will not be exact with the linear assumption, while the single constraint benefits remain.
- Multiple Independent Constraints: In this case, we run the minimum compliance problem, but with four different materials. Each material has a different Young's modulus, and the volume fraction for each material is separately constrained. This scenario is meant to highlight performance in cases where constraints are independent, and therefore, the projection sub-problem can be solved by binary search. This is meant to demonstrate the scalability of PGD in independent constraint scenarios.
- General Multiple Constraints: Finally, we run an example of a fully general TO problem with minimum compliance as the objective, but with multiple dependent constraints. In this scenario, we apply the volume fraction requirement, as well as requiring the center of mass of the design to be within a desired region. The latter constraint is nonlinear and not independent of the volume constraint, which represents a general case where multiple general constraints are present. This is a scenario where the regularized projection and semi-smooth Newton method are tested in PGD.

In each of these scenarios, we employ the popular Solid Isotropic Material Penalization (SIMP) approach for dynamically adjusting the Young's modulus of each element in the mesh. We do not detail this in the paper for brevity and refer interested readers to the work by Bendsoe and Sigmund [22] for more details. Suffice it to say that the FEA for the underlying problem yields a system of equations $\mathbf{K}(\rho) = \mathbf{f}$. Moreover, we use the same FEA solver, which we include with our publicly available code, for all optimizers, and use a density filter with a filter radius of 1.5 (See [22]) for the SIMP penalty scheme. For all problems, we run each optimizer for 300 steps and report our results for each experiment. Finally, we use the SIMP penalization scheme with a penalty of 3. Finally, we run all problems for regular grid meshes with resolutions 128×64 , 256×128 , and 512×256 , to measure how well each approach scales with the number of design variables.

In all cases, we adopt the standard cantilever beam configuration for boundary conditions and loading, as illustrated in Fig. 1.

4.1 The Benchmark Problems

Before presenting the results, we first formalize the specific optimization problems used in our benchmarks. Each of the four test cases corresponds to one of the problem classes described in the previous section, designed to assess solver performance across varying levels of nonlinearity, coupling, and constraint complexity. The formulations of these benchmark problems are summarized below, and the corresponding results are discussed in the following section.

4.1.1 Volume Constrained Minimum Compliance

This problem is an example of a single linear constraint TO problem. The compliance objective is defined as $\mathbf{f}^T \mathbf{K}^{-1}(\boldsymbol{\rho}) \mathbf{f}$. For a mesh with N elements, the minimum compliance problem with volume constraint can be formulated as:

$$\min_{\boldsymbol{\rho} \in R^{N}} \quad \mathbf{f}^{T} \mathbf{K}^{-1}(\boldsymbol{\rho}) \mathbf{f}$$
s.t. $0 \le \rho_{i} \le 1, \quad \forall i \in [N]$

$$\frac{1}{N} \sum_{i=1}^{N} \rho_{i} \le V_{f},$$
(17)

where V_f is the target volume fraction. As can be seen, we are left with a single constraint other than bounds, which is linear. In these experiments, we initialize the optimizers with $\rho = 1$, and set the target volume fraction to 0.2.

4.1.2 Compliance Constrained Minimum Volume

In this case, we simply invert the constraint and objective of the problem above:

$$\min_{\boldsymbol{\rho} \in R^{N}} \quad \frac{1}{N} \sum_{i=1}^{N} \rho_{i}$$
s.t. $0 \le \rho_{i} \le 1$, $\forall i \in [N]$

$$\mathbf{f}^{T} \mathbf{K}^{-1}(\boldsymbol{\rho}) \mathbf{f} \le C_{\text{max}},$$
(18)

where C_{max} is the target maximum allowable compliance. As evident here, we will have a single nonlinear constraint. In these problems, we set a compliance limit of $C_{\text{max}} = 150$, assuming a Young's modulus of 1.0 and a force magnitude of 1.0.

4.1.3 Multi-Material Volume Constrained Minimum Compliance

In these problems, we intend to use multiple different materials with different Young's moduli, and with separate volume constraints independently applied to each material. For modelling material, we use the penalization scheme proposed by Zheng et al. [23] with the same filtering and penalty schedules as we use for SIMP. The formulation of this problem is similar to the problem before, except now there are multiple materials with their own volume constraints. For a mesh with N elements, and a problem with K materials, the problem can be formulated as:

$$\min_{\boldsymbol{\rho} \in R^{N}} \quad \mathbf{f}^{T} \mathbf{K}^{-1}(\boldsymbol{\rho}) \mathbf{f}$$
s.t. $0 \le \rho_{i} \le 1, \quad \forall i \in [N]$

$$\frac{1}{N} \sum_{i=1}^{N} \rho_{i} \le V_{j}, \quad \forall i \in M_{j} \ \forall j \in [K]$$
(19)

where V_j is the target volume fraction of material j and $M_j \subset \{1, \ldots, N\}$ is the subset of design variable indices associated with material j. As can be seen, we have multiple independent constraints $(M_i \cap M_j = \emptyset \text{ if } i \neq j)$ in this problem. In these problems, we solve for four materials with Young's moduli of 1.0, 0.5, 0.25, 0.125, with each material having a target volume fraction of 0.05.

4.1.4 Volume and Weight Distribution Constrained Minimum Compliance

Finally, to test the general case, we perform optimization on a problem with multiple interdependent constraints. For this example, we perform the minimum compliance problem with a volume constraint, as well as dictating that the resulting topologies' center of mass be placed within a certain region of space. This problem can be formulated as:

$$\min_{\boldsymbol{\rho} \in R^{N}} \quad \mathbf{f}^{T} \mathbf{K}^{-1}(\boldsymbol{\rho}) \mathbf{f}$$
s.t. $0 \le \rho_{i} \le 1, \quad \forall i \in [N]$

$$\frac{1}{N} \sum_{i=1}^{N} \rho_{i} \le V_{f},$$

$$\|\mathbf{R}(\boldsymbol{\rho}) - \mathbf{R}_{t}\|_{2}^{2} \le r_{b}$$
(20)

where V_f is the target volume fraction, and $\mathbf{R}(\boldsymbol{\rho})$ is the center of mass based on the material distribution, \mathbf{R}_t is the center of the acceptable region, and r_b is the maximum distance that is acceptable from \mathbf{R}_t . As is evident, here we have multiple interdependent and nonlinear constraints. This problem will thus allow us to simulate a case of a general TO problem. In these problems, we set the target volume fraction to 0.2 and set the desired center of mass to $\begin{pmatrix} 0.25 \\ 0.25 \end{pmatrix}$ on a domain of length 1.0 along the x-axis and 0.5 along the y-axis. Moreover, we set the tolerance radius $r_b = 10^{-2}$ in these problems (See Fig. 1).

4.2 Results

With the test problems established, we now present the results of the experiments in each scenario and compare the three different optimizers we test. For each problem, we briefly described the exact settings of the problem and left full details to our publicly available code for brevity. Below, we present the results of running PGD (with and without the independent constraint assumption for the multi-material case), MMA, and OC optimizers (only in single and multi-material minimum compliance).

4.2.1 Solution Time & Scalability

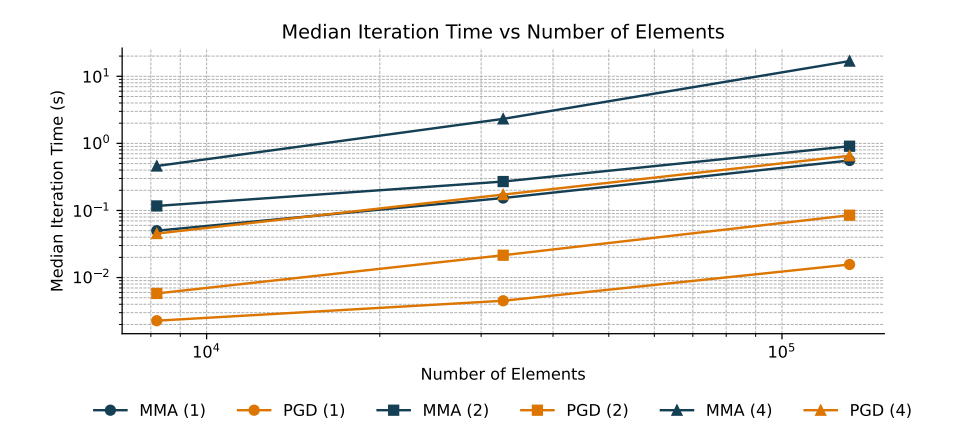


Fig. 2: Scaling of iteration time with problem size and number of constraints. PGD achieves roughly an order-of-magnitude improvement in iteration time across all constraint counts and scales almost log-linearly with the number of elements. Notably, PGD with four constraints matches the iteration time of MMA with a single constraint, while MMA's cost rises sharply as the number of constraints increases from two to four—highlighting the superior scalability of the proposed approach.

Before discussing convergence and constraint handling in each case, we discuss the most important reason for the deployment of the proposed PGD algorithm, scalability and computational efficiency over methods like MMA. Note that in all experiments, we find that both PGD and MMA could handle linear and nonlinear constraints and converged in all cases (we discuss the nuances of this in later sections). With that in mind, we investigate the computational cost and scalability of both PGD and MMA across both design variable count and constraint count.

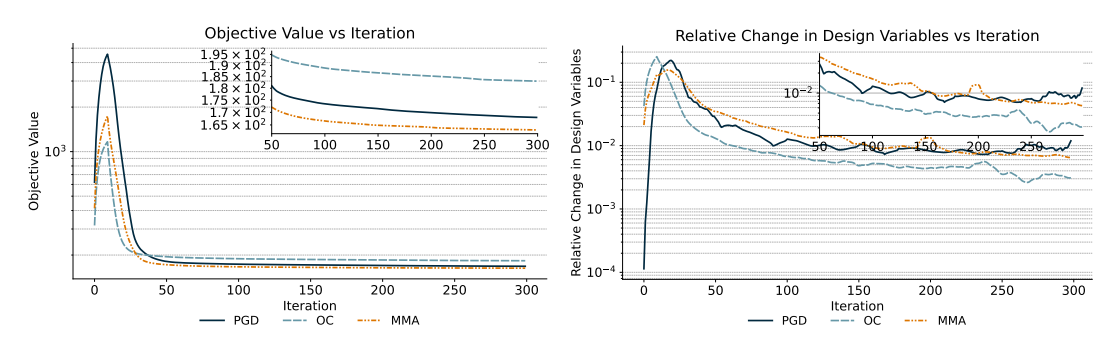
		Number of Constraints		
Optimizer	Variable Count	1	2	4
	8192	0.0461	0.1176	1.883
MMA	32768	0.1444	0.2623	1.8915
	131072	0.6188	0.9067	8.4764
PGD	8192	$0.0022 (22.35 \times)$	$0.0053~(22.2\times)$	0.0437 (43.06 ×)
	32768	$0.0041 \ (35.08 \times)$	$0.0205~(12.77\times)$	$0.1777 \ (10.64 \times)$
	131072	$0.0146 \ (42.44 \times)$	$0.0799~(11.35\times)$	$0.6534~(12.97\times)$
PGD^{\dagger}	8192	0.0022 (22.35 ×)	-	0.0060 (312.11 ×)
	32768	$0.0041 \ (35.08 \times)$	-	$0.0164~(115.23\times)$
	131072	0.0146 (42.44 ×)	-	$0.0537 \ (157.82 \times)$

Table 1: Median iteration time (s) across problem sizes and constraint counts. Comparison of MMA, PGD with Newton-based projection, and PGD[†] with independent-constraint (binary-search) projection. Values in parentheses indicate the speedup of PGD relative to MMA. PGD achieves approximately ten- to forty-fold faster iterations across general problems and over one hundred-fold acceleration when constraints are independent, demonstrating its efficiency and scalability.

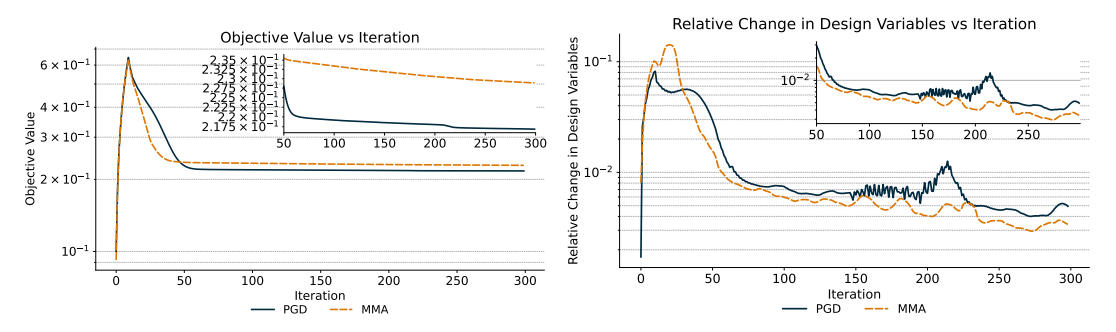
Table 1 shows how both MMA and PGD median iteration times look across different problem sizes and numbers of constraints. The problems reported in the above table are for minimum compliance (single constraint), weight distribution, and volume-constrained minimum compliance (two constraints), and multi-material minimum compliance (four constraints). We see that in the single constraint case, PGD speeds up optimization more than in multi-constraint scenarios, which is expected since single constraint problems will be solved using only binary search, while multi-constrained problems will require Newton iterations in some scenarios, as seen in the initial jump in iteration time in Figure 2. More notably, in multi-constraint scenarios with independent constraints, the binary search projection solution of PGD is two orders of magnitude faster, making it an even more efficient choice for these scenarios. Overall, we see that the PGD approach we propose can provide an order of magnitude improvement in iteration time compared to MMA, which can save a significant amount of time in optimization, especially in large-scale scenarios.

4.3 Convergence & Robustness

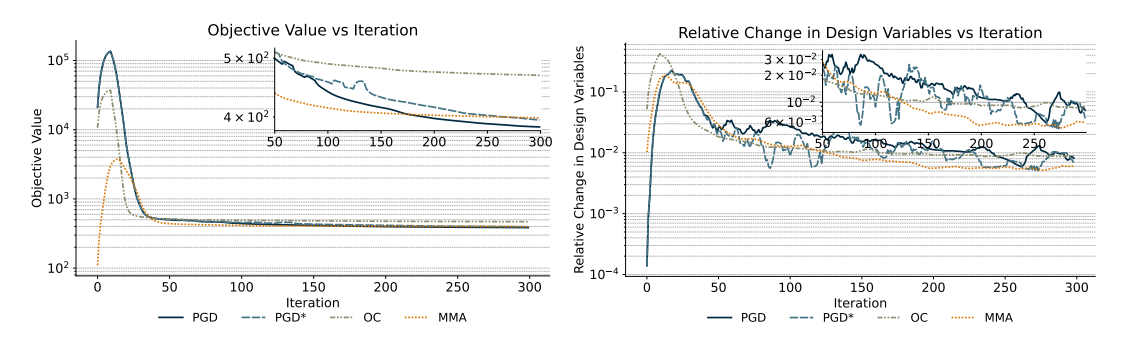
Minimum Compliance Problem



Compliance Constrained Minimum Volume



Multi-Material Minimum Compliance



Volume & Weight Distribution Constrained Minimum Compliance

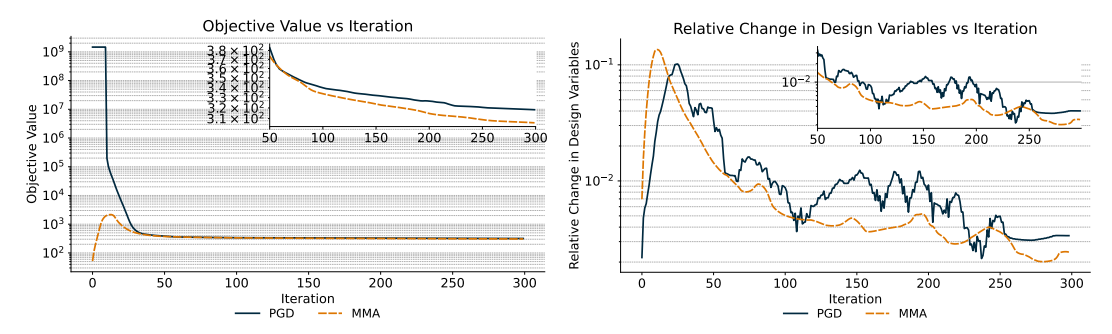


Fig. 3: Convergence behavior at fine mesh resolution for each benchmark problem. Each column compares objective evolution (left) and relative design-variable change (right) for single-and multi-constraint problems with both linear and nonlinear constraints. Across all four scenarios, PGD, MMA, and OC exhibit nearly identical convergence trajectories, confirming that the proposed PGD framework is broadly applicable and numerically stable across diverse constraint types. PGD* denotes PGD using the Newton-based projection instead of binary search in cases with independent constraints; the default PGD employs the faster binary-search projection, and PGD* is shown for completeness.

We provide the full set of results for all experiments in Appendix A.5, and only discuss the main findings in this section. Figure 3 shows that the proposed PGD approach converges and exhibits stable convergence in both problems with linear and nonlinear constraints, while exhibiting convergence behavior and rates similar to those of MMA and OC. This is an important observation, given that it confirms the sequential linear approximation of constraints does not lead to unstable optimization or slower convergence in PGD.

Besides the general stability of solvers, it is important to note the overall convergence behavior of each approach. Qualitatively, when looking at the convergence plots in Figure 3, we observe that MMA and PGD in most cases exhibit similar rates of convergence and converge to designs with similar objective values. This suggests that both approaches provide stable convergence, while PGD, as we discussed, offers an order of magnitude faster optimization iteration time.

4.4 Constraint Handling

Another essential part of optimizing TO problems is adhering to constraints. In our experiments, we track deviations from the constraint boundary across iterations to assess how accurately each optimizer adheres to the constraints of each problem over time. For brevity, we do not include all these figures across problems, and refer interested readers to Appendix A.5. In all problems, the optimizers show stable and consistently low constraint violations, with PGD often exhibiting better adherence than MMA in most experiments.

However, in the problem of compliance-constrained minimum volume, when the problem is solved for coarse and medium grid resolutions, making the simulation and thus compliance more sensitive to a few design variables, the heuristic we apply for post-warm-up step size adjustment kicks in for PGD, which means that the constraint violations and optimization steps start to exhibit an oscillatory behavior. We show an example of this in Figure 4 for the medium resolution run of this problem. Despite the oscillations, we observe that our heuristic-based approach, which relaxes the step sizes when violations are too high, maintains the constraint violation at a low level and does not hinder stable convergence in the objective or design variables. This is evident in the convergence plots shown in Figure 4 as well as the visualization of the designs across iterations. This example illustrates a scenario where sequential linear approximations may become problematic and highlights the importance of incorporating the heuristic step relaxation into the algorithm. Moreover, one could relax all step sizes in the optimizer to stabilize this behavior; however, the inclusion of automatic step relaxation makes the overall algorithm more robust in cases where this behavior is not known a priori.

5 Conclusion

In this work, we propose a comprehensive projected gradient descent framework for constrained optimization, with a particular focus on its application to topology optimization. The central contribution lies in reformulating the projection step, which traditionally can be tough for multiple nonlinear constraints and requires finding the active set every time. This reformulation into a regularized projection problem replaces the explicit active-set determination with a strictly convex quadratic program augmented by penalty terms on constraint violations. This regularization ensures well-posedness and guarantees the existence and uniqueness of the solution, even in the presence of infeasible or near-singular constraint sets. We derived the associated Karush–Kuhn–Tucker conditions and established the strict monotonicity of the resulting operator, enabling the use of a semismooth Newton method for efficient and globally convergent solution of the projection subproblem. Moreover, we show that under certain conditions—single active constraint, or multiple independent constraints—the projection can be solved much faster with a binary search, which is incorporated in our method for much better computational efficiency.

Beyond the algorithmic reformulation, we provided a theoretical analysis of convergence under standard smoothness assumptions. Specifically, we proved that the proposed PGD scheme converges sublinearly for sufficiently small step sizes when the objective function is L-smooth. To enhance convergence in practice, we proposed a dynamic step-size adaptation rule based on local estimates of the Lipschitz constant as well as a spectral projected gradient descent analysis ensuring robustness across a range of problem scales and conditioning scenarios. Moreover, we saw that convergence requires iterates to be feasible across iterations, which for nonlinear constraints could become problematic; thus, we introduce a heuristic relaxation to automatically handle cases where such patterns emerge. The empirical results demonstrate

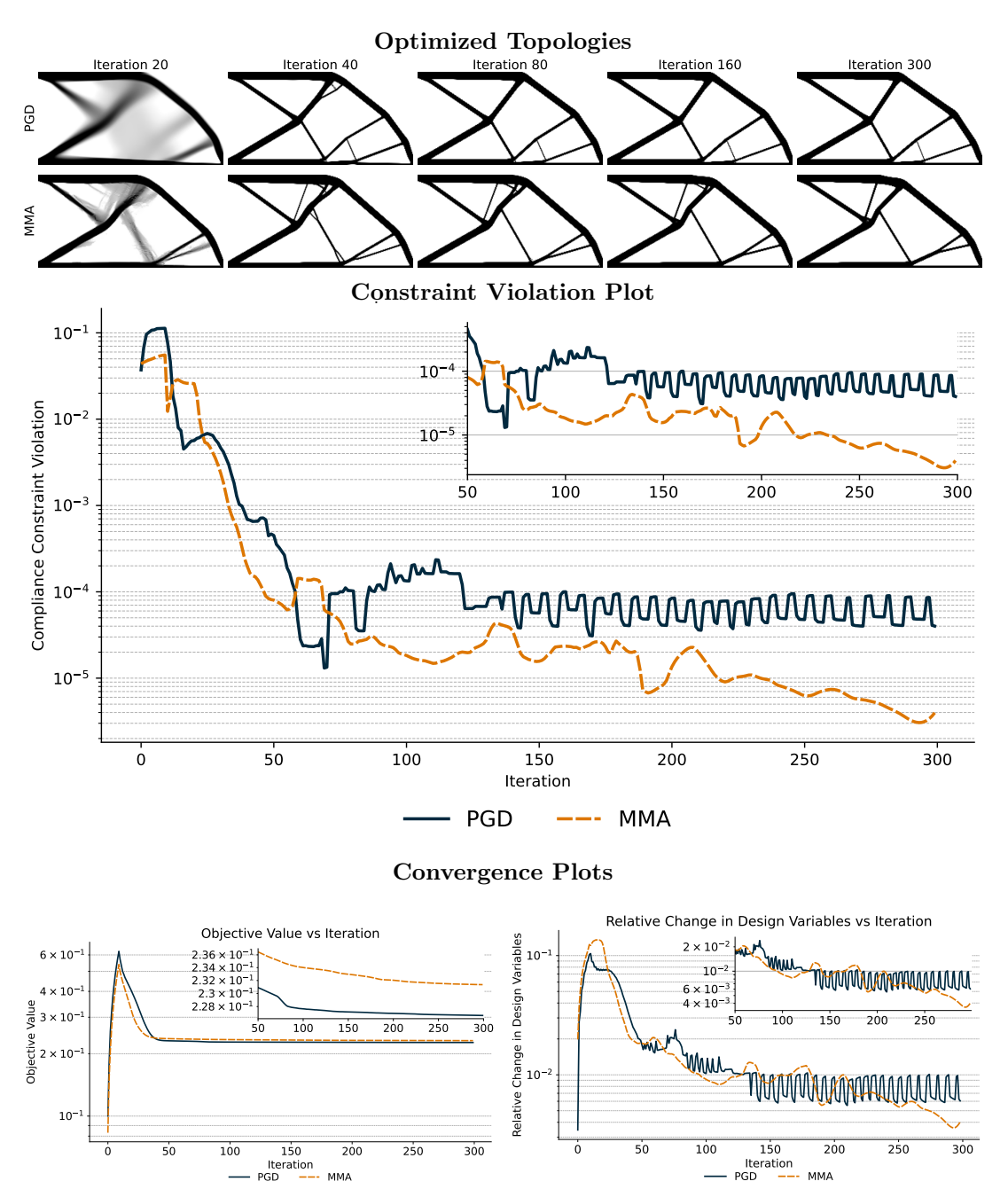


Fig. 4: An example of linear approximation of constraint leading to step size relaxation in our algorithm, keeping the problem stable and convergence behavior robust—as seen visually and in convergence plots—without the need to adjust the global step size relaxation from the start.

that, when applied across topology optimization problems, the PGD method achieves convergence behavior and final compliance comparable to and even better in some cases than that of established approaches such as the Method of Moving Asymptotes and Optimality Criteria, while offering an order of magnitude improvement in scalability and speed.

Our findings suggest several broader implications. The proposed regularized PGD algorithm provides a general-purpose tool for solving high-dimensional, constrained optimization problems that exhibit similar structural properties to TO, namely, those involving nonlinear objectives and constraints with constant bounds on design variables. Its capacity to handle infeasible iterates makes it suitable for a range of domains beyond topology optimization. Furthermore, the modular nature of the approach allows integration with higher-order or even stochastic methods, potentially enabling more advanced optimization approaches.

In summary, this paper establishes a theoretically grounded and computationally efficient framework for projected gradient descent with regularized projections, extending both the analytical understanding and practical usability of PGD-type methods in nonlinear constrained TO

problems. Future research can focus on better search direction and step-size adjustment, incorporating momentum-based approaches. Notably, the increased efficiency and scalability of such an optimizer could enable large-scale nonlinear problem solutions at scale, which allows datasets to be generated for deep-learning-based approaches that require massive scale of data to be successful, and have shown promising results in recent works [24–30]. Finally, this framework, although tested in this paper across various nonlinear and potentially challenging constraint scenarios, has not been tested on a wider range of TO problems with advanced structural and manufacturing constraints, and thus requires more detailed investigation and potentially improvements to be adopted widely by TO and structural optimization researchers. We believe the results here demonstrate the value of such an adoption, especially given that, based on the nature of the proposed algorithms, one would expect an even greater improvement in speed if highly parallelized hardware platforms such as GPUs and TPUs were to be utilized for optimization. To encourage further research on the topic and further investigation on the optimizer, we make our entire platform for efficient FEA and topology optimization accelerated on GPU and CPU publicly available for all to use at https://github.com/ahnobari/pyFANTOM.

References

- [1] Svanberg, K.: The method of moving asymptotes—a new method for structural optimization. International Journal for Numerical Methods in Engineering 24(2), 359–373 (1987) https://doi.org/10.1002/nme.1620240207
- [2] Hassani, B., Hinton, E.: A review of homogenization and topology optimization iii—topology optimization using optimality criteria. Computers & Structures **69**(6), 739–756 (1998) https://doi.org/10.1016/S0045-7949(98)00131-6
- [3] Gomes, F.A., Senne, T.A.: An slp algorithm and its application to topology optimization. Computational & Applied Mathematics **30**, 53–89 (2011) https://doi.org/10.1590/S1807-03022011000100003
- [4] Rojas-Labanda, S., Stolpe, M.: An efficient second-order sqp method for structural topology optimization. Structural and Multidisciplinary Optimization 53(6), 1315–1333 (2016) https://doi.org/10.1007/s00158-016-1471-7
- [5] Hoppe, R.H., Petrova, S.I., Schulz, V.: Primal-dual newton-type interior-point method for topology optimization. Journal of Optimization Theory and Applications 114, 545–571 (2002) https://doi.org/10.1023/A:1014072503048
- [6] Tavakoli, R.: Multimaterial topology optimization by volume constrained allen—cahn system and regularized projected steepest descent method. Computer Methods in Applied Mechanics and Engineering 276, 534–565 (2014) https://doi.org/10.1016/j.cma.2014.04.
- [7] Nishioka, A., Kanno, Y.: Inertial projected gradient method for large-scale topology optimization. Japan Journal of Industrial and Applied Mathematics **40**(2), 877–905 (2023) https://doi.org/10.1007/s13160-023-00563-0
- [8] Barbeau, L., Lamarche-Gagnon, M., Ilinca, F.: Improving the robustness of the projected gradient descent method for nonlinear constrained optimization problems in topology optimization. International Journal for Numerical Methods in Engineering 126(12) (2025) https://doi.org/10.1002/nme.70068
- [9] Gaynor, A.T., Meisel, N.A., Williams, C.B., Guest, J.K.: Topology optimization for additive manufacturing: considering maximum overhang constraint. In: 15th AIAA/ISSMO Multidisciplinary Analysis and Optimization Conference, p. 2036 (2014). https://doi.org/10.2514/6.2014-2036 . https://doi.org/10.2514/6.2014-2036
- [10] Qian, X.: Undercut and overhang angle control in topology optimization: A density gradient based integral approach. International Journal for Numerical Methods in Engineering 111(3), 247–272 (2017) https://doi.org/10.1002/nme.5461
- [11] Lamarche-Gagnon, M.-É., Molavi-Zarandi, M., Raymond, V., Ilinca, F.: Additively

- manufactured conformal cooling channels through topology optimization. Structural and Multidisciplinary Optimization $\bf 67(8)$, 1–19 (2024) https://doi.org/10.1007/s00158-024-03846-3
- [12] Gu, R., Gao, B.: A random active set method for strictly convex quadratic problem with simple bounds. Mathematics of Computation (2024) https://doi.org/10.1090/mcom/3647
- [13] Dostal, Z., Schoberl, J.: Minimizing quadratic functions subject to bound constraints with the rate of convergence and finite termination. Computational Optimization and Applications 30, 23–43 (2005) https://doi.org/10.1007/s10589-005-4584-7
- [14] Bendsoe, M.P.: Optimization of Structural Topology, Shape, and Material. Springer, Berlin, Germany (1995)
- [15] Ferrari, F., Sigmund, O.: A new generation 99 line Matlab code for compliance Topology Optimization and its extension to 3D (2020). https://arxiv.org/abs/2005.05436
- [16] Wang, C., Zhao, Z., Zhou, M., Sigmund, O., Zhang, X.S.: A comprehensive review of educational articles on structural and multidisciplinary optimization. Struct. Multidiscipl. Optim. 64(5), 2827–2880 (2021)
- [17] Hintermüller, M., Ito, K., Kunisch, K.: The primal-dual active set strategy as a semismooth newton method. SIAM Journal on Optimization 13(3), 865–888 (2002) https://doi.org/ 10.1137/S1052623401383558 https://doi.org/10.1137/S1052623401383558
- [18] Börgens, E., Kanzow, C., Steck, D.: Local and global analysis of multiplier methods for constrained optimization in banach spaces. SIAM Journal on Control and Optimization 57(6), 3694–3722 (2019) https://doi.org/10.1137/19M1240186 https://doi.org/10.1137/19M1240186
- [19] Boyd, S., Vandenberghe, L.: Convex Optimization. Cambridge University Press, Cambridge, England (2004)
- [20] Birgin, E.G., Martínez, J.M., Raydan, M.: Spectral projected gradient methods: Review and perspectives. Journal of Statistical Software 60(3), 1–21 (2014) https://doi.org/10. 18637/jss.v060.i03
- [21] Polak, E., Ribiere, G.: Note sur la convergence de méthodes de directions conjuguées. Revue française d'informatique et de recherche opérationnelle. Série rouge **3**(R1), 35–43 (1969)
- [22] Bendsoe, M.P., Sigmund, O.: Topology Optimization, 2nd edn. Springer, Berlin, Germany (2011)
- [23] Zheng, R., Yi, B., Peng, X., Yoon, G.-H.: An efficient code for the multi-material topology optimization of 2d/3d continuum structures written in matlab. Applied Sciences 14(2) (2024) https://doi.org/10.3390/app14020657
- [24] Regenwetter, L., Nobari, A.H., Ahmed, F.: Deep generative models in engineering design: A review. Journal of Mechanical Design 144(7), 071704 (2022)
- [25] Nobari, A.H., Regenwetter, L., Picard, C., Han, L., Ahmed, F.: Optimize any topology: A foundation model for shape- and resolution-free structural topology optimization. In: The Thirty-ninth Annual Conference on Neural Information Processing Systems (2025). https://openreview.net/forum?id=eD0lYGQKn0
- [26] Nie, Z., Lin, T., Jiang, H., Kara, L.B.: Topologygan: Topology optimization using generative adversarial networks based on physical fields over the initial domain. Journal of Mechanical Design 143(3) (2021)
- [27] Nobari, A.H., Giannone, G., Regenwetter, L., Ahmed, F.: NITO: Neural Implicit Fields for Resolution-free Topology Optimization (2024). https://arxiv.org/abs/2402.05073

- [28] Mazé, F., Ahmed, F.: Diffusion models beat gans on topology optimization. In: Proceedings of the AAAI Conference on Artificial Intelligence (AAAI), Washington, DC (2023). https://arxiv.org/abs/2208.09591
- [29] Giannone, G., Srivastava, A., Winther, O., Ahmed, F.: Aligning optimization trajectories with diffusion models for constrained design generation. arXiv preprint arXiv:2305.18470 (2023)
- [30] Hu, J., He, Y., Xu, B., Wang, S., Lei, N., Luo, Z.: If-tonir: Iteration-free topology optimization based on implicit neural representations. Computer-Aided Design **167**, 103639 (2024) https://doi.org/10.1016/j.cad.2023.103639
- [31] Pardalos, P.M., Kovoor, N.: An algorithm for a singly constrained class of quadratic programs subject to upper and lower bounds. Mathematical Programming 46, 321–328 (1990)

Appendix A KKT Analysis of The Projection Problem

In this section, we will discuss the optimality conditions for the projection problem and provide a detailed derivation of the proposed approach. Before we continue solving the problem, we will formulate the Karush-Kuhn-Tucker (KKT) conditions for the projection problem (4) and refer to these KKT conditions in our solution:

$$g_j(\boldsymbol{\rho}_t) + (\boldsymbol{\delta} - \alpha \nabla f(\boldsymbol{\rho}_t))^T \nabla g_j(\boldsymbol{\rho}_t) - G_j \le 0 \quad \forall j \in \{1, \dots, m\},$$
 (A1)

$$l - \tilde{\rho}_i - \delta_i \leqslant 0, \quad \forall i \in \{1, \dots, n\},$$
 (A2)

$$\delta_i + \tilde{\rho}_i - u \leqslant 0, \quad \forall i \in \{1, \dots, n\},$$
 (A3)

$$2\delta_i + \sum_j \lambda_j (\nabla g_j(\boldsymbol{\rho}_t))_i + \nu_i - \mu_i = 0 \quad \forall i \in \{1, \dots, n\},$$
(A4)

$$\mu_i (l - \tilde{\rho}_i - \delta_i) = 0 \quad \forall i \in \{1, \dots, n\}, \tag{A5}$$

$$\nu_i \left(\delta_i - u + \tilde{\rho}_i \right) = 0 \quad \forall i \in \{1, \dots, n\}, \tag{A6}$$

$$\lambda_j \left((\boldsymbol{\delta} - \alpha \nabla f(\boldsymbol{\rho}_t))^T \nabla g_j(\boldsymbol{\rho}_t) - G_j + g_j(\boldsymbol{\rho}_t) \right) = 0 \quad \forall j \in \{1, \dots, m\},$$
(A7)

$$\lambda_j \ge 0, \quad \mu_i \geqslant 0, \quad \nu_i \geqslant 0 \quad \forall i \in \{1, \dots, n\}, \forall j \in \{1, \dots, m\}.$$
 (A8)

We can now perform a simple analysis of this problem to limit the solution space to some extent. From (A4) we have the stationary condition:

$$\delta_i = -\frac{\sum_j \lambda_j (\nabla g_j(\boldsymbol{\rho}_t))_i + \nu_i - \mu_i}{2}.$$
(A9)

Given (A8),(A5), and (A6) and the fact that l < u, when $\delta_i < -\frac{1}{2} \sum_j \lambda_j (\nabla g_j(\boldsymbol{\rho}_t))_i$, from (A5),(A6),(A8) we must have $\nu_i > 0$ and $\mu_i = 0$ and similarly when $\delta_i > -\frac{1}{2} \sum_i \lambda_j (\nabla g_j(\boldsymbol{\rho}_t))_i$, we must have $\mu_i > 0$ and $\nu_i = 0$, therefore we know:

$$\delta_i < -\frac{1}{2} \sum_j \lambda_j (\nabla g_j(\boldsymbol{\rho}_t))_i \to \delta_i = u - \tilde{\rho}_i,$$
 (A10)

$$\delta_i > -\frac{1}{2} \sum_j \lambda_j (\nabla g_j(\boldsymbol{\rho}_t))_i \to \delta_i = l - \tilde{\rho}_i.$$
 (A11)

We can see that for the terms in the stationary condition pertaining to the inequality constraints, we have three possibilities:

- Case 1: -½ ∑_j λ_j(∇g_j(ρ_t))_i > u ρ̃_i, which from (A2) yields δ_i < -½ ∑_j λ_j(∇g_j(ρ_t))_i and thereby from (A10), u ρ̃_i.
 Case 2: -½ ∑_j λ_j(∇g_j(ρ_t))_i < l ρ̃_i, which from (A3) yields δ_i > -½ ∑_j λ_j(∇g_j(ρ_t))_i and thereby from (A11), l ρ̃_i.
 Case 3: l ρ̃_i ≤ -½ ∑_j λ_j(∇g_j(ρ_t))_i ≤ u ρ̃_i, which then means that if δ_i < -½ ∑_j λ_j(∇g_j(ρ_t))_i, then δ_i = u ρ̃_i, which means δ_i ≥ -½ ∑_j λ_j(∇g_j(ρ_t))_i, which contradicts the assumption. Similarly if δ_i > -½ ∑_j λ_j(∇g_j(ρ_t))_i we will have a contradiction, which leaves only δ = -½ ∑_j λ_j(∇g_j(ρ_t))_i which leaves only $\delta_i = -\frac{1}{2} \sum_i \lambda_j (\nabla g_j(\boldsymbol{\rho}_t))_i$.

It is now evident that a three-case breakdown can give us a candidate solution for the projection. Let $y_j = -\frac{\lambda_j}{2}$ $\forall j \in \{1, \dots, m\}$, then a candidate solution to the problem can take the form (given $\mathbf{y} \in \mathbb{R}^{m}$):

$$\delta_{i}(\mathbf{y}) = \begin{cases} l - \tilde{\rho}_{i} & \text{if } \sum_{j} y_{j} (\nabla g_{j}(\boldsymbol{\rho}_{t}))_{i} < l - \tilde{\rho}_{i}, \\ \sum_{j} y_{j} (\nabla g_{j}(\boldsymbol{\rho}_{t}))_{i} & \text{if } l - \tilde{\rho}_{i} \leq \sum_{j} y_{j} (\nabla g_{j}(\boldsymbol{\rho}_{t}))_{i} \leq u - \tilde{\rho}_{i}, \\ u - \tilde{\rho}_{i} & \text{if } \sum_{j} y_{j} (\nabla g_{j}(\boldsymbol{\rho}_{t}))_{i} > u - \tilde{\rho}_{i}. \end{cases}$$
(A12)

Now Let:

$$\lambda_j = -2y_j, \tag{A13}$$

$$\mu_i = 2\max(0, l - \tilde{\rho}_i - \sum_j y_j(\nabla g_j(\boldsymbol{\rho}_t))_i), \tag{A14}$$

$$\nu_i = 2\max(0, \sum_j y_j(\nabla g_j(\boldsymbol{\rho}_t))_i - u + \tilde{\rho}_i). \tag{A15}$$

If there exists a $\mathbf{y}^* \in \mathbb{R}^m \leq 0$ such that the choice of $\lambda_j = -2y_j$ above, satisfies (A1) and (A7), we can show that the above choices for δ , μ_i , and ν_i satisfy all other KKT conditions. We can look at the inequality breakdowns of the proposed solution to prove this:

- Case 1: $\sum_{j} y_{j}(\nabla g_{j}(\boldsymbol{\rho}_{t}))_{i} < l \tilde{\rho}_{i}$, then $\delta_{i} = l \tilde{\rho}_{i}$, $\mu_{i} = 2\left(l \tilde{\rho}_{i} \sum_{j} y_{j}(\nabla g_{j}(\boldsymbol{\rho}_{t}))_{i}\right)$, $\nu_i = 0$, which satisfy (A2)-(A6) as well as (A8).
- $u_i = 0$, which satisfy (A2)-(A6) as well as (A8).

 Case 2: $\sum_j y_j(\nabla g_j(\boldsymbol{\rho}_t))_i > u \tilde{\rho}_i$, then $\delta_i = u \tilde{\rho}_i$, $\mu_i = 0$, $\nu_i = 2\left(\sum_j y_j(\nabla g_j(\boldsymbol{\rho}_t))_i u + \tilde{\rho}_i\right)$, which satisfy (A2)-(A6) as well as (A8).

 Case 3: $l \tilde{\rho}_i \leq \sum_j y_j(\nabla g_j(\boldsymbol{\rho}_t))_i \leq u \tilde{\rho}_i$, then $\delta_i = \sum_j y_j(\nabla g_j(\boldsymbol{\rho}_t))_i$, $\mu_i = \nu_i = 0$, which also satisfy (A2)-(A6) as well as (A8).

Thus, by convexity, δ^* defined by (A12) computed at \mathbf{y}^* is the solution to the problem. Thus, we see that the problem reduces to finding $\mathbf{y}^* \in \mathbb{R}^m \leq 0$ such that the choice of $\lambda_j = -2y_j$, satisfies (A1) and (A7). We will now propose an approach for solving this problem in the special case of one active constraint, as well as a general active set approach for solving the general problem.

Single Constraint Solution

Let m=1 in the projection sub-problem defined in (4). Then the solution form introduced in (A12) will take the simple form:

$$\delta_{i}(y) = \begin{cases} l - \tilde{\rho}_{i} & \text{if } y(\nabla g(\boldsymbol{\rho}_{t}))_{i} < l - \tilde{\rho}_{i}, \\ y(\nabla g(\boldsymbol{\rho}_{t}))_{i} & \text{if } l - \tilde{\rho}_{i} \leq y(\nabla g(\boldsymbol{\rho}_{t}))_{i} \leq u - \tilde{\rho}_{i}, \\ u - \tilde{\rho}_{i} & \text{if } y(\nabla g(\boldsymbol{\rho}_{t}))_{i} > u - \tilde{\rho}_{i}. \end{cases}$$
(A16)

Given the fact that we chose $\lambda = -2y$, from (A1) and (A7) we have:

$$y = 0 \Rightarrow \lambda = 0 \to (\boldsymbol{\delta} - \alpha \nabla f(\boldsymbol{\rho}_t))^T \nabla g_j(\boldsymbol{\rho}_t) - G_j + g_j(\boldsymbol{\rho}_t) \le 0, \tag{A17}$$

$$y < 0 \Rightarrow \lambda > 0 \rightarrow (\delta - \alpha \nabla f(\rho_t))^T \nabla g_i(\rho_t) - G_i + g_i(\rho_t) = 0.$$
 (A18)

This shows us that if y = 0 yields a feasible solution under the form described in the prior section, then the solution is simply as described in (A16) given y = 0 by convexity. Otherwise, the inequality constraint is active. Let $\Gamma_i = (\nabla g(\boldsymbol{\rho}_t))_i \, \delta_i(y)$, then for the active constraint case, by plugging in (A16) in (A18), we have:

$$\sum_{i} \Gamma_i - \hat{G} = 0, \tag{A19}$$

Where $\hat{G} = G - g(\boldsymbol{\rho}_t) + \alpha \nabla f(\boldsymbol{\rho}_t)^T \nabla g(\boldsymbol{\rho}_t)$. Note that for Γ we have:

$$\Gamma_{i}(y) = \begin{cases}
(\nabla g(\boldsymbol{\rho}_{t}))_{i}(l - \tilde{\rho}_{i}) & \text{if } y(\nabla g(\boldsymbol{\rho}_{t}))_{i} < l - \tilde{\rho}_{i}, \\
y((\nabla g(\boldsymbol{\rho}_{t}))_{i})^{2} & \text{if } l - \tilde{\rho}_{i} \leq y(\nabla g(\boldsymbol{\rho}_{t}))_{i} \leq u - \tilde{\rho}_{i}, \\
(\nabla g(\boldsymbol{\rho}_{t}))_{i}(u - \tilde{\rho}_{i}) & \text{if } y(\nabla g(\boldsymbol{\rho}_{t}))_{i} > u - \tilde{\rho}_{i}.
\end{cases}$$
(A20)

It is clear that $\Gamma_i(y)$ is a piecewise linear, monotone, non-decreasing function of y; thus making the left-hand side of (A19) a monotone, non-decreasing function of y. This means that if there exists a $y^* \in \mathbb{R} \leq 0$, it can be found through a computationally cheap and efficient binary search in the range $\left[\min_{i} \left\{\min\left(\frac{l-\tilde{\rho}_{i}}{(\nabla g(\boldsymbol{\rho}_{t}))_{i}}, \frac{u-\tilde{\rho}_{i}}{(\nabla g(\boldsymbol{\rho}_{t}))_{i}}\right)\right\}, 0\right]$. Thus, for the case of a single constraint (e.g., any nonlinear topology optimization under only volume constraint), the projection can be solved by first testing if y = 0 yields a feasible solution, and if not, performing a binary search in the aforementioned range. This finding and solution are inspired by the solution developed by Pardalos and Kovoor [31].

A.2 Efficiently Solving The General Problem

In general, to solve the above problem for the full set of problems, we will have to find m different y_j values. There are three possible scenarios that we can consider in our approach, which can be efficiently resolved:

- Single Constraint: If a single constraint is present, we can simply obtain y^* through a binary search as described in the prior section.
- Multiple Independent Constraints: If a given problem has m constraints that each involve a subset of the design variables $\varphi_j \subset \rho$, which are non-overlapping, i.e., $\varphi_k \cap \varphi_j = \emptyset$ for all $j \neq k$, then each constraint will only involve the specific subset of variables and thus the same analysis as done for a single constraint stands, and all $y*_j$ values can be obtain by m binary searches which can be done in paralle.
- Singular Active Constraint: In many real-world problems, the set of constraints that are active will typically be only one. This occurs when one active constraint is met exactly at the bound while all other constraints are not violated (this is a common occurrence in high-dimensional numerical problems such as TO). Given this, one can start with the assumption that the active set only contains one constraint and find by binary search y_j^* values for each constraint independently (which can be done efficiently in parallel), and if one such solution is feasible, the projection problem is solved by convexity.

The final case is when the problem involves multiple active constraints. In this scenario, we must find which constraints are active and solve the system of nonlinear equations to find the vector valued \mathbf{y}^* , which will be zero for inactive constraints and leads to a feasible $\delta(\mathbf{y}^*)$. Noting that in practice, we do not know if the problem is even feasible, we must construct an approach that is robust to uncertainties and makes finding the active set and dual variable values efficient. Thus, we take a regularization approach and rewrite the projection problem in an equivalent, constraint-violation regularization form.

A.2.1 The Regularized Projection Problem

We introduce a non-negative slack variable, $s_j \geq 0$, for each of the m general constraints. This variable measures the amount by which a constraint is violated. The new, regularized optimization problem is then formulated as:

$$\min_{\boldsymbol{\delta} \in \mathbb{R}^{N}, \mathbf{s} \in \mathbb{R}^{m}} \quad \frac{1}{2} \|\boldsymbol{\delta}\|_{2}^{2} + \frac{C}{2} \|\mathbf{s}\|_{2}^{2}$$
s.t. $l \leq \tilde{\rho}_{i} + \delta_{i} \leq u, \quad \forall i \in [N]$

$$g_{j}(\boldsymbol{\rho}_{t}) + (\boldsymbol{\delta} - \alpha \nabla f(\boldsymbol{\rho}_{t}))^{T} \nabla g_{j}(\boldsymbol{\rho}_{t}) - s_{j} \leq G_{j} \quad \forall j \in [m]$$

$$s_{i} > 0 \quad \forall j \in [m], \tag{A21}$$

where C > 0 is a large penalty parameter. This problem is a strictly convex Quadratic Program (QP) and is always feasible. As $C \to \infty$ and if the original problem (4) is feasible, the solution to this problem will have $\mathbf{s} = \mathbf{0}$, recovering the original projection. Otherwise, a solution that optimally balances minimizing the projection distance and the constraint violations will emerge. This, therefore, will enable us to practically solve the projection problem and not have to deal with the active set finding problem, which can be computationally less efficient. The proper value for C can be determined based on the constraint tolerances and the constraint gradients.

A.2.2 Optimality Conditions and Solution Form

In this section, we derive the optimality conditions for the regularized projection problem defined in (A21). The KKT conditions for the problem are:

$$g_j(\tilde{\boldsymbol{\rho}}) + \sum_i (\nabla g_j(\boldsymbol{\rho}_t))_i \delta_i - s_j - G_j \le 0, \quad \forall j \in [m]$$
 (A22)

$$l - \tilde{\rho}_i - \delta_i \le 0, \quad \forall i \in [N]$$
 (A23)

$$\delta_i + \tilde{\rho}_i - u \le 0, \quad \forall i \in [N] \tag{A24}$$

$$-s_i \le 0, \quad \forall j \in [m] \tag{A25}$$

$$\delta_i + \sum_j \lambda_j (\nabla g_j(\boldsymbol{\rho}_t))_i + \nu_i - \mu_i = 0, \quad \forall i \in [N]$$
(A26)

$$Cs_j - \lambda_j - \eta_j = 0, \quad \forall j \in [m]$$
 (A27)

$$\mu_i (l - \tilde{\rho}_i - \delta_i) = 0, \quad \forall i \in [N]$$
 (A28)

$$\nu_i \left(\delta_i - u + \tilde{\rho}_i \right) = 0, \quad \forall i \in [N] \tag{A29}$$

$$\lambda_j \left(g_j(\boldsymbol{\rho}_t) + (\boldsymbol{\delta} - \alpha \nabla f(\boldsymbol{\rho}_t))^T \nabla g_j(\boldsymbol{\rho}_t) - s_j - G_j \right) = 0, \quad \forall j \in [m]$$
 (A30)

$$\eta_i s_i = 0, \quad \forall j \in [m] \tag{A31}$$

$$\lambda_j \ge 0, \quad \mu_i \ge 0, \quad \nu_i \ge 0, \quad \eta_j \ge 0 \quad \forall i, j$$
 (A32)

As before, let $y_j = -\lambda_j/2$, then the analysis of the box constraints on δ allows us to express δ as the same piecewise function in (A12).

From (A27), (A31), and (A32), we can deduce a direct relationship between s_j and λ_j . from (A27), we have $Cs_j = \lambda_j + \eta_j$. If $\eta_j > 0$, then it implies from (A31) that $s_j = 0$, and thus $\lambda_j = -\eta_j$, which implies that $\lambda_j < 0$, which is in contradiction with (A32) and thus not possible, this implies that if $s_j = 0$, then since $\lambda_j = -\eta_j$, given (A32), the only solution is $\lambda_j = \eta_j = 0$. On the other hand if $s_j > 0$, then (A31) implies $\eta_j = 0$, and thus from (A27) we have $s_j = \frac{\lambda_j}{C} = \frac{-2y_j}{C}$. Note that this also stands in the case of s = 0, as we saw before, therefore we can deduce that in general:

$$s_j(\mathbf{y}) = \frac{-2y_j}{C}. (A33)$$

The problem now reduces to finding the vector $\mathbf{y} \leq \mathbf{0}$ that satisfies the complementarity condition (A30). Let us define a function $\mathbf{h}(\mathbf{y})$:

$$h_{j}(\mathbf{y}) = g_{j}(\boldsymbol{\rho}_{t}) + (\boldsymbol{\delta} - \alpha \nabla f(\boldsymbol{\rho}_{t}))^{T} \nabla g_{j}(\boldsymbol{\rho}_{t}) - s_{j}(\mathbf{y}) - G_{j}$$

$$= g_{j}(\boldsymbol{\rho}_{t}) + (\boldsymbol{\delta} - \alpha \nabla f(\boldsymbol{\rho}_{t}))^{T} \nabla g_{j}(\boldsymbol{\rho}_{t}) + \frac{2y_{j}}{C} - G_{j}.$$
(A34)

Thus, the solution is found by finding $\mathbf{y} \leq \mathbf{0}$ such that $h_j(\mathbf{y}) \leq \mathbf{0}$ and $y_j h_j(\mathbf{y}) = 0$ for all j.

To summarize, the solution to this convex QP is fully characterized by its KKT conditions. This analysis reveals that the entire problem can be reduced to finding a unique vector of dual variables $\mathbf{y} \in \mathbb{R}^m$. The optimal adjustment vector $\boldsymbol{\delta}^*$ and slack variables \mathbf{s}^* are functions of \mathbf{y}^* :

$$\delta_{i}^{*}(\mathbf{y}^{*}) = \begin{cases} l - \tilde{\rho}_{i} & \text{if } \sum_{j} y_{j}^{*}(\nabla g_{j}(\boldsymbol{\rho}_{t}))_{i} < l - \tilde{\rho}_{i}, \\ \sum_{j} y_{j}^{*}(\nabla g_{j}(\boldsymbol{\rho}_{t}))_{i} & \text{if } l - \tilde{\rho}_{i} \leq \sum_{j} y_{j}^{*}(\nabla g_{j}(\boldsymbol{\rho}_{t}))_{i} \leq u - \tilde{\rho}_{i}, \\ u - \tilde{\rho}_{i} & \text{if } \sum_{j} y_{j}^{*}(\nabla g_{j}(\boldsymbol{\rho}_{t}))_{i} > u - \tilde{\rho}_{i}, \end{cases}$$
(A35)

$$s_j^*(\mathbf{y}^*) = -\frac{y_j^*}{C}.\tag{A36}$$

Thus, $\mathbf{y}^* \in \mathbb{R}^m$ is a unique solution such that for all $j \in \{1, \dots, m\}$:

- 1. $y_j \le 0$
- 2. $h_j(\mathbf{y}) \le 0$
- 3. $y_i h_i(\mathbf{y}) = 0$

where the function $\mathbf{h}(\mathbf{y})$ is defined as:

$$h_j(\mathbf{y}) = \boldsymbol{\delta}(\mathbf{y})^T \nabla g_j(\boldsymbol{\rho}_t) + \frac{y_j}{C} - \hat{G}_j, \tag{A37}$$

where $\hat{G}_j = G_j - g_j(\boldsymbol{\rho}_t) + \alpha \nabla f(\boldsymbol{\rho}_t)^T \nabla g_j(\boldsymbol{\rho}_t)$ We can show that the function $\mathbf{h}(\mathbf{y})$ is strictly monotone with respect to \mathbf{y} , and thus guarantees the existence of a unique $\mathbf{y}^* \in \mathbb{R}^m$ which solves the regularized projection problem. We can prove this by analyzing its Jacobian matrix, $\mathbf{J}_{\mathbf{h}}$.

$$(J_{\mathbf{h}})_{jk} = \frac{\partial h_j}{\partial y_k} = \sum_i (\nabla g_j(\boldsymbol{\rho}_t))_i \frac{\partial \delta_i}{\partial y_k} + \frac{2}{C} \mathbb{I}_{jk}, \tag{A38}$$

where \mathbb{I}_{jk} is the Kronecker delta. The derivative $\frac{\partial \delta_i}{\partial y_k}$ is $I_i(\mathbf{y})(\nabla g_k(\boldsymbol{\rho}_t))_i$, where $I_i(\mathbf{y})$ is an indicator function that is 1 if $l - \tilde{\rho}_i \leq \sum_j y_j(\nabla g_j(\boldsymbol{\rho}_t))_i \leq u - \tilde{\rho}_i$ and 0 otherwise (See A35). The Jacobian is therefore:

$$(J_{\mathbf{h}})_{jk} = \sum_{i} I_{i}(\mathbf{y})(\nabla g_{j}(\boldsymbol{\rho}_{t}))_{i}(\nabla g_{k}(\boldsymbol{\rho}_{t}))_{i} + \frac{2}{C}\mathbb{I}_{jk}.$$
 (A39)

In matrix form, let \mathbf{A} $(m \times N)$ be the matrix of constraint gradients and $\mathbf{D}(\mathbf{y})$ be the diagonal matrix of indicators $I_i(\mathbf{y})$ $(N \times N)$. The Jacobian is:

$$\mathbf{J_h}(\mathbf{y}) = \mathbf{AD}(\mathbf{y})\mathbf{A}^T + \frac{2}{C}\mathbf{I}.$$
 (A40)

The matrix \mathbf{ADA}^T is symmetric and positive semi-definite. The matrix $\frac{2}{C}\mathbf{I}$ is symmetric and positive definite (since C > 0), making the sum strictly positive definite and therefore showing \mathbf{h} strictly monotone. This property guarantees that the problem has a unique solution \mathbf{y}^* , ensuring the robustness of the regularized formulation.

Finally, we must determine the appropriate bounds for C given the gradients of the constraints and a constraint tolerance. Let τ be a desired tolerance on the constraints, then C can be set to a value:

$$C = \frac{2\min_{j} \min_{i} \left\{ \min\left(\frac{l - \tilde{\rho}_{i}}{(\nabla g(\boldsymbol{\rho}_{t}))_{i}}, \frac{u - \tilde{\rho}_{i}}{(\nabla g(\boldsymbol{\rho}_{t}))_{i}}\right) \right\}}{\tau}$$
(A41)

This is the theoretical bound on constraint violation; however, in practice, smaller values for C may result in a zero value on $||s||_2$. In our approach, we keep C constant at 10^{12} and solve the subproblems with this penalty value. In most cases, a sufficiently large C will enable solving the projection nearly perfectly. However, when an infeasible problem is faced, one can adjust C to establish a balance between constraint violations and projection.

A.2.3 Solving The Regularized Problem

To solve the regularized problem as described in the prior section, we will exploit the monotonicity that we saw to solve the problem and find the optimal projection efficiently. First we define a function $\Phi(y)$:

$$\Phi_i(\mathbf{y}) = \max(h_i(\mathbf{y}), 0) + \operatorname{sign}(\max(-h_i(\mathbf{y}), 0))y_i. \tag{A42}$$

Note that the root of this function, i.e., $\Phi(\mathbf{y}) = 0$, corresponds to the solution of the regularized projection problem (see prior section). Therefore, by finding the solution to $\Phi_j(\mathbf{y}) = \mathbf{0}$, we can effectively solve the optimization problem. To do this, we can use a semismooth Newton iteration. First, it is important to note that $\Phi_j(\mathbf{y})$ is a semismooth function of \mathbf{y} , since $\mathbf{h}(\mathbf{y})$ is a piecewise linear function (see (A37), thus semi-smooth, and the the max and sign functions in $\mathbf{\Phi}$ are also piecewise-linear and semi-smooth, thus $\mathbf{\Phi}$ is semismooth and the properties of a semismooth Newton method such as superlinear local convergence apply to this problem. Furthermore, we demonstrated the monotonicity of $\mathbf{h}(\mathbf{y})$, which will be useful in guaranteeing the global convergence of the semismooth Newton method we propose here. Before we continue, let us derive the Jacobian of $\mathbf{\Phi}$, which we will use in our Newton method. Given a solution, at iteration k, $\mathbf{y}^{(k)}$, of the proposed algorithm to solve this problem, we can compute $\mathbf{\delta}(\mathbf{y}^{(k)})$ using (A35) and then $\mathbf{h}(\mathbf{y}^{(k)})$ using (A37). Given these we can also compute $\mathbf{J}_{\mathbf{h}}(\mathbf{y}^{(k)})$ using (A40). Now let $I_{\Phi,j}(\mathbf{y}^{(k)})$ be the indicator function for the active set, meaning $I_{\Phi,j}(\mathbf{y}) = 1$ if $h_j(\mathbf{y}^{(k)}) > 0$ and $I_{\Phi,j}(\mathbf{y}) = 0$ otherwise. Let \mathbf{D}_{Φ} be the diagonal matrix of $I_{\Phi,j}(\mathbf{y}^{(k)})$ then the jacobian of $\mathbf{\Phi}(\mathbf{y}^{(k)})$ can be written as:

$$\mathbf{J}_{\Phi}(\mathbf{y}^{(k)}) = \mathbf{D}_{\Phi}\mathbf{J}_{\mathbf{h}}(\mathbf{y}^{(k)}) - \mathbf{I} + \mathbf{D}_{\Phi}$$
(A43)

Since $\mathbf{J_h}(\mathbf{y}^{(k)})$ is invertible (given it is SPD), $\mathbf{J_{\Phi}}(\mathbf{y}^{(k)})$ is also invertible and thus one can update the dual values with following update rule:

$$\mathbf{y}^{(k+1)} = \mathbf{y}^{(k)} - \alpha \,\mathbf{J}_{\Phi}(\mathbf{y}^{(k)})^{-1}\mathbf{\Phi} = \mathbf{y}^{(k)} - \gamma\mathbf{\Delta},\tag{A44}$$

where $0 < \gamma \le 1$ is a step size for the update. Note that $\gamma = 1$, is equivalent to a purely Newton update; however, a semismooth Newton scheme only guarantees local convergence; therefore, we propose finding γ with a linesearch approach to ensure global convergence. Let $M(\mathbf{y}) = \frac{1}{2} \|\mathbf{\Phi}(\mathbf{y})\|_2^2$, a merit function indicating closeness to the solution (which dictates $M(\mathbf{y}) = \mathbf{0}$). We propose determining the step size for the semismooth Newton method using a line search approach by ensuring the solution improves at each iteration. The proposed line

search algorithm is aligned with the standard Wolfe conditions measured for the merit function M. This gives us the proposed linesearch formulated as follows:

$$\gamma^* = \max_{\alpha} \gamma \tag{A45}$$

s.t.
$$M(\mathbf{y} - \gamma \mathbf{\Delta}) < M(\mathbf{y}) + c_1 \gamma \nabla M(\mathbf{y})$$
 (A46)

$$\nabla M(\mathbf{y} - \gamma \mathbf{\Delta}) \ge c_2 \nabla M(\mathbf{y}) \tag{A47}$$

$$0 < \gamma < 1 \tag{A48}$$

where $\nabla M(\mathbf{y}) = \mathbf{J}_{\Phi}(\mathbf{y}^{(k)})\mathbf{\Phi}^T$, noting that the cost of determining $\mathbf{\Phi}$ and $\mathbf{J}_{\Phi}(\mathbf{y}^{(k)})$ is relatively low given the linearized approximation, this line-search can be done in a computationally efficient binary search approach. The existence of γ^* is guaranteed by the fact that $\nabla M^T \mathbf{\Delta} < 0$ for all $\mathbf{\Phi} \neq \mathbf{0}$ (this can be shown with simple algebra skipped here for brevity). In our approach, we set $c_1 = 10^{-4}$ and $c_2 = 0.9$.

Note that in any case, if the number of constraints m is large, this approach will be prohibitively expensive given the need for an inverse Jacobian, and therefore, in our work, we operate under the assumption that the number of constraints is small enough to make this approach sensible. This is a common theme in many TO problems, which is what makes the proposed framework meaningful for TO problems.

A.3 Convergence Analysis

Let the objective function f and constraint functions g_j , $\forall j \in [m]$ in (4) be L-smooth, namely that $\|\nabla f(x) - \nabla f(y)\|_2 \le L_f \|x - y\|_2$, $\forall x, y \in \mathbb{R}^N$, then have the following for $x, y \in \mathbb{R}^N$:

$$f(y) - f(x) = \int_{0}^{1} \langle \nabla f(x + t \cdot (y - x)), y - x \rangle dt$$

$$= \left(\int_{0}^{1} \langle \nabla f(x + t \cdot (y - x)) - \nabla f(x), y - x \rangle dt \right) + \langle \nabla f(x), y - x \rangle$$

$$\leq \left(\int_{0}^{1} \|\nabla f(x + t \cdot (y - x)) - \nabla f(x)\|_{2} \cdot \|y - x\|_{2} dt \right) + \langle \nabla f(x), y - x \rangle \quad (A49)$$

$$\leq \left(\int_{0}^{1} t L_{f} \|y - x\|_{2}^{2} dt \right) + \langle \nabla f(x), y - x \rangle$$

$$= \frac{L_{f}}{2} \|y - x\|_{2}^{2} + \nabla f(x)^{T} \cdot (y - x)$$

This is true for both f and g_j . Now let $\rho_{t+1} = \Pi_{\Omega}(\rho_t - \alpha \nabla f) = \rho_t - \alpha \nabla f + \delta^*$ be the update at each iteration, where δ^* is the solution of (4). We can use (A49) to obtain:

$$f(\boldsymbol{\rho}_{t+1}) - f(\boldsymbol{\rho}_{t}) \leq \frac{L_{f}}{2} \|\boldsymbol{\rho}_{t+1} - \boldsymbol{\rho}_{t}\|_{2}^{2} + \nabla f(\boldsymbol{\rho}_{t})^{T} \cdot (\boldsymbol{\rho}_{t+1} - \boldsymbol{\rho}_{t})$$

$$\leq \frac{L_{f}}{2} \|\boldsymbol{\rho}_{t+1} - \boldsymbol{\rho}_{t}\|_{2}^{2} - \frac{1}{\alpha} (\boldsymbol{\rho}_{t+1} - \boldsymbol{\rho}_{t} - \boldsymbol{\delta}^{*})^{T} \cdot (\boldsymbol{\rho}_{t+1} - \boldsymbol{\rho}_{t})$$

$$\leq (\frac{L_{f}}{2} - \frac{1}{\alpha}) \|\boldsymbol{\rho}_{t+1} - \boldsymbol{\rho}_{t}\|_{2}^{2} + \frac{1}{\alpha} \boldsymbol{\delta}^{*T} \cdot (\boldsymbol{\rho}_{t+1} - \boldsymbol{\rho}_{t})$$
(A50)

Now, assuming $\rho_t \in \hat{\Omega}_{t+1}$, meaning the current design variable at iteration t+1 is in the linearized convex feasible set, then by convexity of $\hat{\Omega}_{t+1}$, we have $\boldsymbol{\delta}^{*T}.(\boldsymbol{\rho}_{t+1}-\boldsymbol{\rho}_t) \leq 0$, since if $\boldsymbol{\rho}_{t+1} \in \hat{\Omega}_{t+1}$, then (4), will yield $\boldsymbol{\delta}^* = \mathbf{0}$ and other wise the correction to the convex set from a point outside the set will yield $\boldsymbol{\delta}^{*T}.(\boldsymbol{\rho}_{t+1}-\boldsymbol{\rho}_t) \leq 0$. Thus, we have:

$$f(\rho_{t+1}) - f(\rho_t) \le \left(\frac{L_f}{2} - \frac{1}{\alpha}\right) \|\rho_{t+1} - \rho_t\|_2^2$$
 (A51)

Now let $L = \frac{1}{\alpha} - \frac{L_f}{2}$, for a small enough $\alpha < \frac{2}{L_f}$, L > 0 and we can sum the iteration over K steps, yielding the following inequality:

$$L\sum_{t=0}^{K-1} \|\boldsymbol{\rho}_{t+1} - \boldsymbol{\rho}_t\|_2^2 \le f(\boldsymbol{\rho}_0) - f(\boldsymbol{\rho}_K). \tag{A52}$$

Now, assuming within the box constraint range of design variables, the objective f is bounded, namely $f(\rho) \leq f_{\text{inf}}$, then we have:

$$\sum_{t=0}^{K-1} \|\boldsymbol{\rho}_{t+1} - \boldsymbol{\rho}_t\|_2^2 \le \frac{f(\boldsymbol{\rho}_0) - f_{\inf}}{L}, \tag{A53}$$

which means that there must exist one iteration in which $\|\rho_{t+1} - \rho_t\|_2^2 \le \frac{f(\rho_0) - f_{\text{inf}}}{L K}$. In other words:

$$\min_{t} \|\boldsymbol{\rho}_{t+1} - \boldsymbol{\rho}_{t}\|_{2} \le \sqrt{\frac{f(\boldsymbol{\rho}_{0}) - f_{\inf}}{L K}}, \tag{A54}$$

which implies that the Euclidean norm of the design variables update converges at a rate of $O(\frac{1}{\sqrt{K}})$.

Note that in our analysis, we made two crucial assumptions. First, we assumed that the design variables at each iteration are in the feasible set. This assumption will hold for linear constraints at all times, since the convex set for the projection is constant throughout the iterations. Noting that the most common constraints in TO problems, namely volume constraints, are linear, this assumption is valid in most cases. However, for the linearized approximation of nonlinear constraints, this may not always be true, but one can expect that for a well-behaved problem, the iterations will result in increasingly smaller changes, which make the linear approximations increasingly more accurate, hence leading to iterations where the assumption will hold after some initial large updates. To prevent non-convergence in our approach, if the constraint violations are above the tolerance for the Newton iteration, we fall back to the same minimum step size as used in the starting iteration. The second assumption that was made here was the L-smooth nature of the objective function. We argue that this assumption should be true in most TO problems based on FEA solutions. In the section that follows, we formalize this argument.

A.4 On The L-Smooth Assumption of The Objective Function

In most TO problems, the objective function is defined based on solutions from an FEA solver. Thus, it is safe to assume that the objective function can be formulated as a polynomial expression of the solution to the FEA problem. Therefore, if we can show L-smoothness of the solution to the FEA problem, it can be shown that, in most cases, the objective function will also be L-smooth. Let $K(\rho)$ be the resulting matrix of equations for FEA based on some design variables ρ . Let the solution to this system of equations be $u = K^{-1}f$, where f is the forcing term, assumed to be constant here for simplicity. Then, if we show that for any arbitrary $q \in \mathbb{R}^N$, the function $t(\rho) = q^T u = q^T K^{-1}f$ is L-smooth, then it can be easily inferred that any multi-linear polynomial function of u will be L-smooth as well (inferred from the smoothness of the polynomial form itself). To show this, we formulate the Hessian of the proposed test function t. The gradient of the function can be written as:

$$\frac{\partial t}{\partial \rho_i} = -q^T K^{-1} \frac{\partial K}{\partial \rho_i} K^{-1} f \tag{A55}$$

given the identity $\frac{\partial K^{-1}}{\partial \rho_i} = -K^{-1} \frac{\partial K}{\partial \rho_i} K^{-1}$ we have:

$$\frac{\partial^2 t}{\partial \rho_i \partial \rho_j} = q^T \left[K^{-1} \frac{\partial^2 K}{\partial \rho_j \partial \rho_i} K^{-1} - K^{-1} \frac{\partial K}{\partial \rho_j} K^{-1} \frac{\partial K}{\partial \rho_i} K^{-1} - K^{-1} \frac{\partial K}{\partial \rho_i} K^{-1} \frac{\partial K}{\partial \rho_j} K^{-1} \right] f.$$

We can assume elements in K are smooth functions of ρ , which is commonly the case, for example, the SIMP approach elements of K are a polynomial penalty function of the densities, which sometimes also involve a smooth continuous heavy-side projection. Under this assumption and the fact that we assume said smooth functions are defined and finite within the box-constrained values of ρ , we expect:

$$\|\frac{\partial K}{\partial \rho_i}\| \le C_1, \quad \forall i \in [N]$$
 (A56)

$$\|\frac{\partial^2 K}{\partial \rho_j \partial \rho_i}\| \le C_2, \quad \forall i, j \in [N].$$
 (A57)

Combined with the fact that we assume K^{-1} exists for all $\rho \in \Omega$, and the feasible set Ω is non-empty and bounded, $||K^{-1}||$ will also be bounded within the feasible space of the problem, namely $||K^{-1}|| \le C_3$. Thus, can say that the Hessian matrix elements are bounded as well, $\left|\frac{\partial^2 t}{\partial \rho_i \partial \rho_j}\right| \le C_4$, making the objective function L-smooth:

$$\|\nabla t(x) - \nabla t(y)\|_2 \le L_t \|x - y\|_2, \quad \forall x, y \in \Omega,$$
 (A58)

for some constant L_t . In general, although the analysis above is true when K is not ill-conditioned, if in any part of the feasible space the resulting system becomes ill-conditioned, the Lipschitz constant can be huge and thus makes the step size prohibitively small for the optimization. Given this and the fact that finding the constant for any arbitrary TO problem is not trivial, we take a more pragmatic approach to setting the step size in our algorithm. We propose to use a local approximation $\hat{L}_f = \frac{\|\nabla f(\rho_t) - \nabla f(\rho_{t-1})\|}{\|\rho_t - \rho_{t-1}\|}$ at each iteration t, and set the step size of the gradient descent to a small enough $\alpha = \frac{1}{\hat{L}_f}$, at each step. Furthermore, when a problem is ill-conditioned, we fall back to a step size that limits maximum variable change in our approach.

A.5 Full Experimental Results

In this section, we provide detailed plots and visualizations of the results of the different optimization problems. In the main body, we only highlight the main findings and primary results to demonstrate the different observations we make in our experiments.

A.5.1 Volume Constrained Minimum Compliance

Here we provide the full set of results for each of the resolutions. For each resolution, we provide results in the sections that follow.

Coarse Mesh Results

Here we provide figures for the results of running each optimizer for the coarse 128×64 mesh.

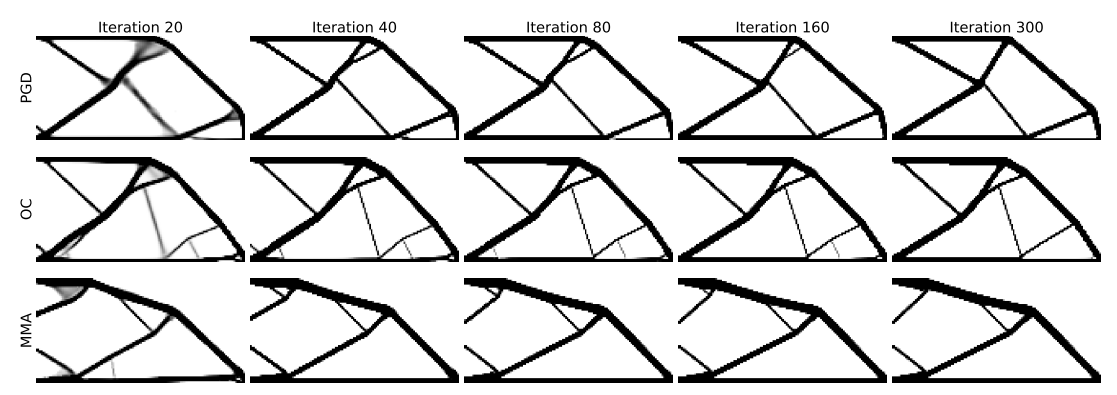


Fig. A1: The designs each optimizer produces at five log-spaced iterations. Here, we visualize the solutions each optimizer produces for the volume-constrained minimum compliance problem on the cantilever beam problem with a volume fraction target of 0.2.

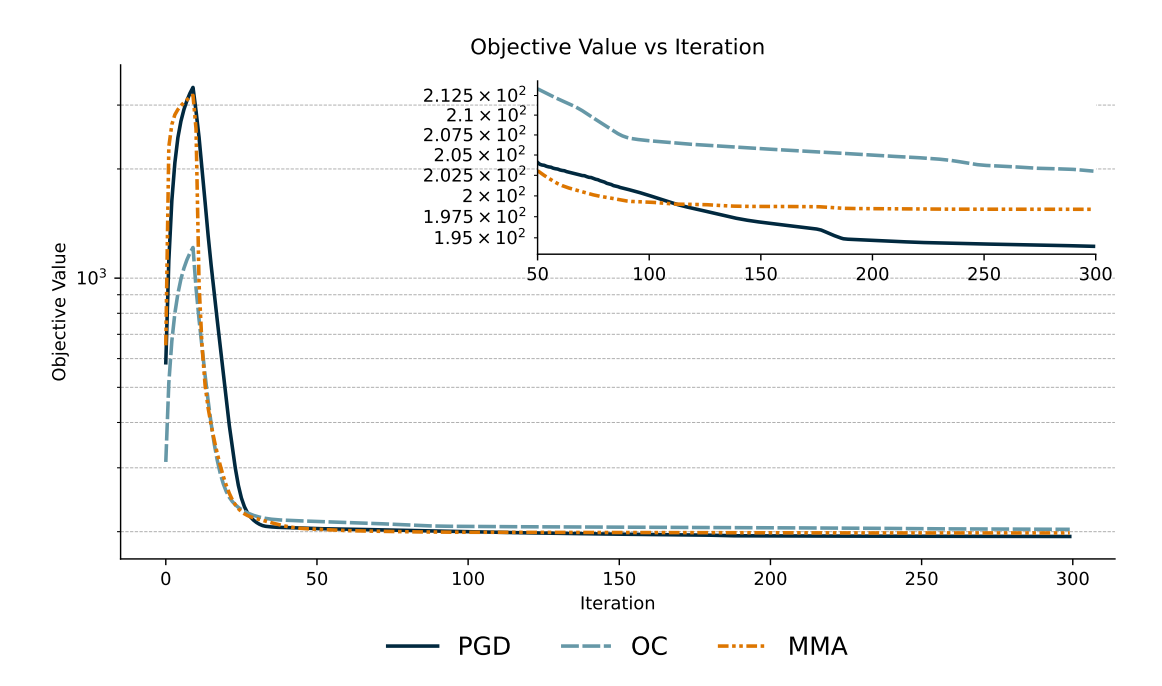


Fig. A2: The value of the objective function measured at each iteration for all solvers. The plots show a 10-iteration moving average to remove noise and make the plots easier to follow. The inset plot provides a rescaled plot for the same axes after 50 iterations, where solvers have stabilized and the plot is scaled more suitably.

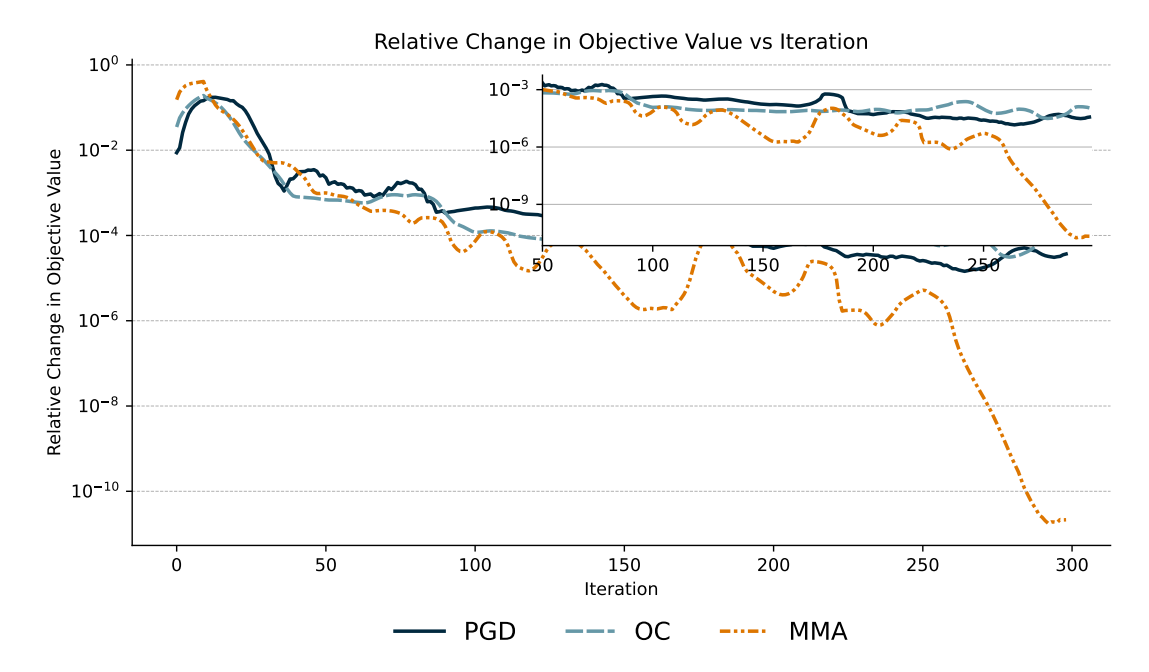


Fig. A3: The value of the relative change in the objective function measured at each iteration for all solvers. The plots show a 10-iteration moving average to remove noise and make the plots easier to follow. The inset plot provides a rescaled plot for the same axes after 50 iterations, where solvers have stabilized and the plot is scaled more suitably.

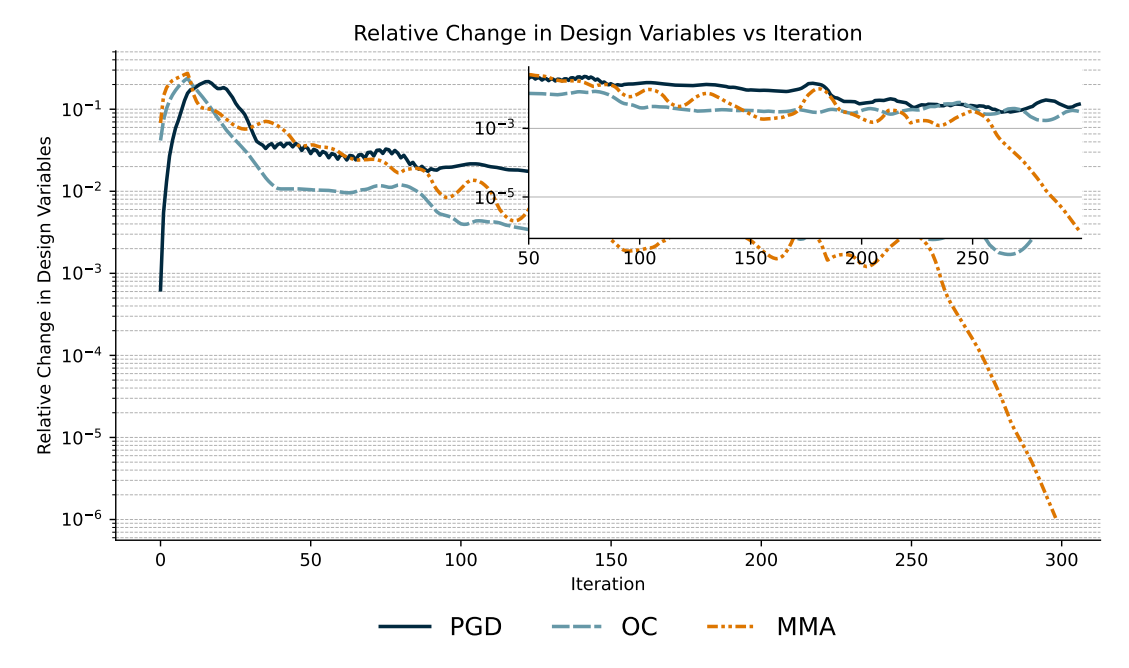


Fig. A4: The value of the relative change in the design variable norm measured at each iteration for all solvers. The plots show a 10-iteration moving average to remove noise and make the plots easier to follow. The inset plot provides a rescaled plot for the same axes after 50 iterations, where solvers have stabilized and the plot is scaled more suitably.

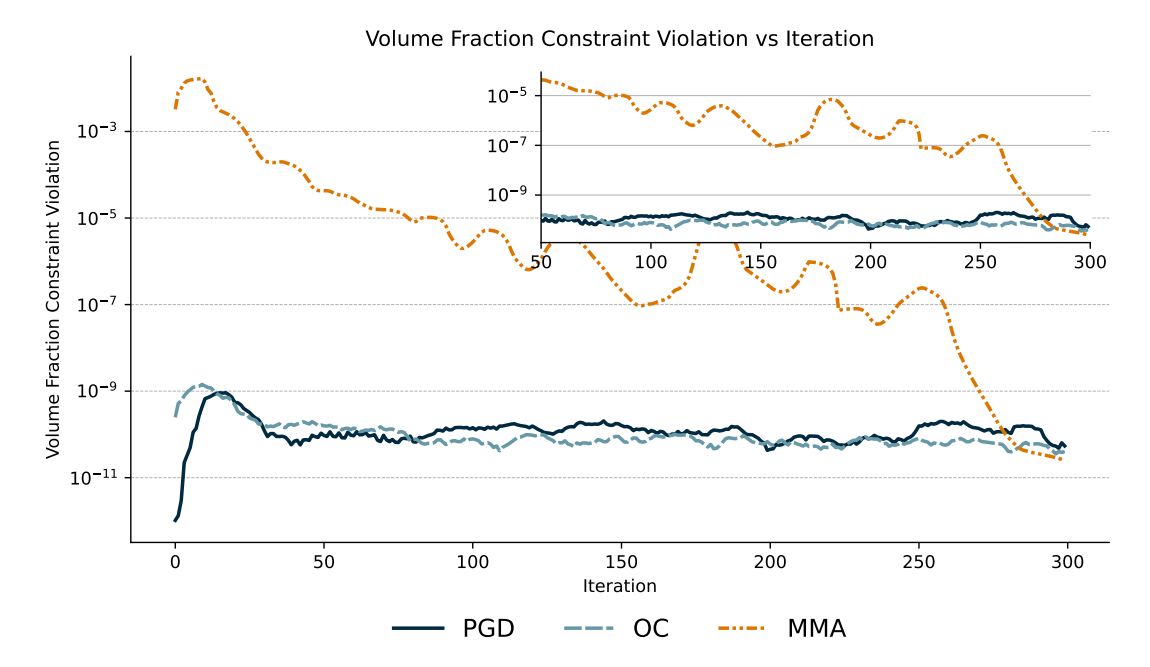


Fig. A5: The value of the constraint violation at each iteration for all solvers. The plots show a 10-iteration moving average to remove noise and make the plots easier to follow. The inset plot provides a rescaled plot for the same axes after 50 iterations, where solvers have stabilized and the plot is scaled more suitably.

Medium Mesh Results

Here we provide figures for the results of running each optimizer for the coarse 256×128 mesh.

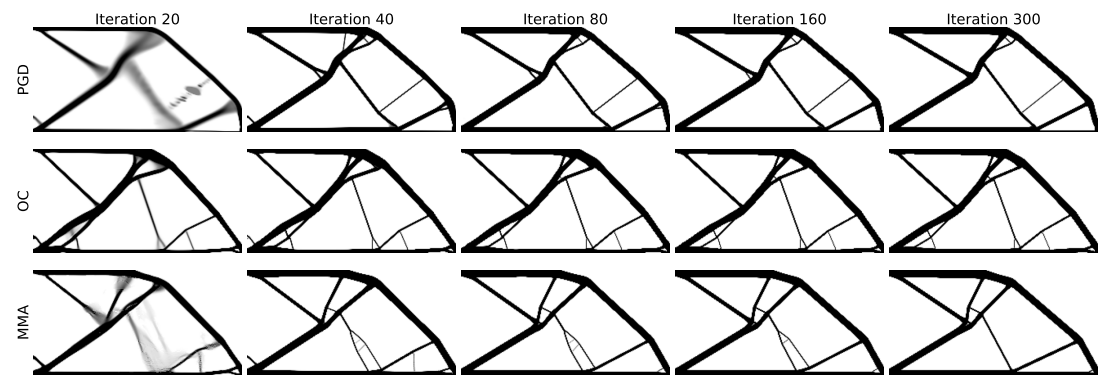


Fig. A6: The designs each optimizer produces at five log-spaced iterations. Here, we visualize the solutions each optimizer produces for the volume-constrained minimum compliance problem on the cantilever beam problem with a volume fraction target of 0.2.

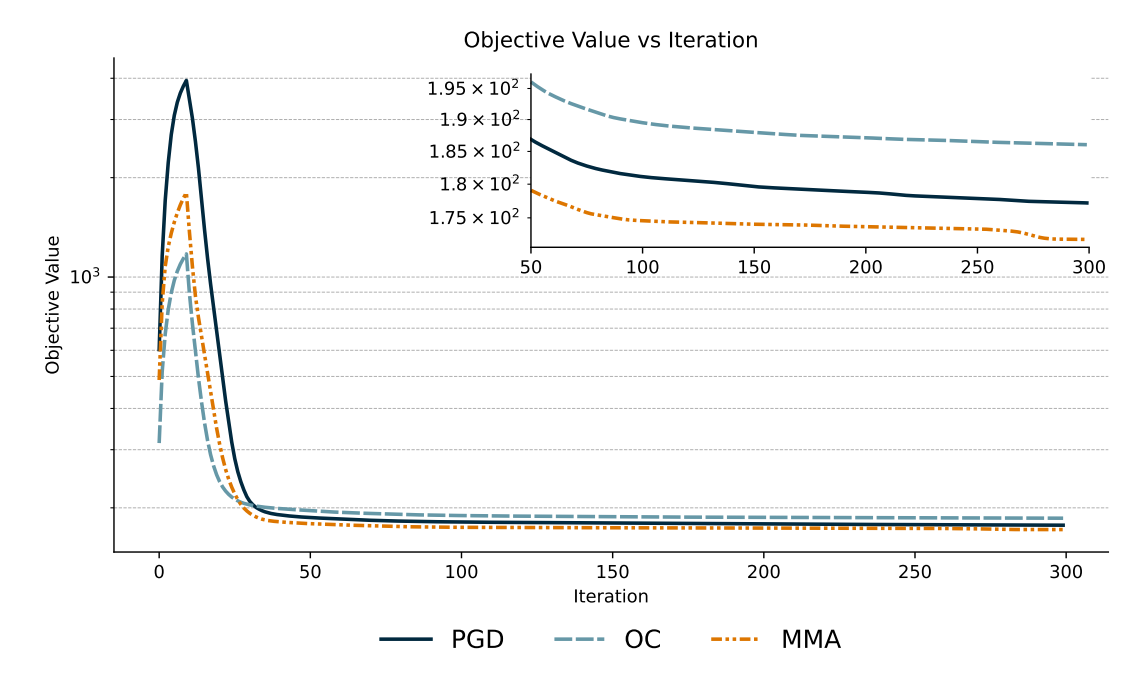


Fig. A7: The value of the objective function measured at each iteration for all solvers. The plots show a 10-iteration moving average to remove noise and make the plots easier to follow. The inset plot provides a rescaled plot for the same axes after 50 iterations, where solvers have stabilized and the plot is scaled more suitably.

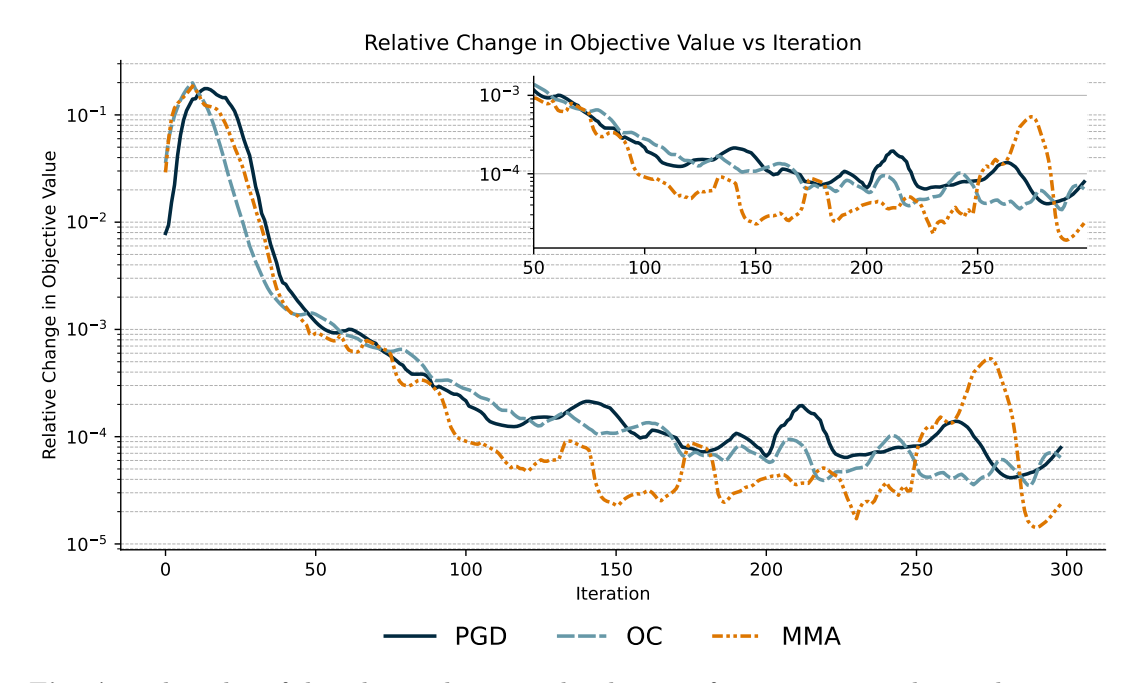


Fig. A8: The value of the relative change in the objective function measured at each iteration for all solvers. The plots show a 10-iteration moving average to remove noise and make the plots easier to follow. The inset plot provides a rescaled plot for the same axes after 50 iterations, where solvers have stabilized and the plot is scaled more suitably.

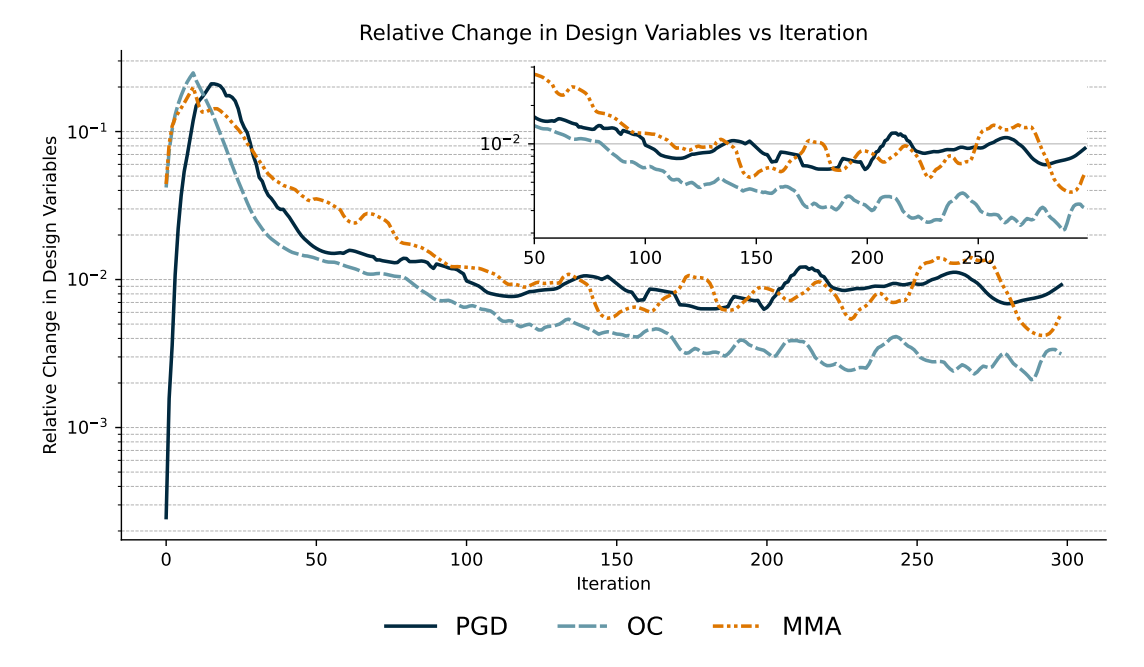


Fig. A9: The value of the relative change in the design variable norm measured at each iteration for all solvers. The plots show a 10-iteration moving average to remove noise and make the plots easier to follow. The inset plot provides a rescaled plot for the same axes after 50 iterations, where solvers have stabilized and the plot is scaled more suitably.

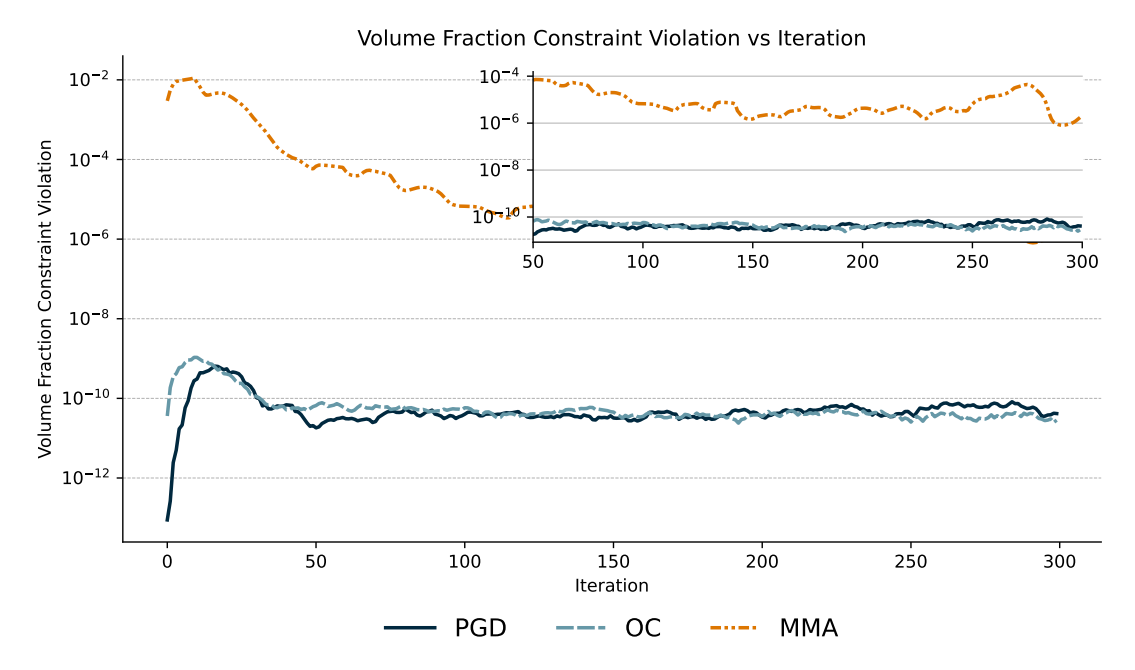


Fig. A10: The value of the constraint violation at each iteration for all solvers. The plots show a 10-iteration moving average to remove noise and make the plots easier to follow. The inset plot provides a rescaled plot for the same axes after 50 iterations, where solvers have stabilized and the plot is scaled more suitably.

Fine Mesh Results

Here we provide figures for the results of running each optimizer for the coarse 512×256 mesh.

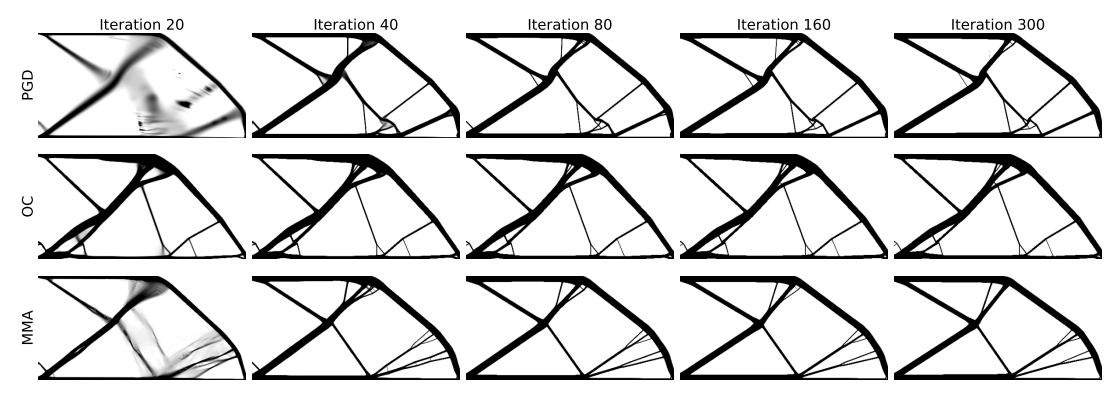


Fig. A11: The designs each optimizer produces at five log-spaced iterations. Here, we visualize the solutions each optimizer produces for the volume-constrained minimum compliance problem on the cantilever beam problem with a volume fraction target of 0.2.

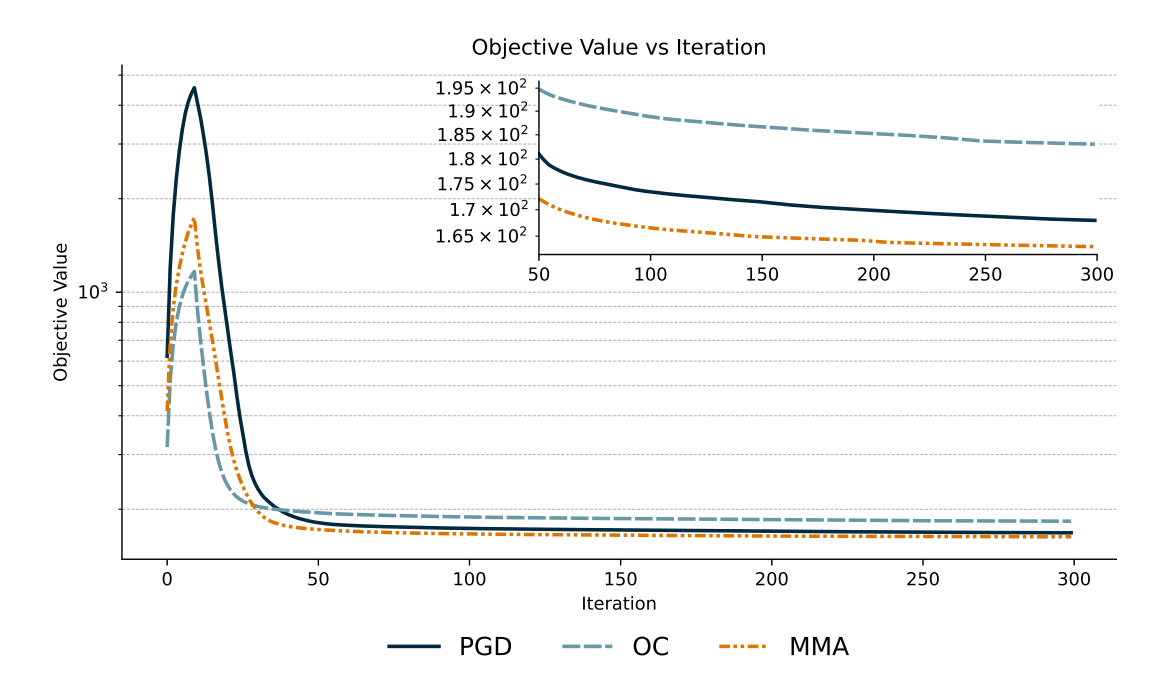


Fig. A12: The value of the objective function measured at each iteration for all solvers. The plots show a 10-iteration moving average to remove noise and make the plots easier to follow. The inset plot provides a rescaled plot for the same axes after 50 iterations, where solvers have stabilized and the plot is scaled more suitably.

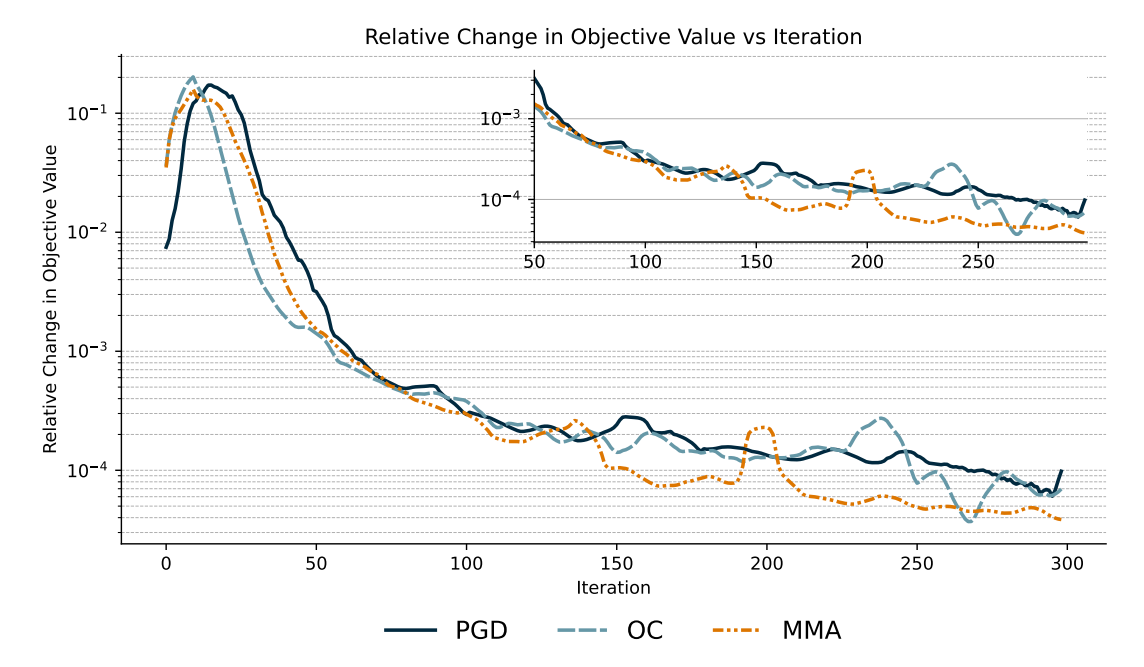


Fig. A13: The value of the relative change in the objective function measured at each iteration for all solvers. The plots show a 10-iteration moving average to remove noise and make the plots easier to follow. The inset plot provides a rescaled plot for the same axes after 50 iterations, where solvers have stabilized and the plot is scaled more suitably.

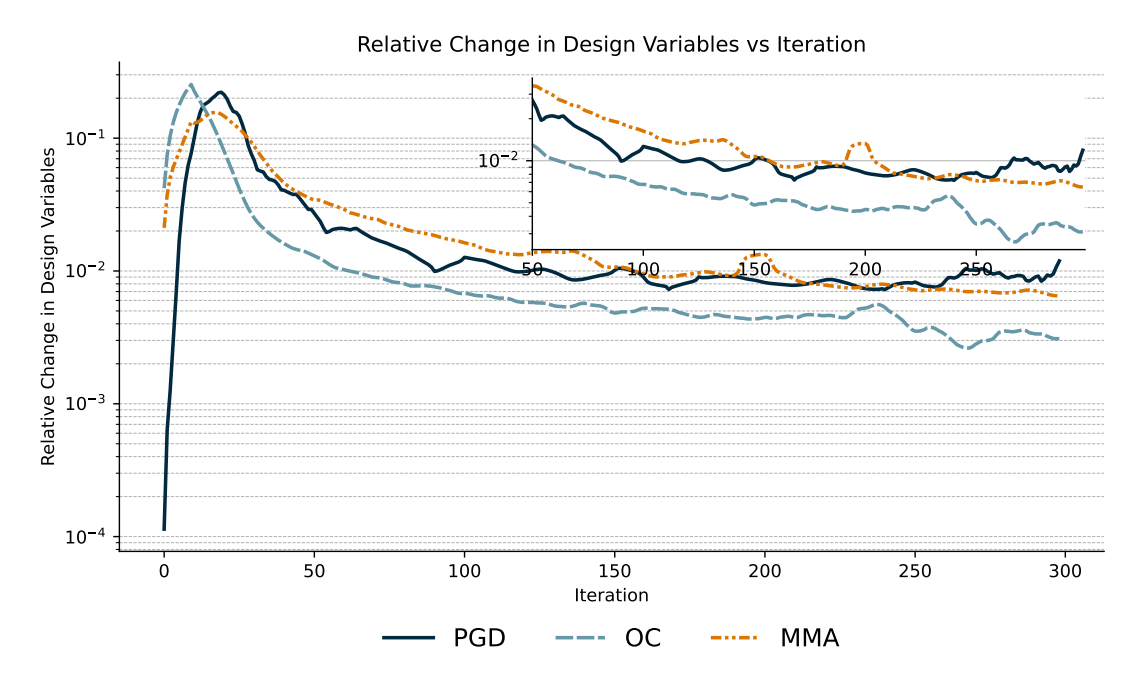


Fig. A14: The value of the relative change in the design variable norm measured at each iteration for all solvers. The plots show a 10-iteration moving average to remove noise and make the plots easier to follow. The inset plot provides a rescaled plot for the same axes after 50 iterations, where solvers have stabilized and the plot is scaled more suitably.

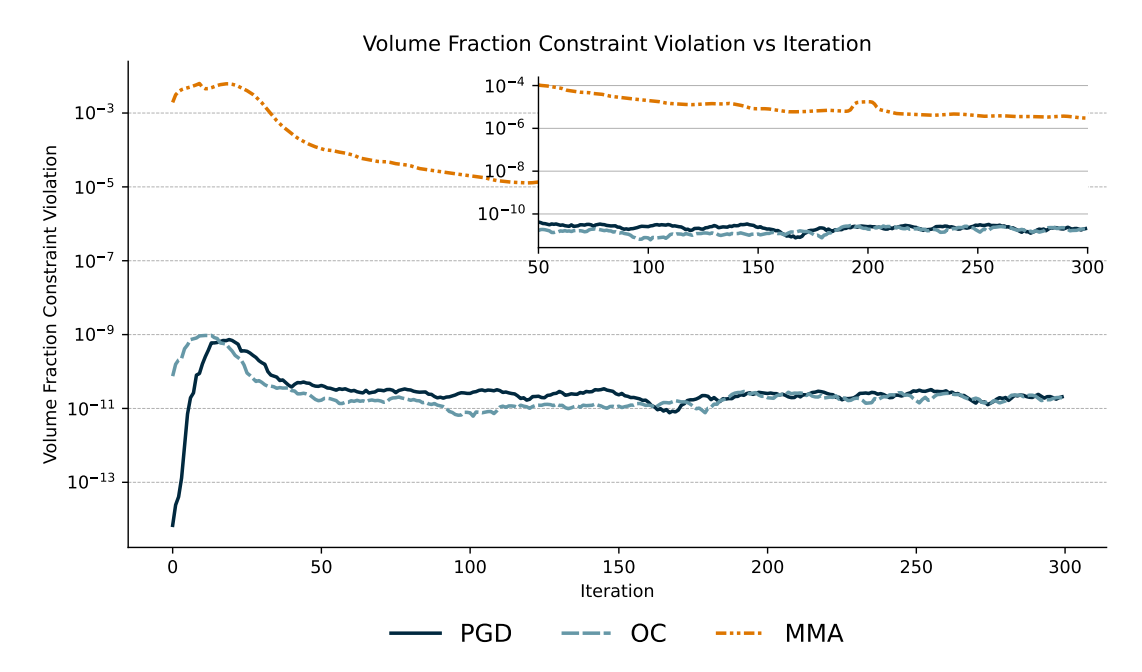


Fig. A15: The value of the constraint violation at each iteration for all solvers. The plots show a 10-iteration moving average to remove noise and make the plots easier to follow. The inset plot provides a rescaled plot for the same axes after 50 iterations, where solvers have stabilized and the plot is scaled more suitably.

A.5.2 Compliance Constrained Minimum Volume

Here we provide the full set of results for each of the resolutions. For each resolution, we provide results in the sections that follow.

Coarse Mesh Results

Here we provide figures for the results of running each optimizer for the coarse 128×64 mesh.

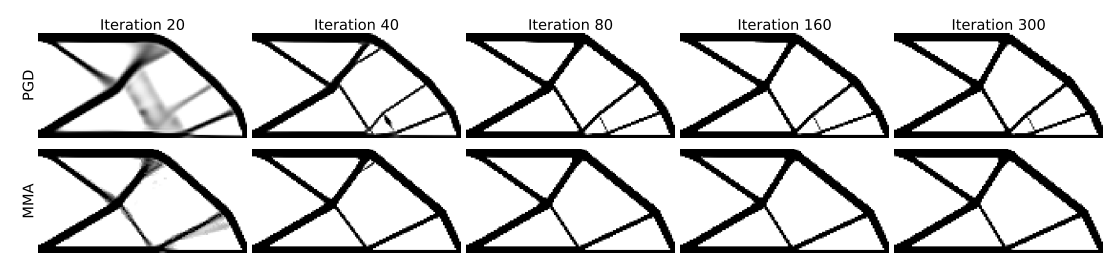


Fig. A16: The designs each optimizer produces at five log-spaced iterations. Here, we visualize the solutions each optimizer produces for the compliance-constrained minimum volume problem on the cantilever beam problem with a volume fraction target of 0.2.

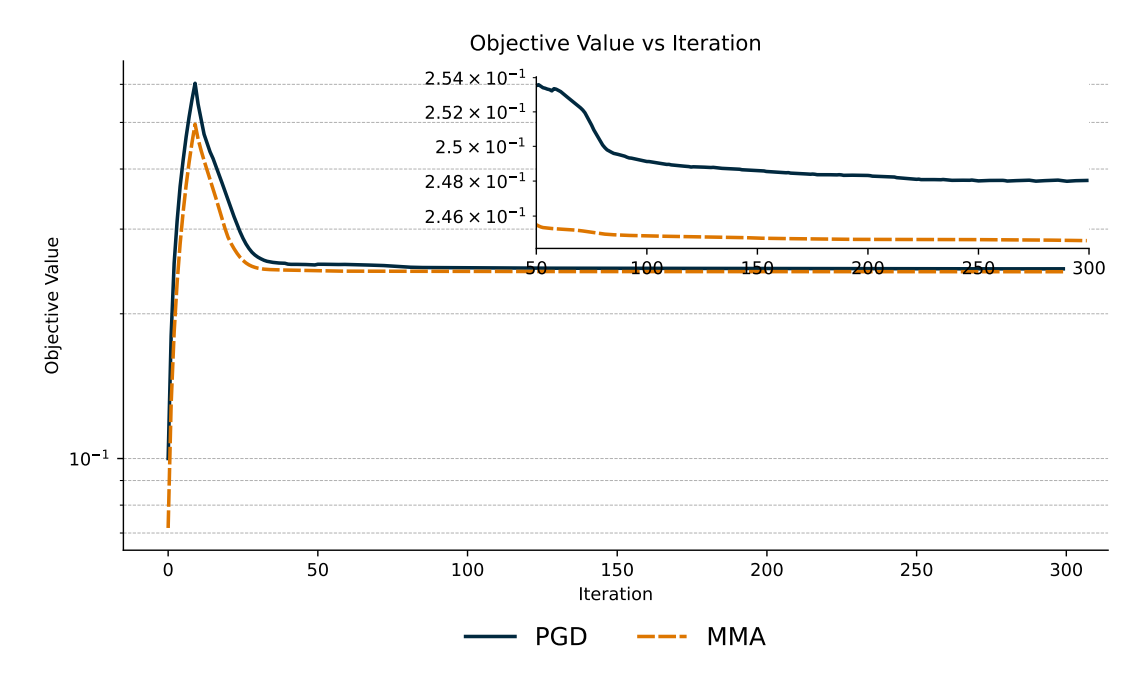


Fig. A17: The value of the objective function measured at each iteration for all solvers. The plots show a 10-iteration moving average to remove noise and make the plots easier to follow. The inset plot provides a rescaled plot for the same axes after 50 iterations, where solvers have stabilized and the plot is scaled more suitably.

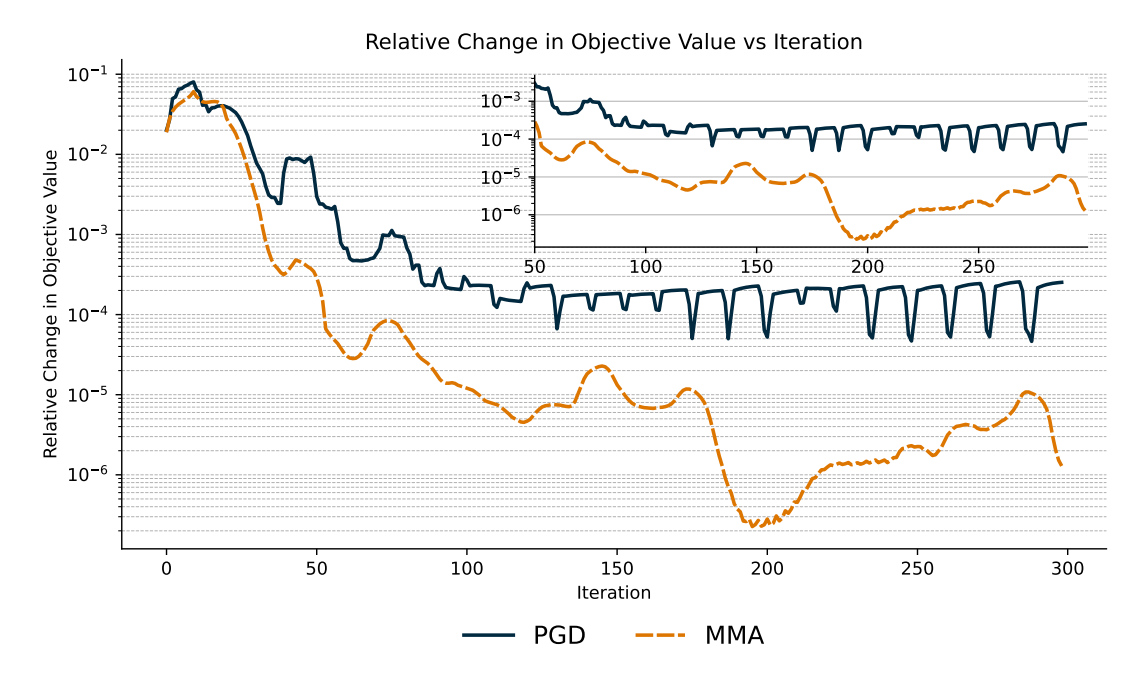


Fig. A18: The value of the relative change in the objective function measured at each iteration for all solvers. The plots show a 10-iteration moving average to remove noise and make the plots easier to follow. The inset plot provides a rescaled plot for the same axes after 50 iterations, where solvers have stabilized and the plot is scaled more suitably.

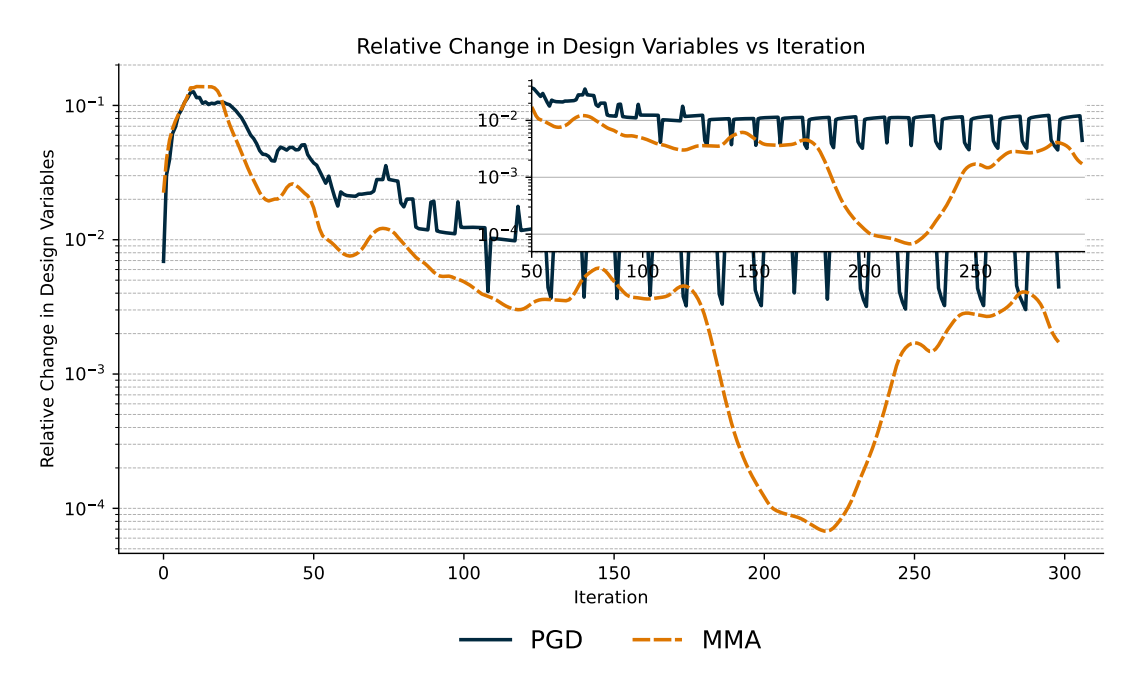


Fig. A19: The value of the relative change in the design variable norm measured at each iteration for all solvers. The plots show a 10-iteration moving average to remove noise and make the plots easier to follow. The inset plot provides a rescaled plot for the same axes after 50 iterations, where solvers have stabilized and the plot is scaled more suitably.

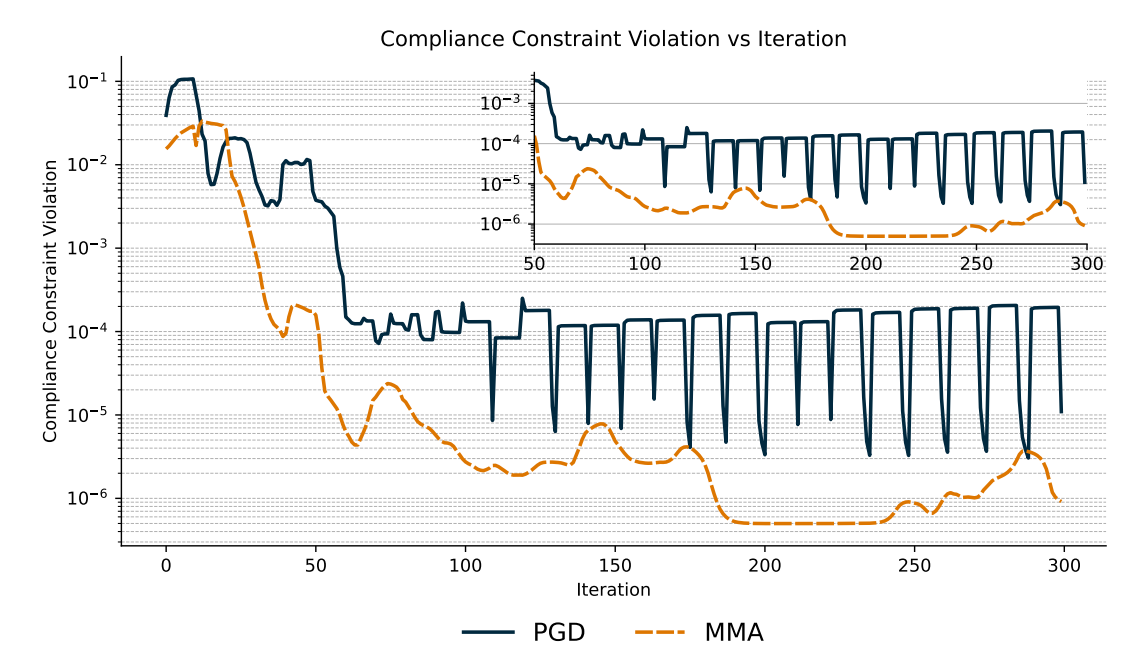


Fig. A20: The value of the constraint violation at each iteration for all solvers. The plots show a 10-iteration moving average to remove noise and make the plots easier to follow. The inset plot provides a rescaled plot for the same axes after 50 iterations, where solvers have stabilized and the plot is scaled more suitably.

Medium Mesh Results

Here we provide figures for the results of running each optimizer for the coarse 256×128 mesh.

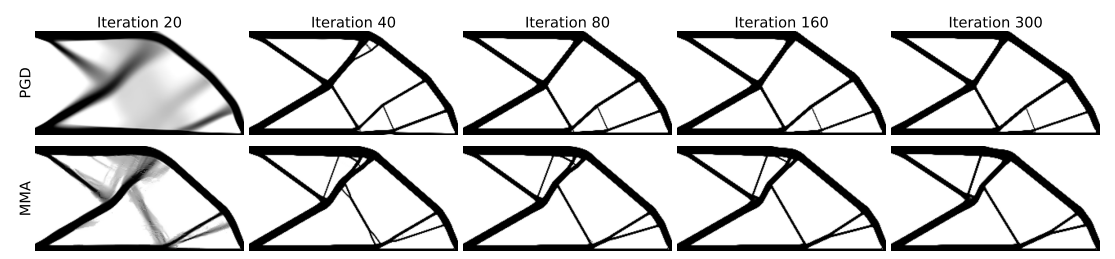


Fig. A21: The designs each optimizer produces at five log-spaced iterations. Here, we visualize the solutions each optimizer produces for the compliance-constrained minimum volume problem on the cantilever beam problem with a volume fraction target of 0.2.

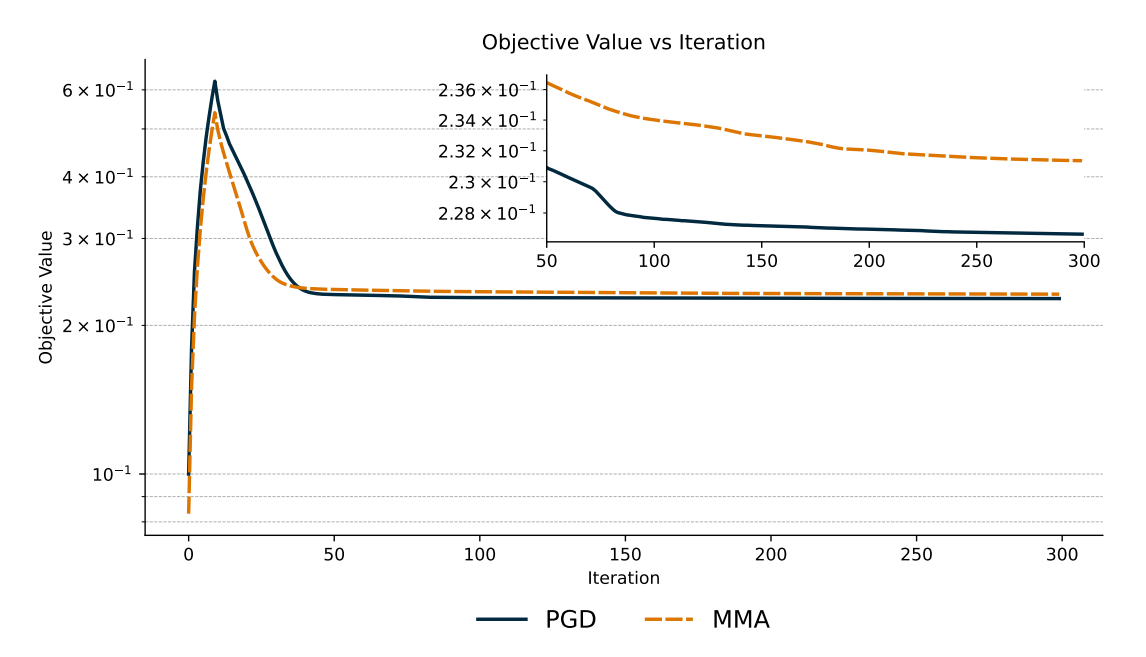


Fig. A22: The value of the objective function measured at each iteration for all solvers. The plots show a 10-iteration moving average to remove noise and make the plots easier to follow. The inset plot provides a rescaled plot for the same axes after 50 iterations, where solvers have stabilized and the plot is scaled more suitably.

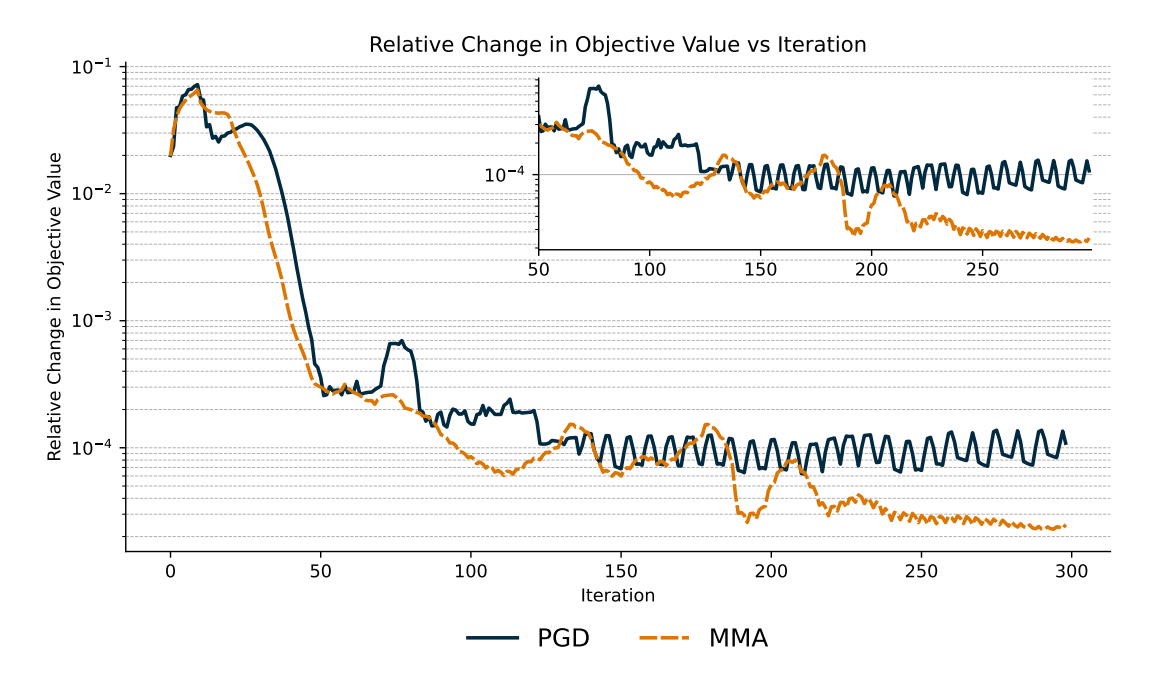


Fig. A23: The value of the relative change in the objective function measured at each iteration for all solvers. The plots show a 10-iteration moving average to remove noise and make the plots easier to follow. The inset plot provides a rescaled plot for the same axes after 50 iterations, where solvers have stabilized and the plot is scaled more suitably.

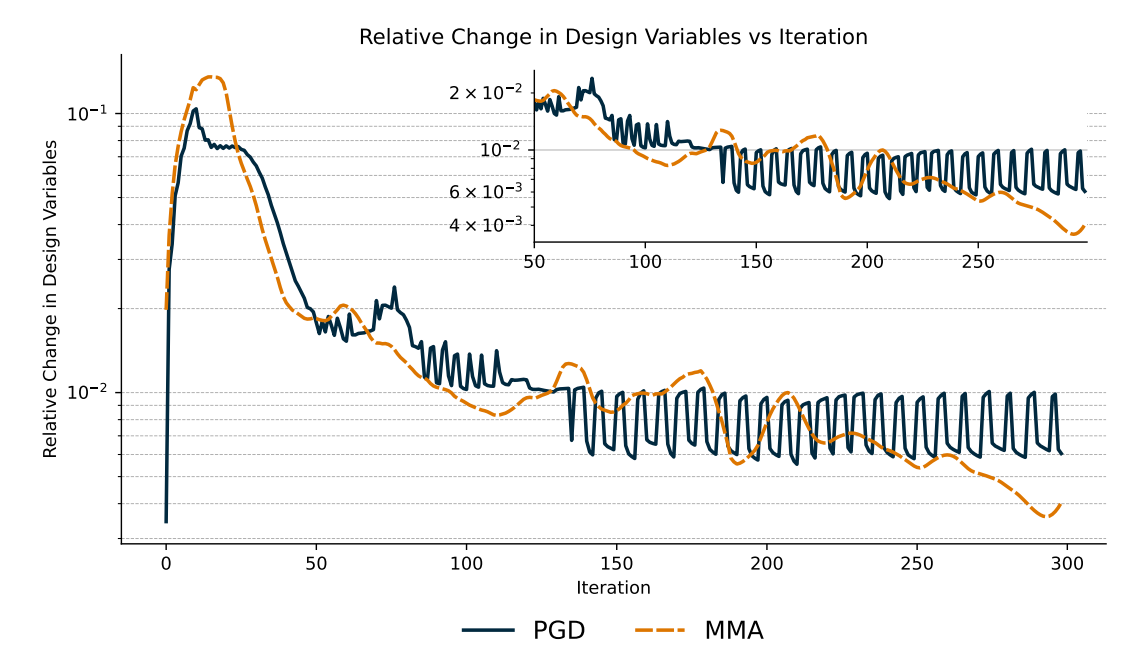


Fig. A24: The value of the relative change in the design variable norm measured at each iteration for all solvers. The plots show a 10-iteration moving average to remove noise and make the plots easier to follow. The inset plot provides a rescaled plot for the same axes after 50 iterations, where solvers have stabilized and the plot is scaled more suitably.

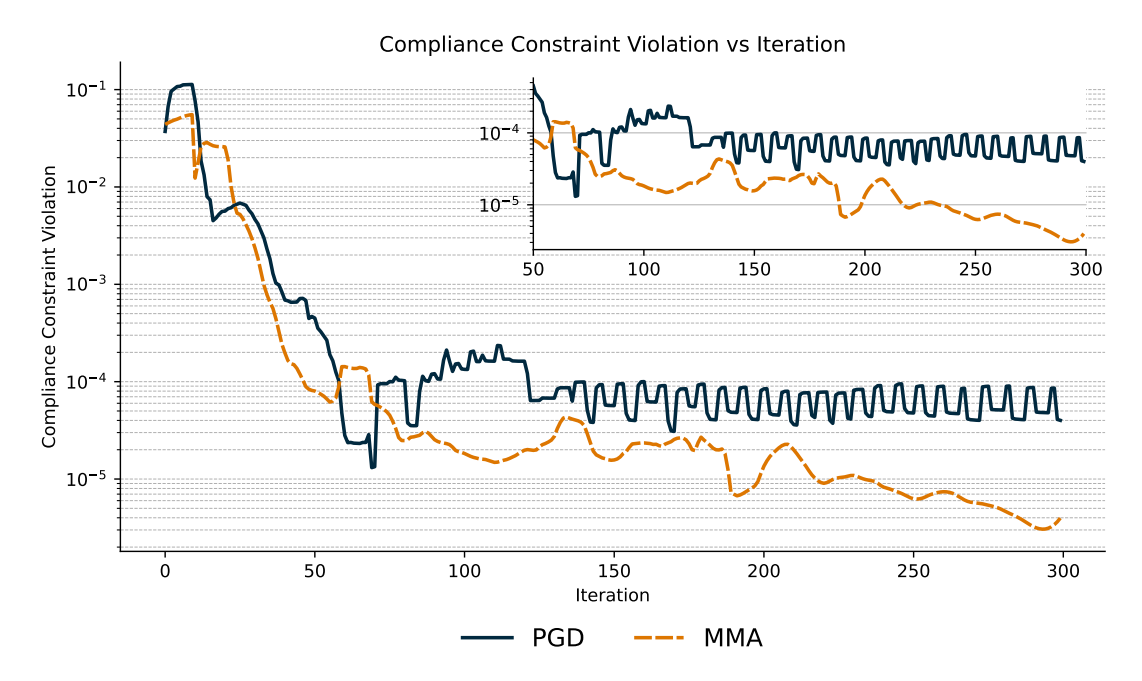


Fig. A25: The value of the constraint violation at each iteration for all solvers. The plots show a 10-iteration moving average to remove noise and make the plots easier to follow. The inset plot provides a rescaled plot for the same axes after 50 iterations, where solvers have stabilized and the plot is scaled more suitably.

Fine Mesh Results

Here we provide figures for the results of running each optimizer for the coarse 512×256 mesh.

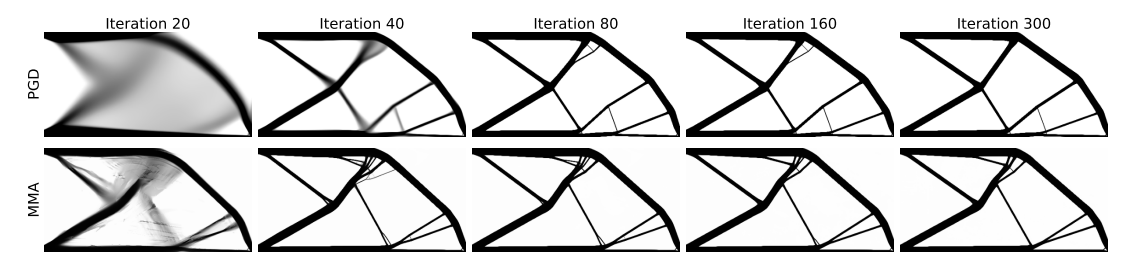


Fig. A26: The designs each optimizer produces at five log-spaced iterations. Here, we visualize the solutions each optimizer produces for the compliance-constrained minimum volume problem on the cantilever beam problem with a volume fraction target of 0.2.

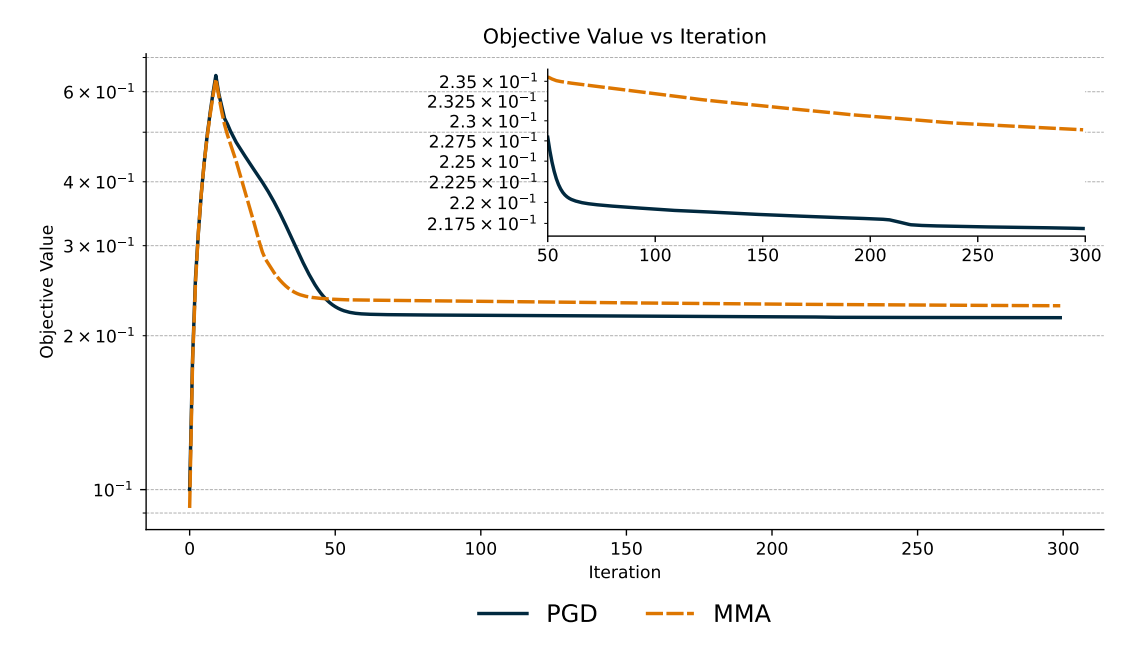


Fig. A27: The value of the objective function measured at each iteration for all solvers. The plots show a 10-iteration moving average to remove noise and make the plots easier to follow. The inset plot provides a rescaled plot for the same axes after 50 iterations, where solvers have stabilized and the plot is scaled more suitably.

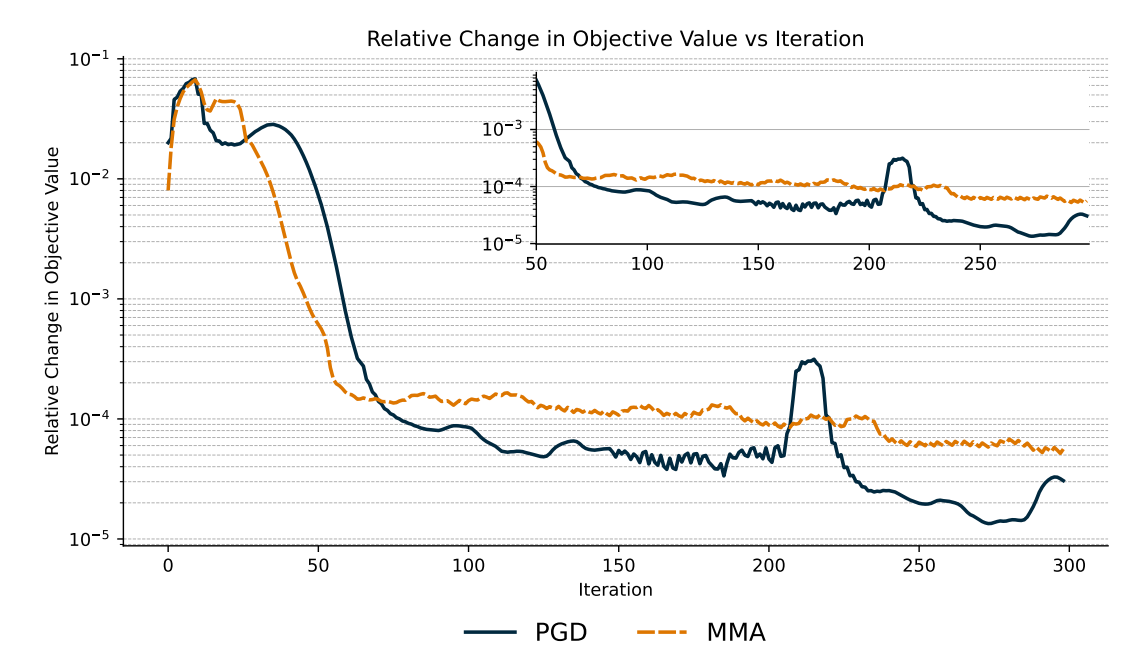


Fig. A28: The value of the relative change in the objective function measured at each iteration for all solvers. The plots show a 10-iteration moving average to remove noise and make the plots easier to follow. The inset plot provides a rescaled plot for the same axes after 50 iterations, where solvers have stabilized and the plot is scaled more suitably.

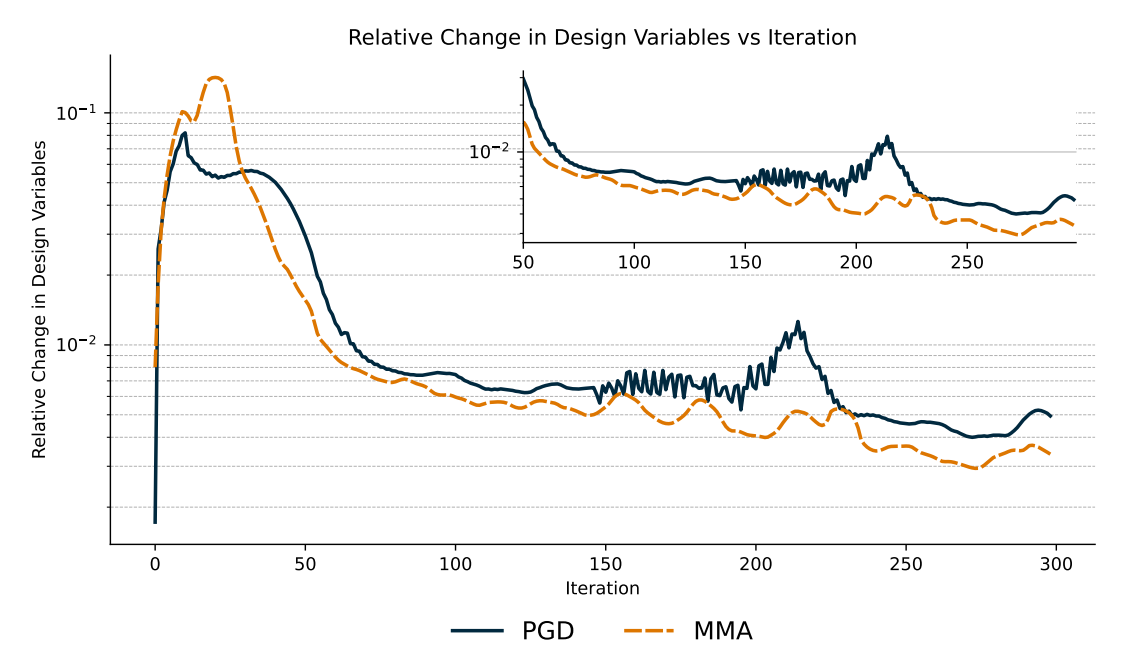


Fig. A29: The value of the relative change in the design variable norm measured at each iteration for all solvers. The plots show a 10-iteration moving average to remove noise and make the plots easier to follow. The inset plot provides a rescaled plot for the same axes after 50 iterations, where solvers have stabilized and the plot is scaled more suitably.

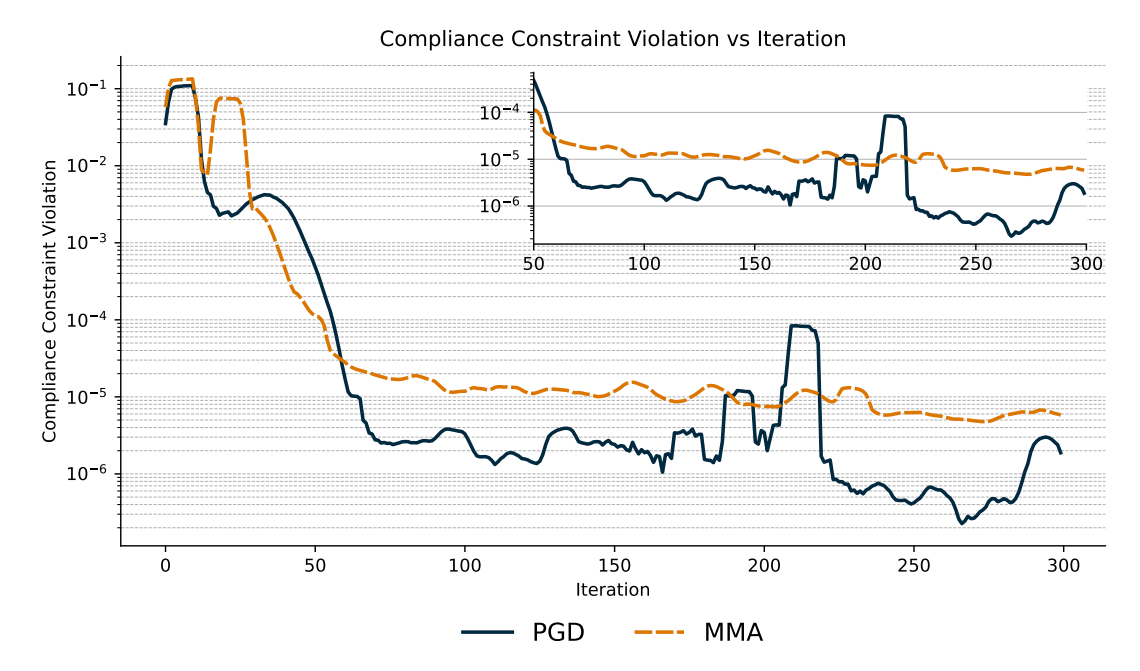


Fig. A30: The value of the constraint violation at each iteration for all solvers. The plots show a 10-iteration moving average to remove noise and make the plots easier to follow. The inset plot provides a rescaled plot for the same axes after 50 iterations, where solvers have stabilized and the plot is scaled more suitably.

A.5.3 Multi-Material Minimum Compliance

Here we provide the full set of results for each of the resolutions. For each resolution, we provide results in the sections that follow.

Coarse Mesh Results

Here we provide figures for the results of running each optimizer for the coarse 128×64 mesh.

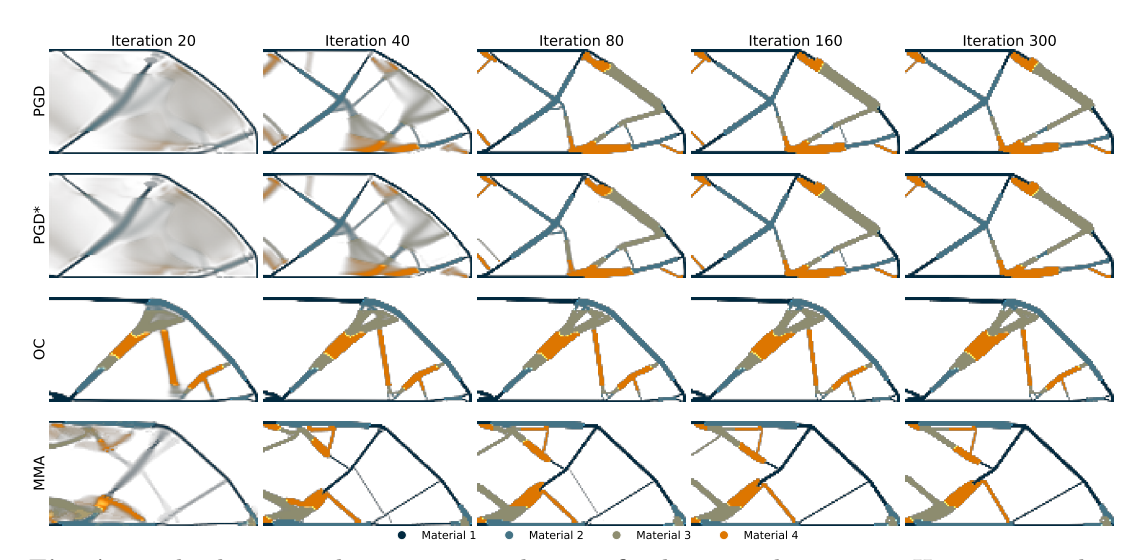


Fig. A31: The designs each optimizer produces at five log-spaced iterations. Here, we visualize the solutions each optimizer produces for the multi-material minimum compliance problem on the cantilever beam problem with a volume fraction target of 0.2.

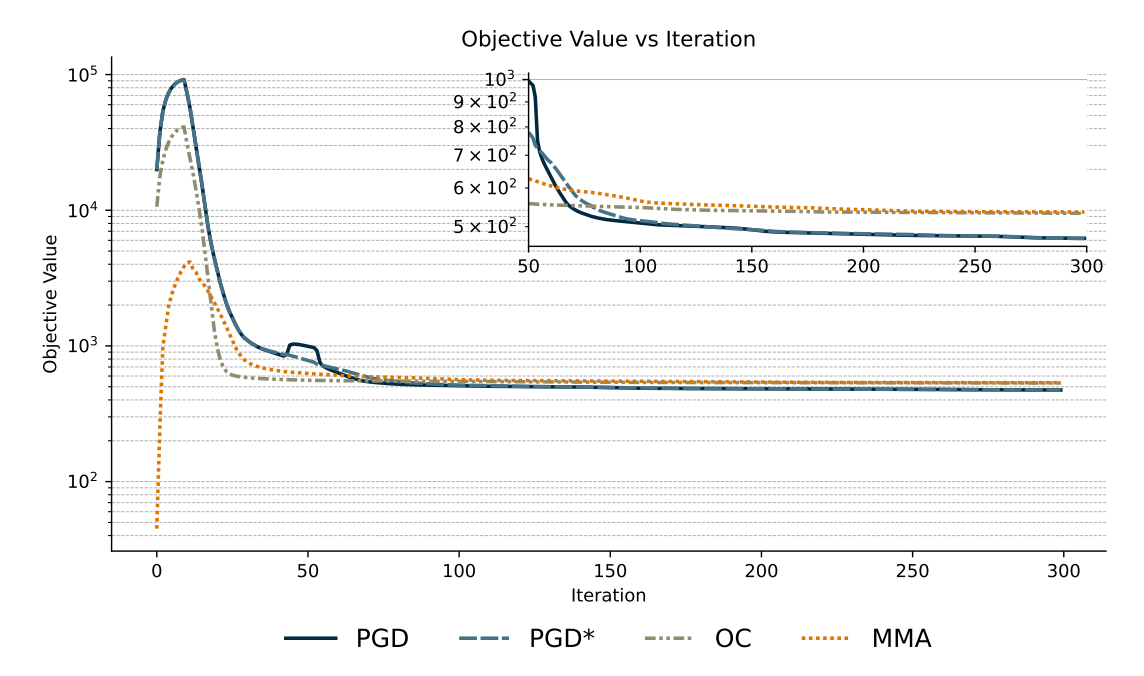


Fig. A32: The value of the objective function measured at each iteration for all solvers. The plots show a 10-iteration moving average to remove noise and make the plots easier to follow. The inset plot provides a rescaled plot for the same axes after 50 iterations, where solvers have stabilized and the plot is scaled more suitably.

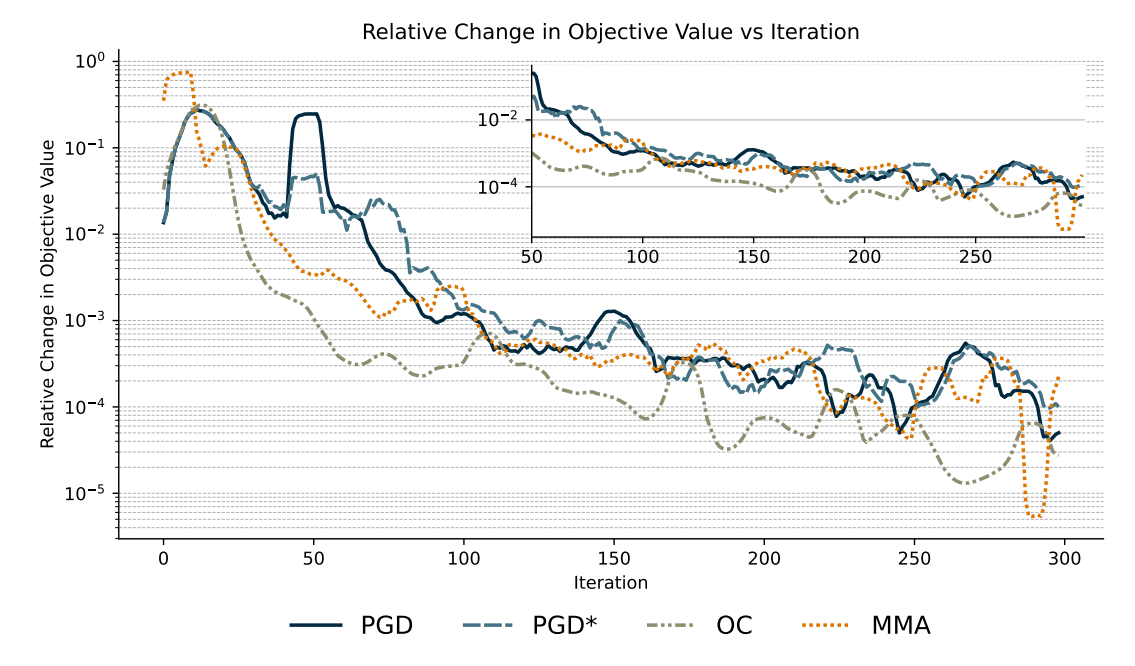


Fig. A33: The value of the relative change in the objective function measured at each iteration for all solvers. The plots show a 10-iteration moving average to remove noise and make the plots easier to follow. The inset plot provides a rescaled plot for the same axes after 50 iterations, where solvers have stabilized and the plot is scaled more suitably.

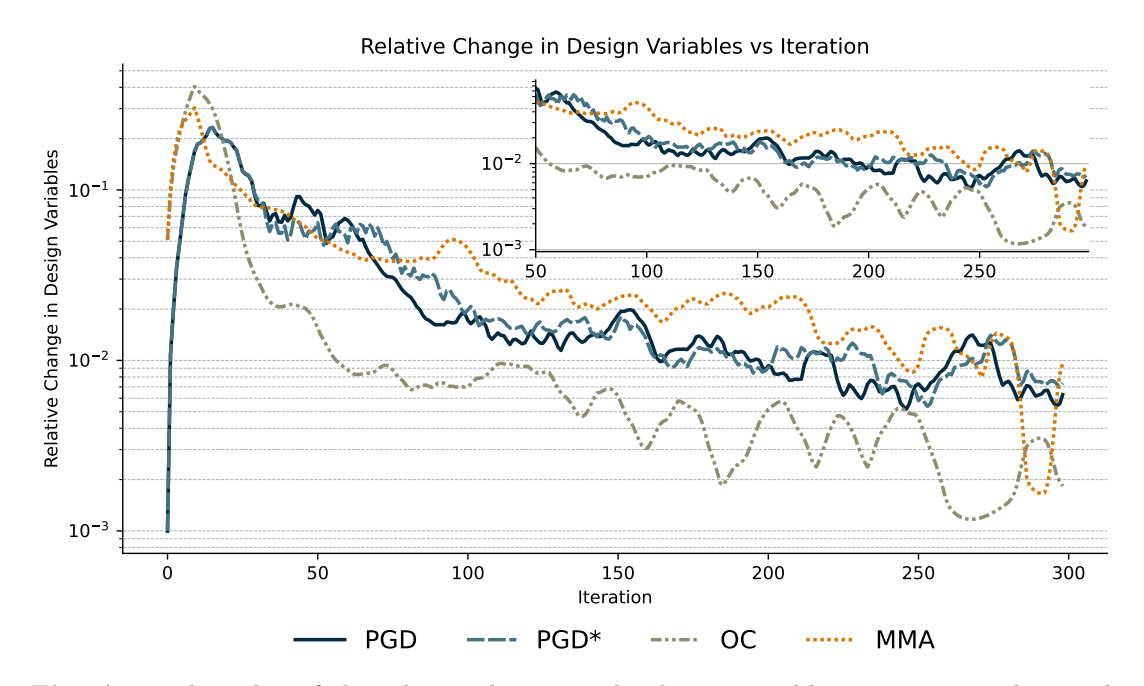


Fig. A34: The value of the relative change in the design variable norm measured at each iteration for all solvers. The plots show a 10-iteration moving average to remove noise and make the plots easier to follow. The inset plot provides a rescaled plot for the same axes after 50 iterations, where solvers have stabilized and the plot is scaled more suitably.

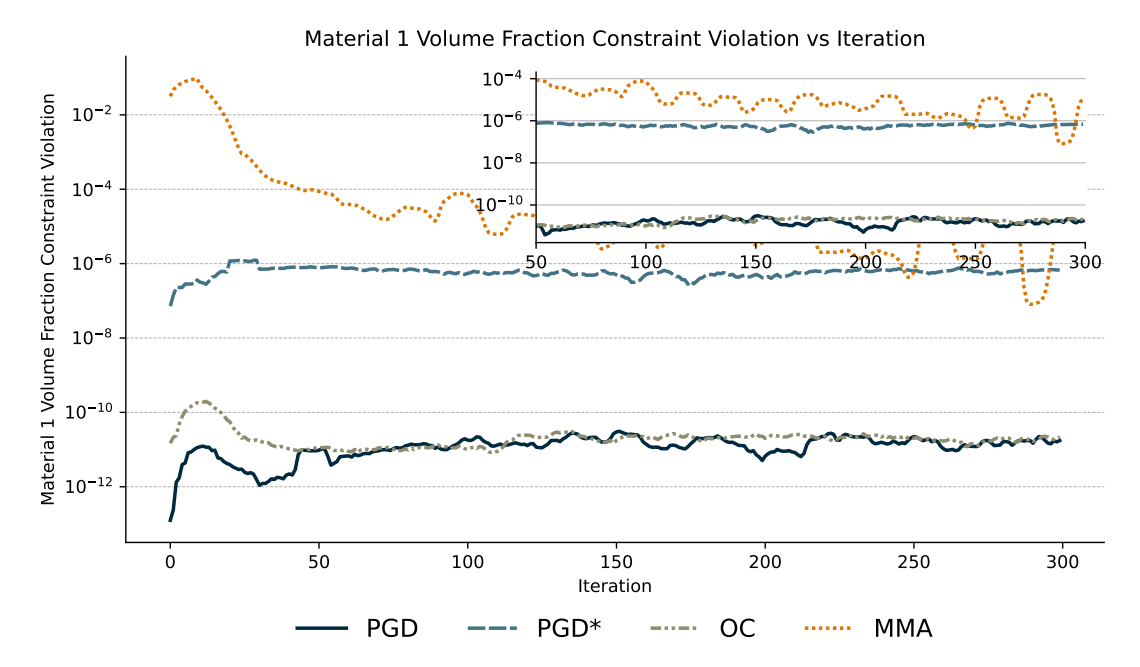


Fig. A35: The value of the constraint violation (material 1) at each iteration for all solvers. The plots show a 10-iteration moving average to remove noise and make the plots easier to follow. The inset plot provides a rescaled plot for the same axes after 50 iterations, where solvers have stabilized and the plot is scaled more suitably.

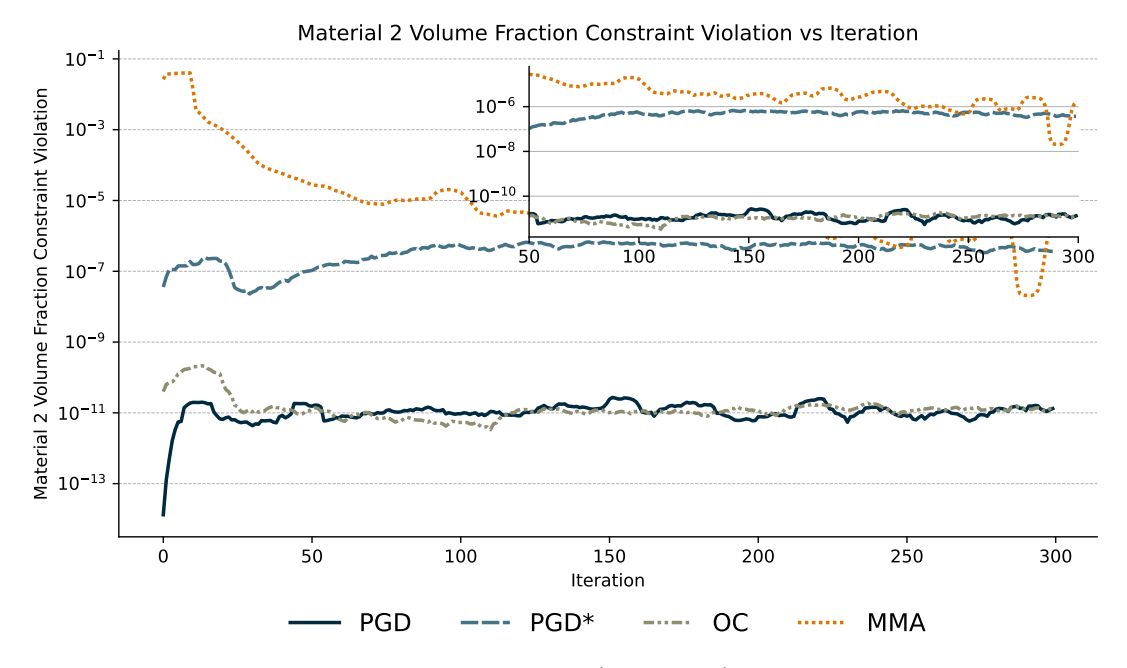


Fig. A36: The value of the constraint violation (material 2) at each iteration for all solvers. The plots show a 10-iteration moving average to remove noise and make the plots easier to follow. The inset plot provides a rescaled plot for the same axes after 50 iterations, where solvers have stabilized and the plot is scaled more suitably.

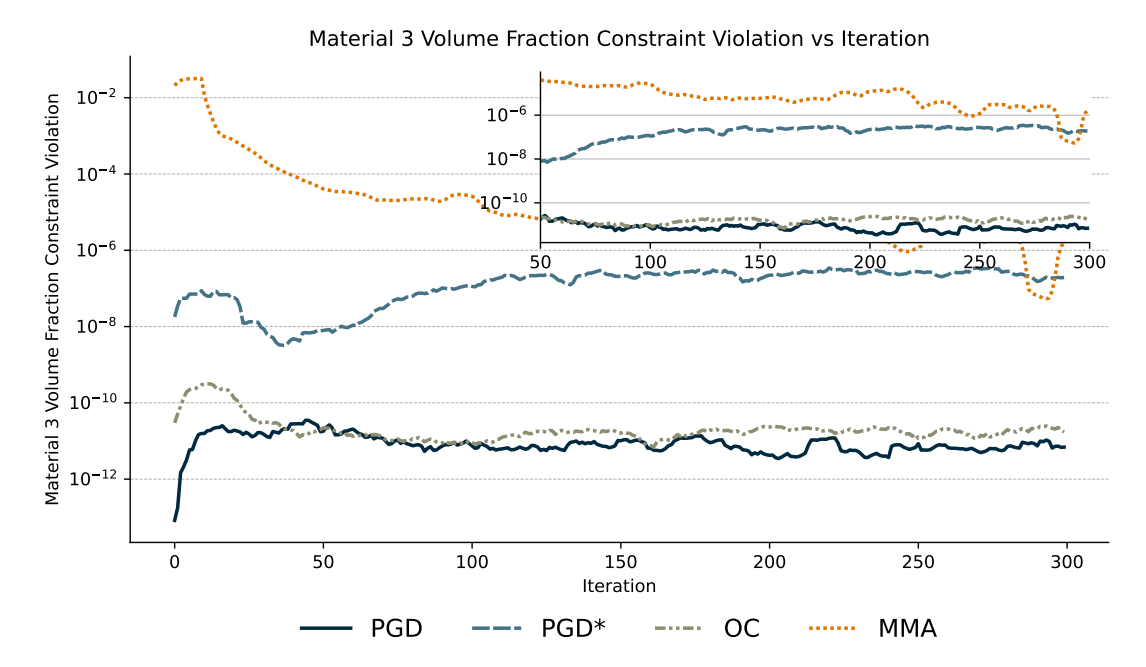


Fig. A37: The value of the constraint violation (material 3) at each iteration for all solvers. The plots show a 10-iteration moving average to remove noise and make the plots easier to follow. The inset plot provides a rescaled plot for the same axes after 50 iterations, where solvers have stabilized and the plot is scaled more suitably.

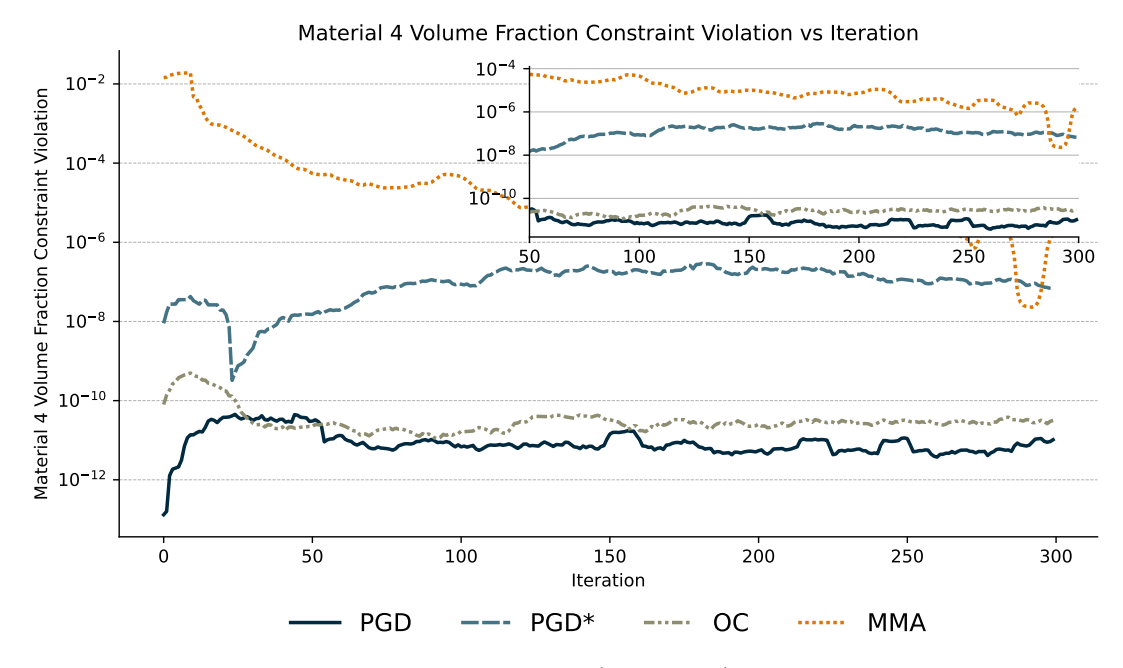


Fig. A38: The value of the constraint violation (material 4) at each iteration for all solvers. The plots show a 10-iteration moving average to remove noise and make the plots easier to follow. The inset plot provides a rescaled plot for the same axes after 50 iterations, where solvers have stabilized and the plot is scaled more suitably.

Medium Mesh Results

Here we provide figures for the results of running each optimizer for the coarse 256×128 mesh.

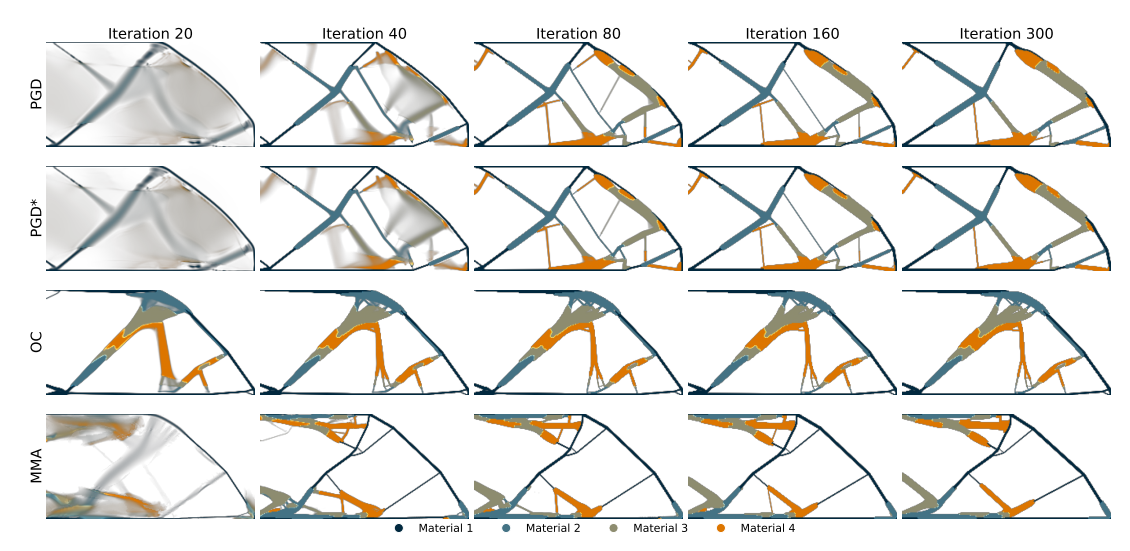


Fig. A39: The designs each optimizer produces at five log-spaced iterations. Here, we visualize the solutions each optimizer produces for the multi-material minimum compliance problem on the cantilever beam problem with a volume fraction target of 0.2.

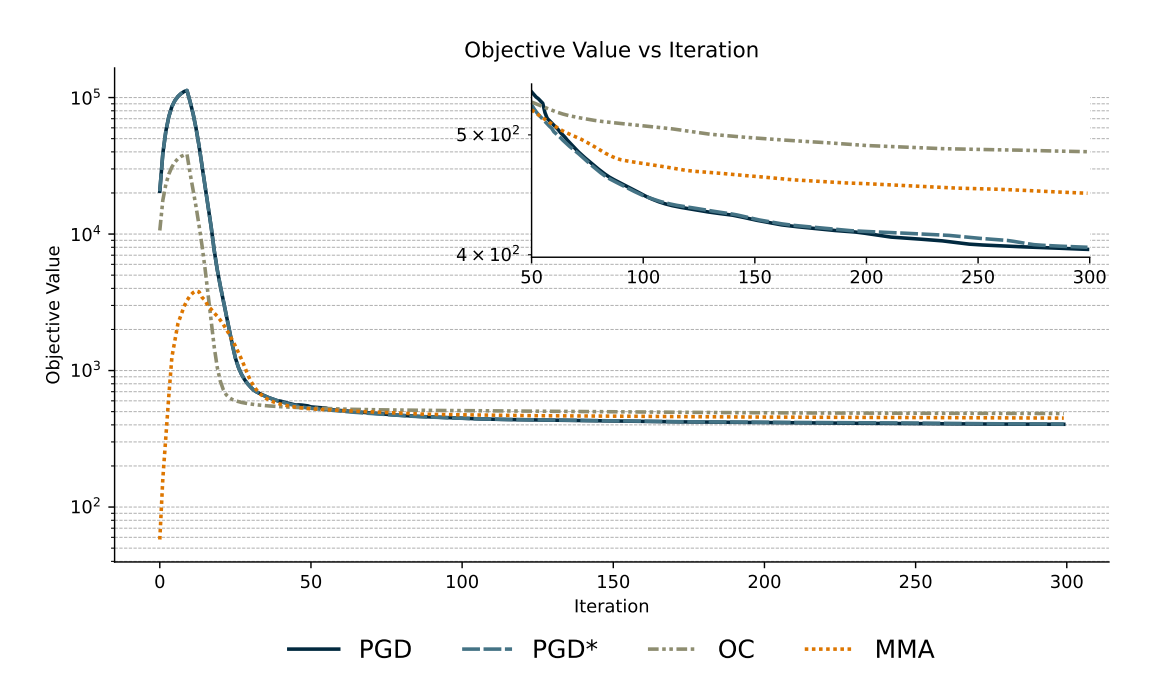


Fig. A40: The value of the objective function measured at each iteration for all solvers. The plots show a 10-iteration moving average to remove noise and make the plots easier to follow. The inset plot provides a rescaled plot for the same axes after 50 iterations, where solvers have stabilized and the plot is scaled more suitably.

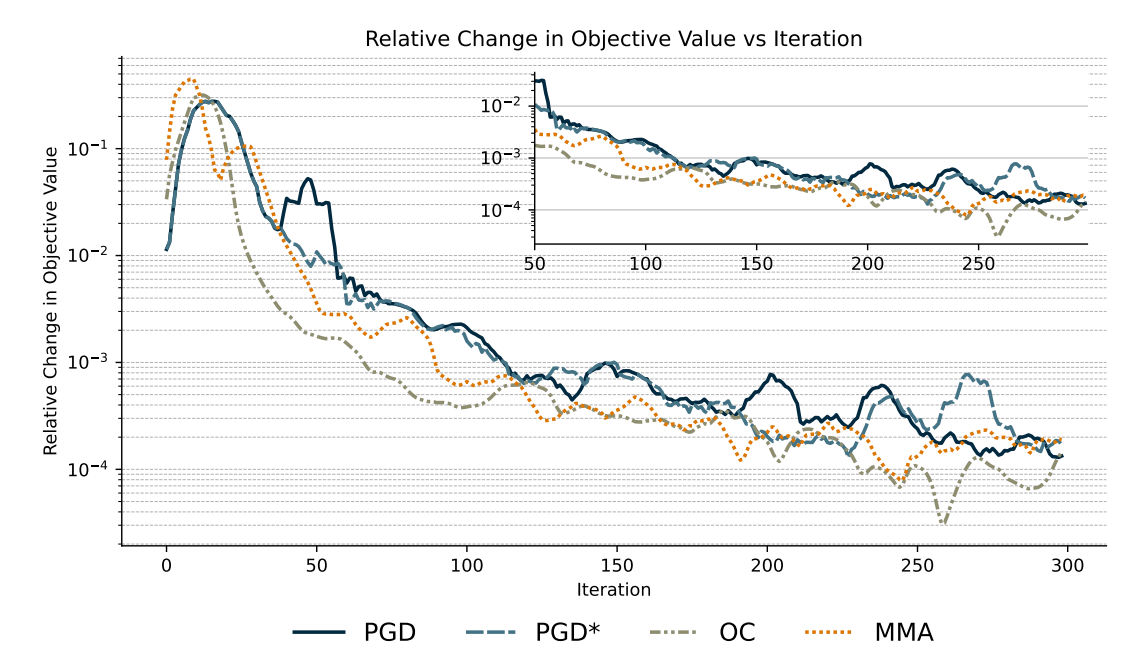


Fig. A41: The value of the relative change in the objective function measured at each iteration for all solvers. The plots show a 10-iteration moving average to remove noise and make the plots easier to follow. The inset plot provides a rescaled plot for the same axes after 50 iterations, where solvers have stabilized and the plot is scaled more suitably.

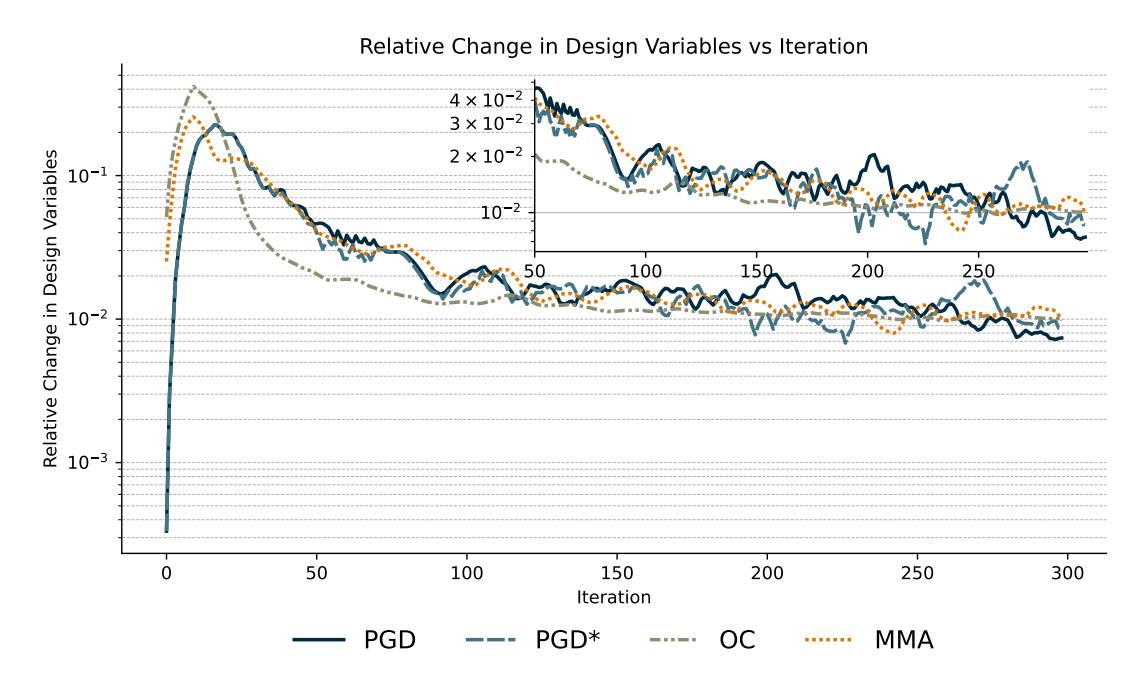


Fig. A42: The value of the relative change in the design variable norm measured at each iteration for all solvers. The plots show a 10-iteration moving average to remove noise and make the plots easier to follow. The inset plot provides a rescaled plot for the same axes after 50 iterations, where solvers have stabilized and the plot is scaled more suitably.

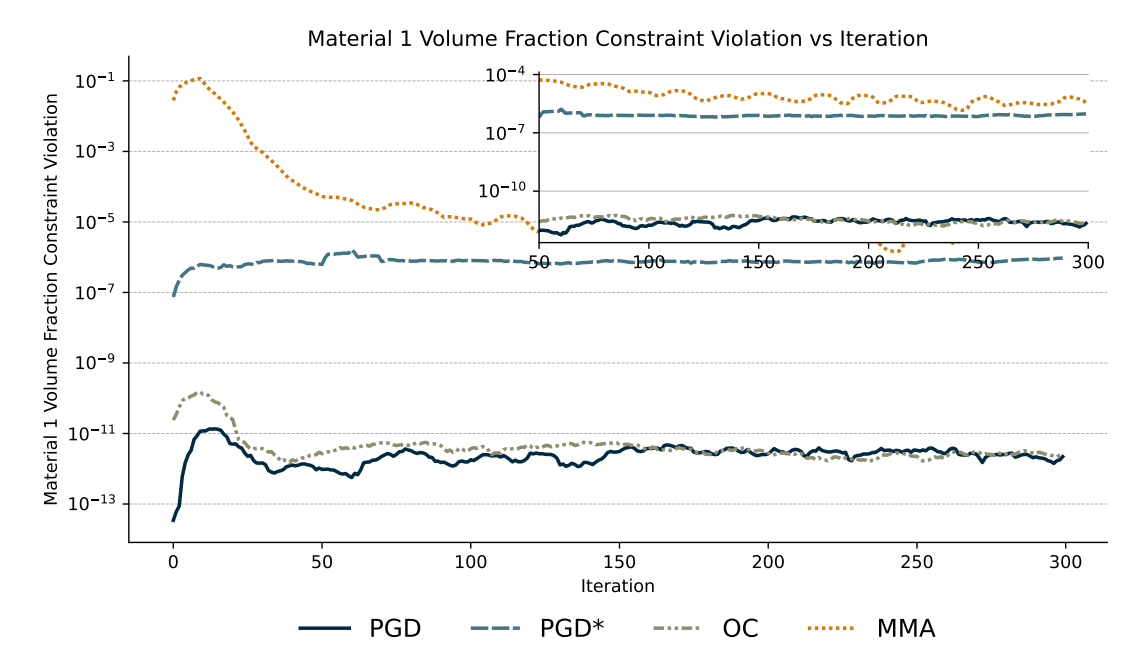


Fig. A43: The value of the constraint violation (material 1) at each iteration for all solvers. The plots show a 10-iteration moving average to remove noise and make the plots easier to follow. The inset plot provides a rescaled plot for the same axes after 50 iterations, where solvers have stabilized and the plot is scaled more suitably.

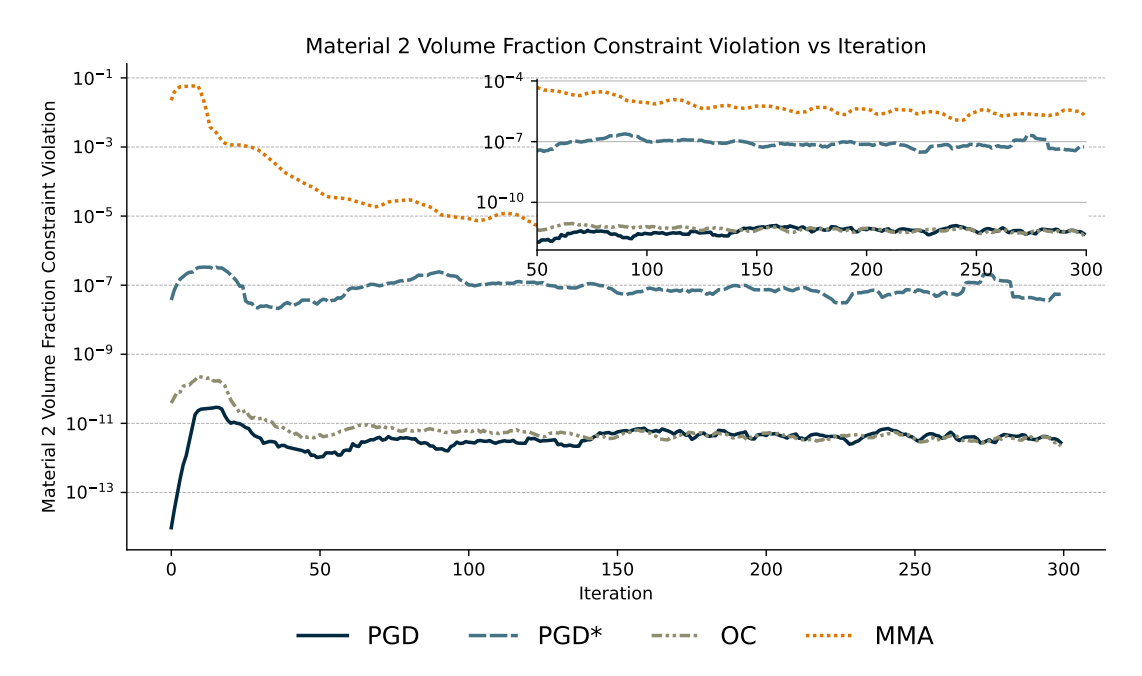


Fig. A44: The value of the constraint violation (material 2) at each iteration for all solvers. The plots show a 10-iteration moving average to remove noise and make the plots easier to follow. The inset plot provides a rescaled plot for the same axes after 50 iterations, where solvers have stabilized and the plot is scaled more suitably.

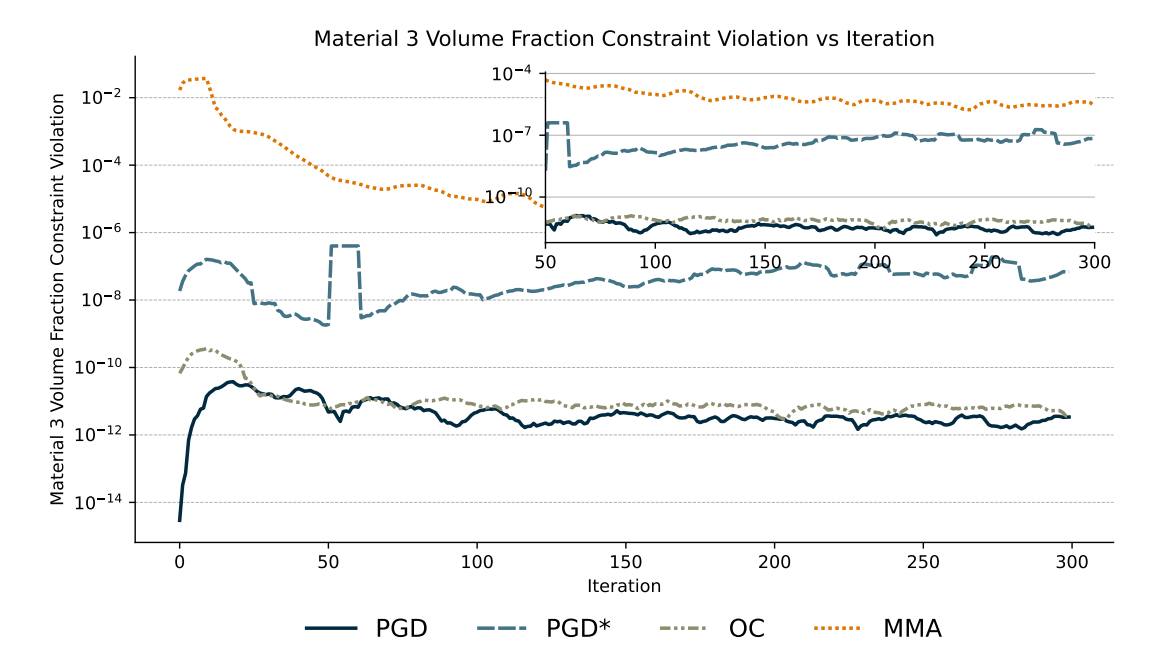


Fig. A45: The value of the constraint violation (material 3) at each iteration for all solvers. The plots show a 10-iteration moving average to remove noise and make the plots easier to follow. The inset plot provides a rescaled plot for the same axes after 50 iterations, where solvers have stabilized and the plot is scaled more suitably.

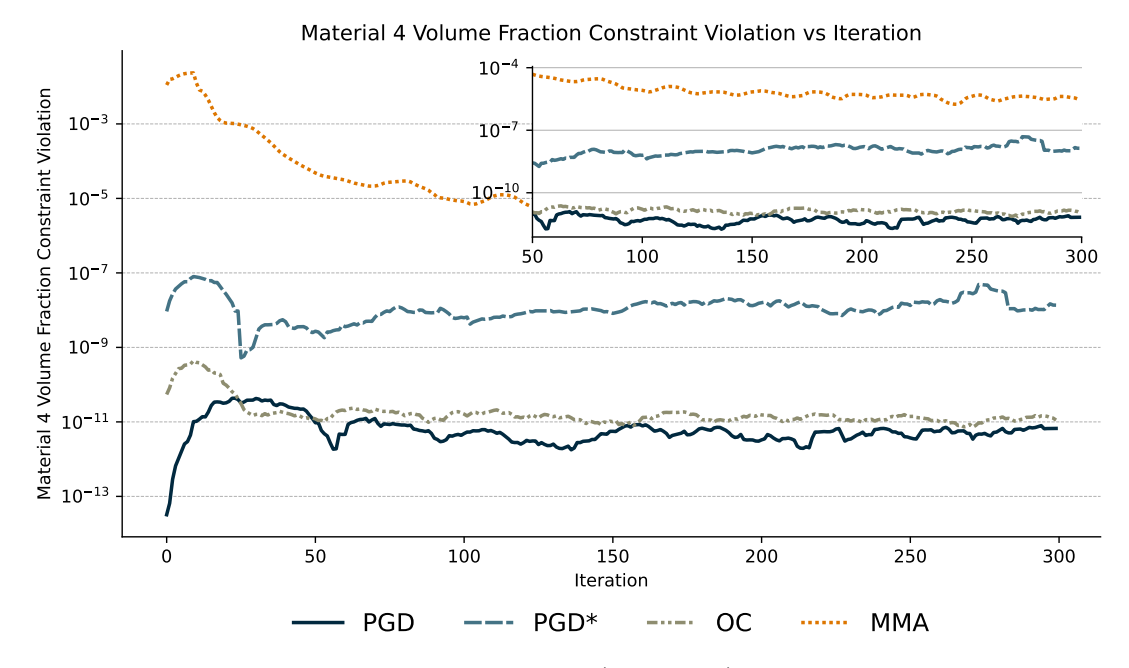


Fig. A46: The value of the constraint violation (material 4) at each iteration for all solvers. The plots show a 10-iteration moving average to remove noise and make the plots easier to follow. The inset plot provides a rescaled plot for the same axes after 50 iterations, where solvers have stabilized and the plot is scaled more suitably.

Fine Mesh Results

Here we provide figures for the results of running each optimizer for the coarse 512×256 mesh.

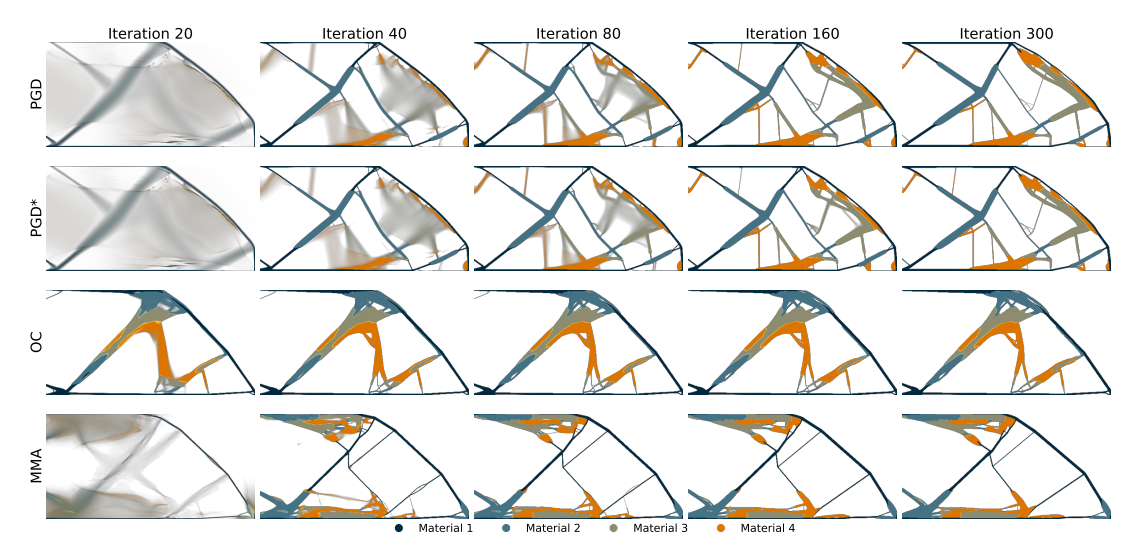


Fig. A47: The designs each optimizer produces at five log-spaced iterations. Here, we visualize the solutions each optimizer produces for the multi-material minimum compliance problem on the cantilever beam problem with a volume fraction target of 0.2.

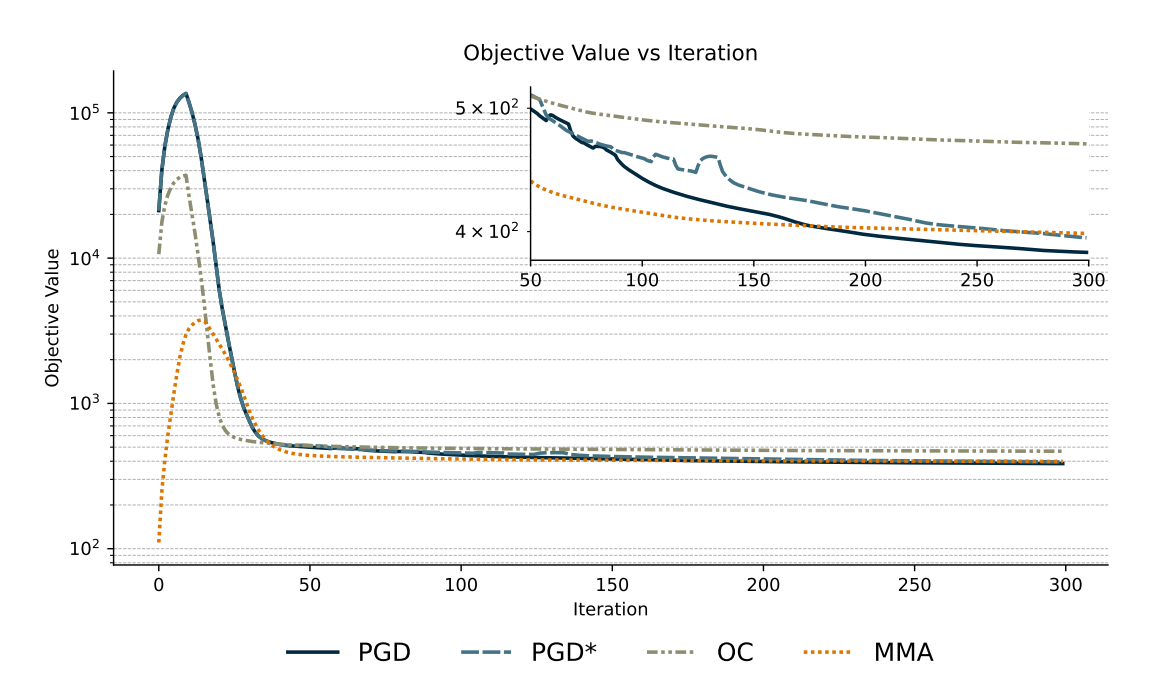


Fig. A48: The value of the objective function measured at each iteration for all solvers. The plots show a 10-iteration moving average to remove noise and make the plots easier to follow. The inset plot provides a rescaled plot for the same axes after 50 iterations, where solvers have stabilized and the plot is scaled more suitably.

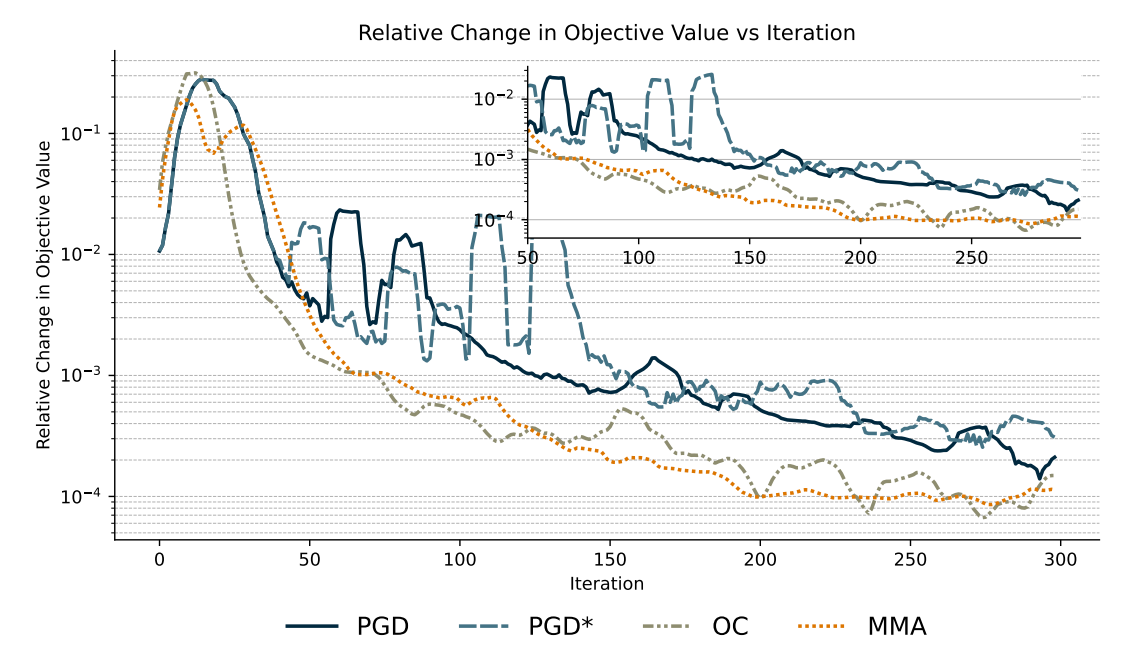


Fig. A49: The value of the relative change in the objective function measured at each iteration for all solvers. The plots show a 10-iteration moving average to remove noise and make the plots easier to follow. The inset plot provides a rescaled plot for the same axes after 50 iterations, where solvers have stabilized and the plot is scaled more suitably.

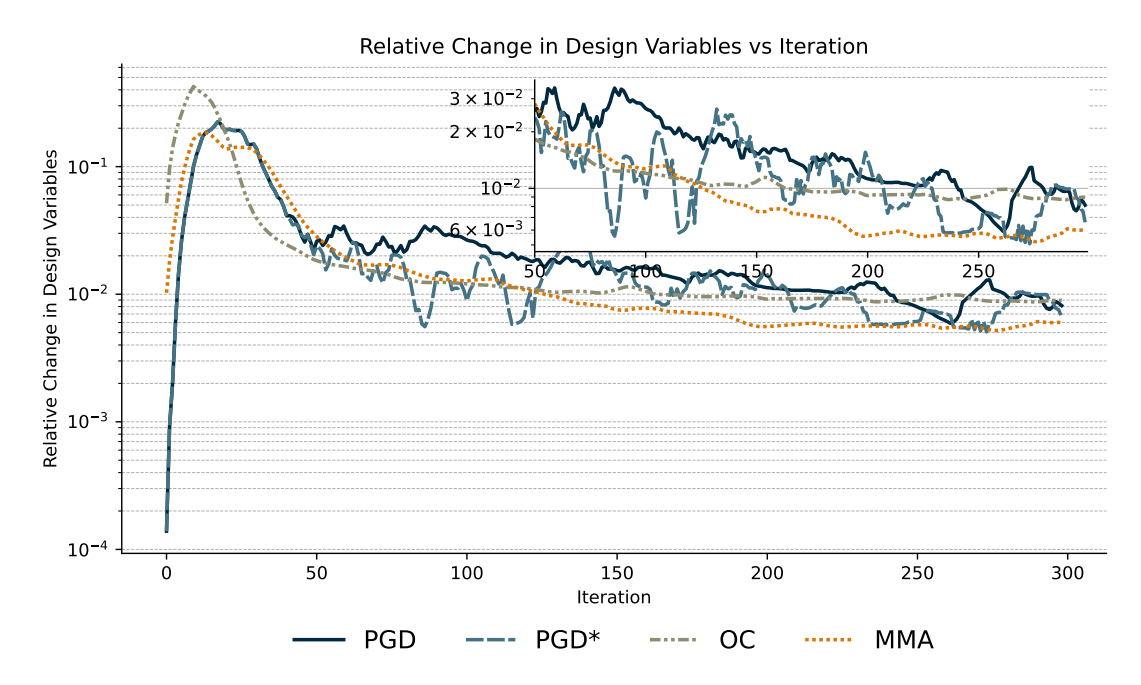


Fig. A50: The value of the relative change in the design variable norm measured at each iteration for all solvers. The plots show a 10-iteration moving average to remove noise and make the plots easier to follow. The inset plot provides a rescaled plot for the same axes after 50 iterations, where solvers have stabilized and the plot is scaled more suitably.

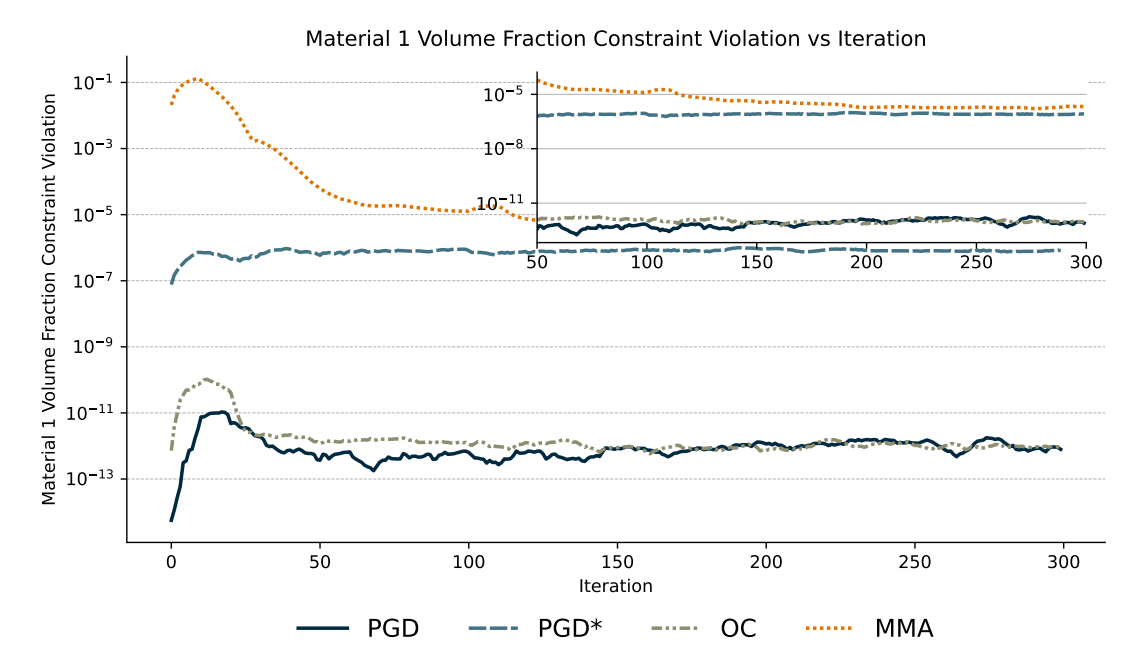


Fig. A51: The value of the constraint violation (material 1) at each iteration for all solvers. The plots show a 10-iteration moving average to remove noise and make the plots easier to follow. The inset plot provides a rescaled plot for the same axes after 50 iterations, where solvers have stabilized and the plot is scaled more suitably.

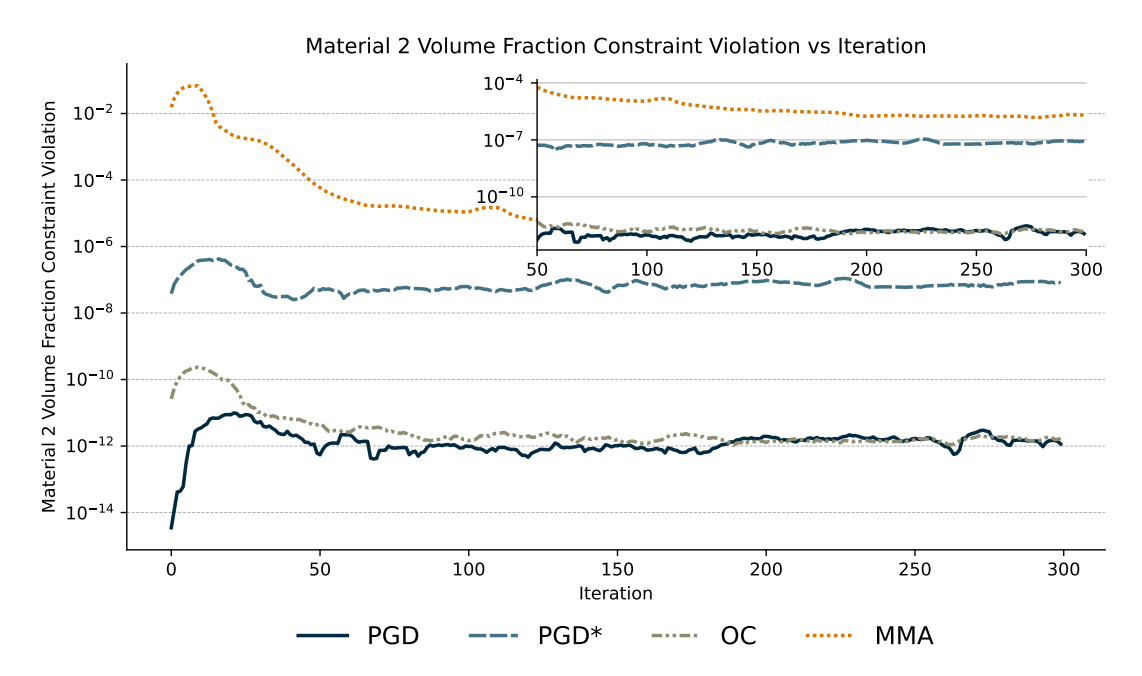


Fig. A52: The value of the constraint violation (material 2) at each iteration for all solvers. The plots show a 10-iteration moving average to remove noise and make the plots easier to follow. The inset plot provides a rescaled plot for the same axes after 50 iterations, where solvers have stabilized and the plot is scaled more suitably.

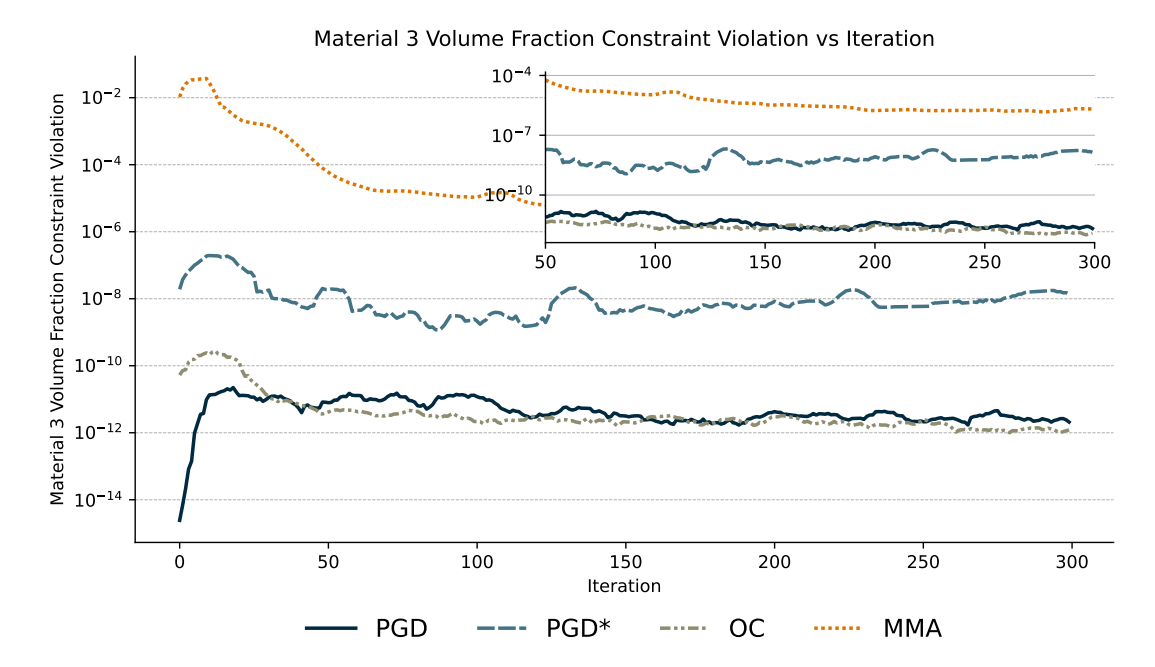


Fig. A53: The value of the constraint violation (material 3) at each iteration for all solvers. The plots show a 10-iteration moving average to remove noise and make the plots easier to follow. The inset plot provides a rescaled plot for the same axes after 50 iterations, where solvers have stabilized and the plot is scaled more suitably.

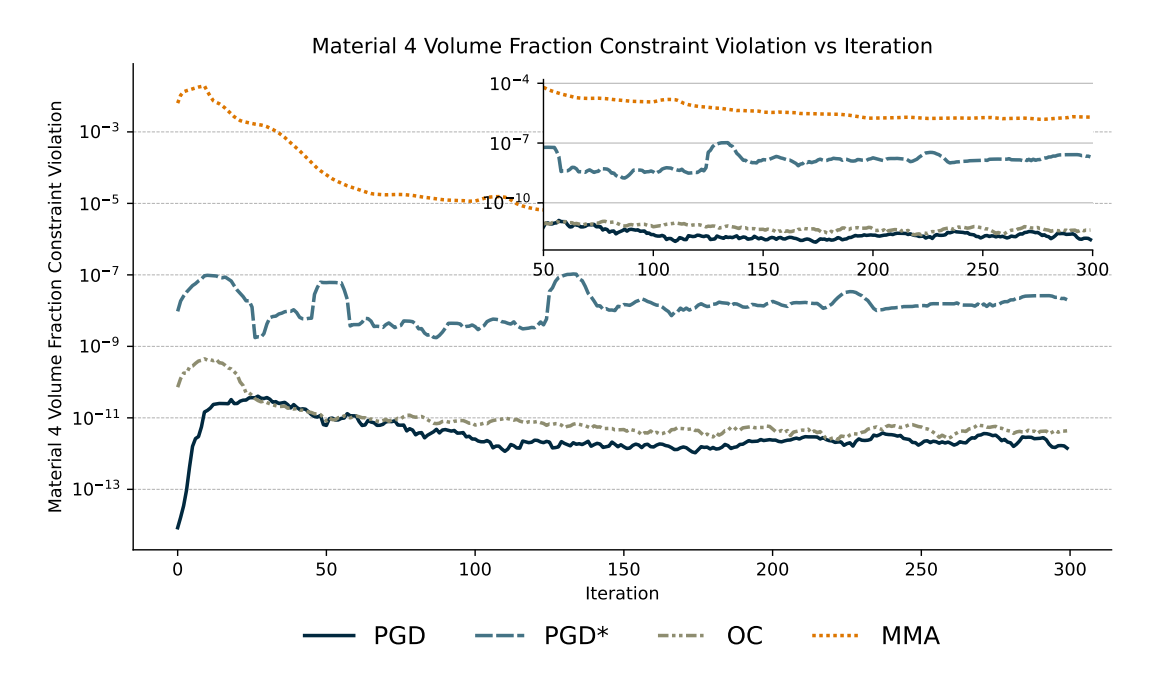


Fig. A54: The value of the constraint violation (material 4) at each iteration for all solvers. The plots show a 10-iteration moving average to remove noise and make the plots easier to follow. The inset plot provides a rescaled plot for the same axes after 50 iterations, where solvers have stabilized and the plot is scaled more suitably.

A.5.4 Volume & Weight Distribution Constrained Minimum Compliance

Here we provide the full set of results for each of the resolutions. For each resolution, we provide results in the sections that follow.

Coarse Mesh Results

Here we provide figures for the results of running each optimizer for the coarse 128×64 mesh.

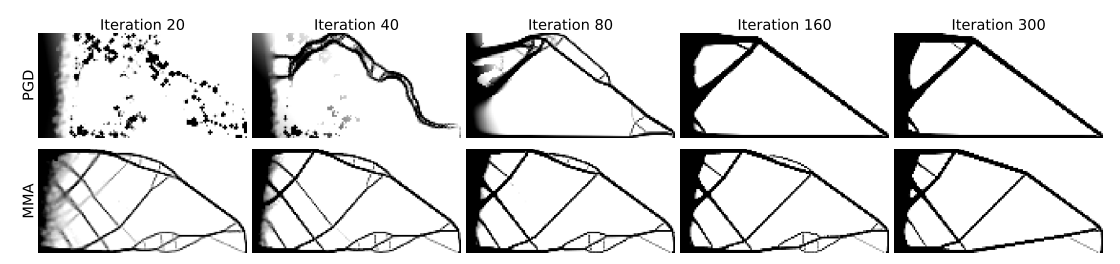


Fig. A55: The designs each optimizer produces at five log-spaced iterations. Here, we visualize the solutions each optimizer produces for the volume & weight constrained minimum compliance problem on the cantilever beam problem with a volume fraction target of 0.2.

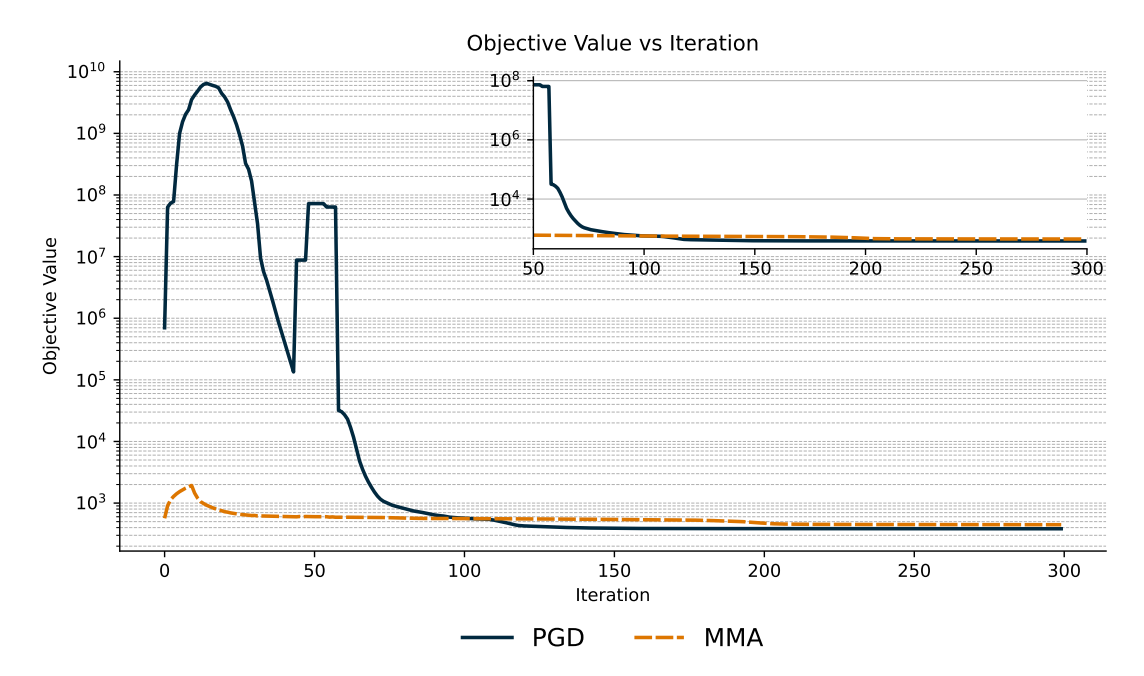


Fig. A56: The value of the objective function measured at each iteration for all solvers. The plots show a 10-iteration moving average to remove noise and make the plots easier to follow. The inset plot provides a rescaled plot for the same axes after 50 iterations, where solvers have stabilized and the plot is scaled more suitably.

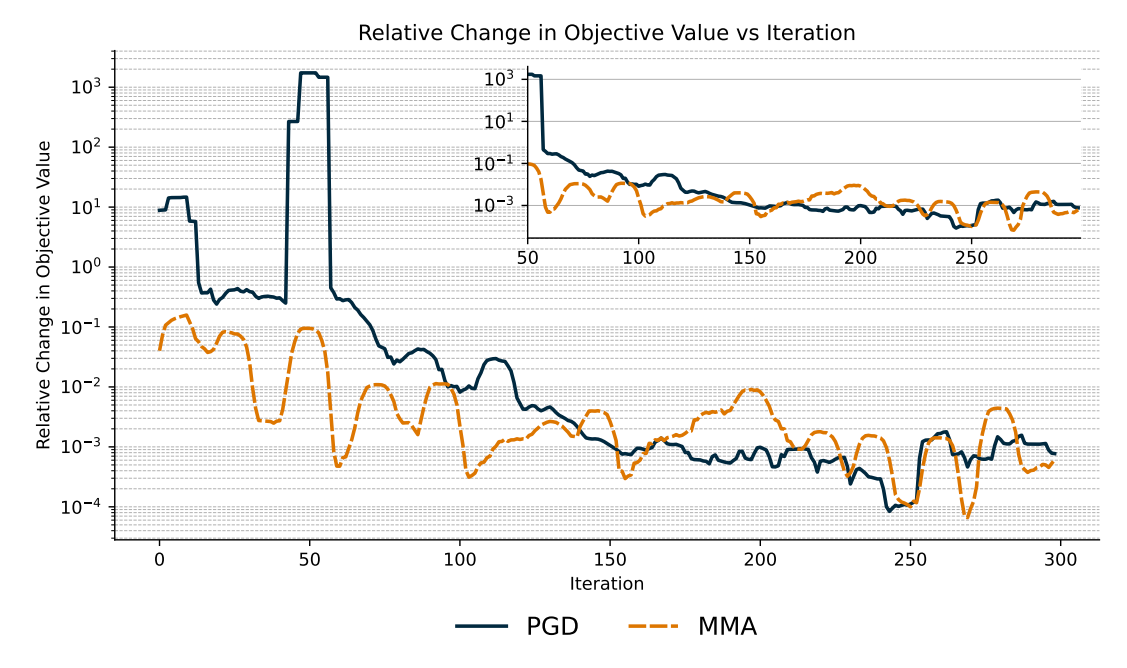


Fig. A57: The value of the relative change in the objective function measured at each iteration for all solvers. The plots show a 10-iteration moving average to remove noise and make the plots easier to follow. The inset plot provides a rescaled plot for the same axes after 50 iterations, where solvers have stabilized and the plot is scaled more suitably.

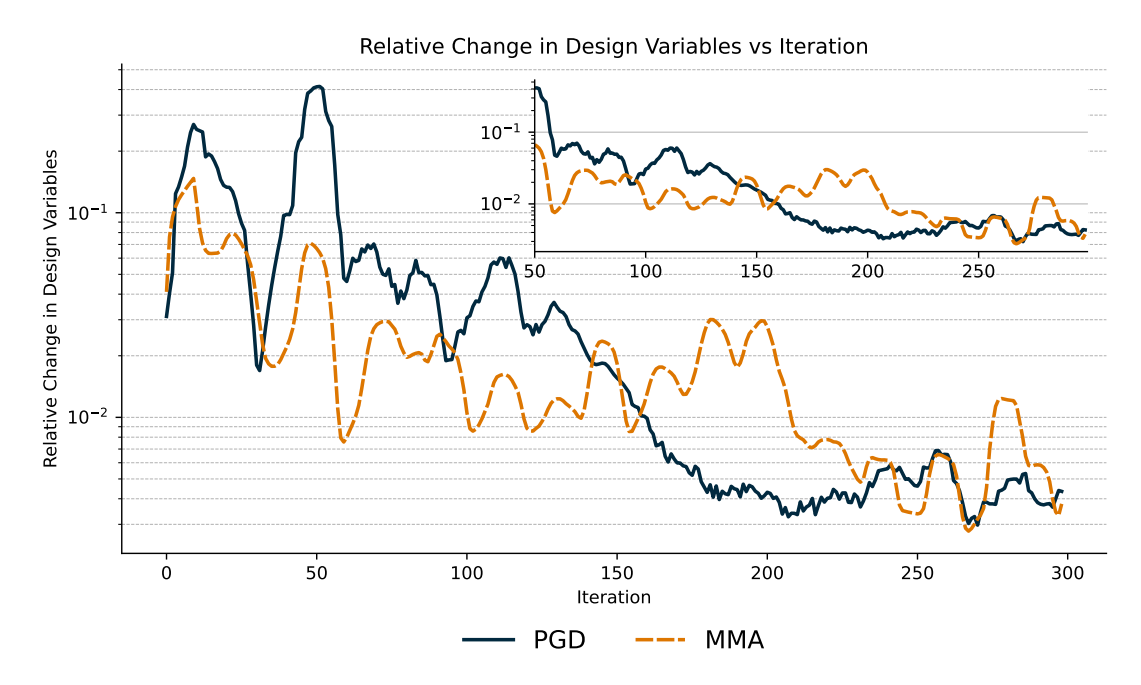


Fig. A58: The value of the relative change in the design variable norm measured at each iteration for all solvers. The plots show a 10-iteration moving average to remove noise and make the plots easier to follow. The inset plot provides a rescaled plot for the same axes after 50 iterations, where solvers have stabilized and the plot is scaled more suitably.

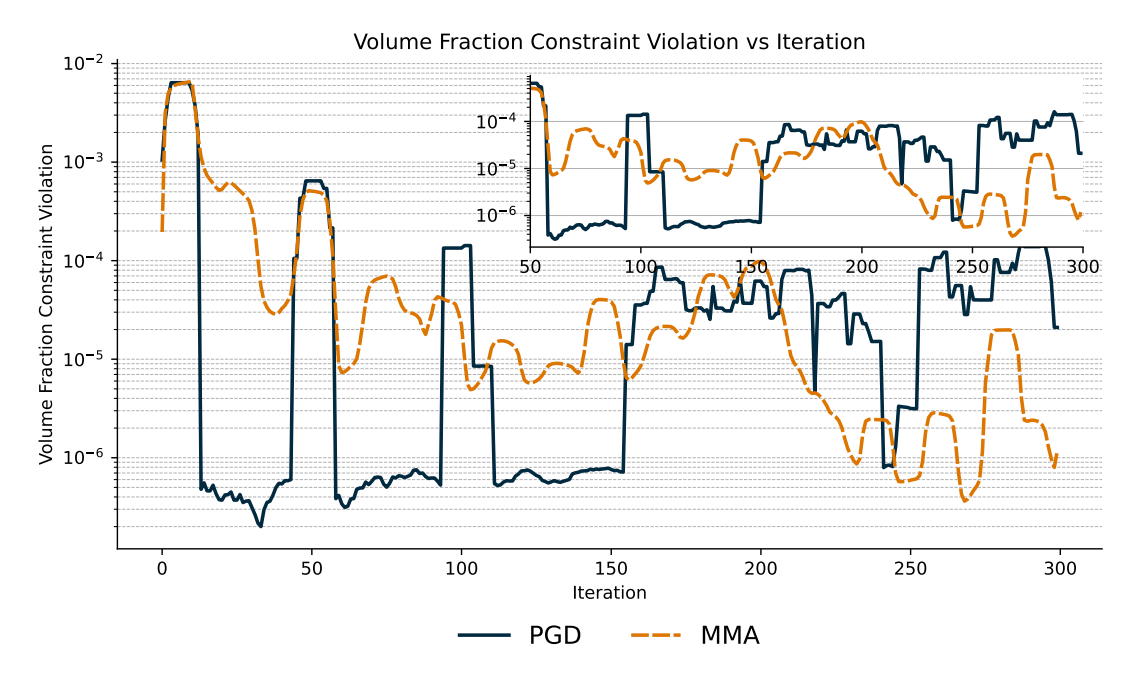


Fig. A59: The value of the constraint violation (volume constraint) at each iteration for all solvers. The plots show a 10-iteration moving average to remove noise and make the plots easier to follow. The inset plot provides a rescaled plot for the same axes after 50 iterations, where solvers have stabilized and the plot is scaled more suitably.

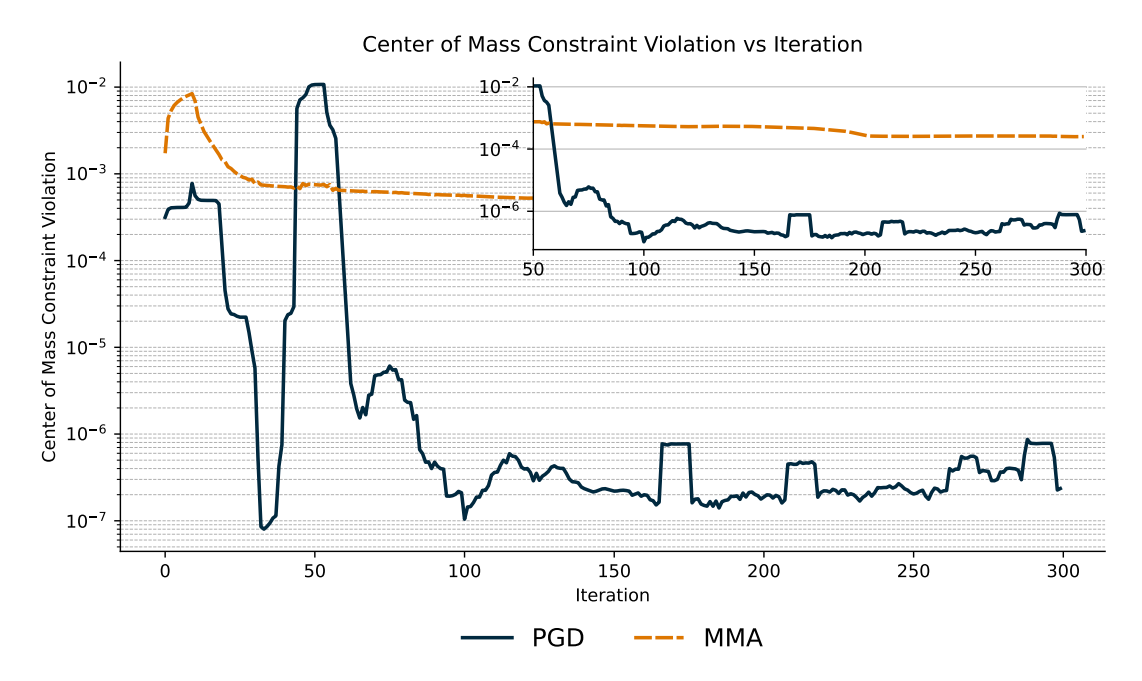


Fig. A60: The value of the constraint violation (center of distance deviation) at each iteration for all solvers. The plots show a 10-iteration moving average to remove noise and make the plots easier to follow. The inset plot provides a rescaled plot for the same axes after 50 iterations, where solvers have stabilized and the plot is scaled more suitably.

Medium Mesh Results

Here we provide figures for the results of running each optimizer for the coarse 256×128 mesh.

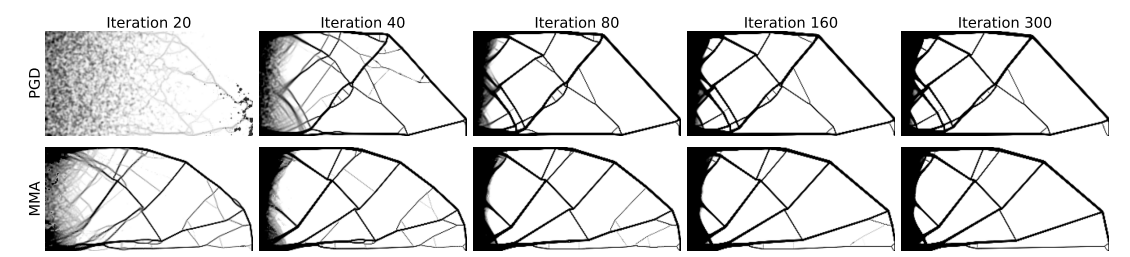


Fig. A61: The designs each optimizer produces at five log-spaced iterations. Here, we visualize the solutions each optimizer produces for the volume & weight constrained minimum compliance problem on the cantilever beam problem with a volume fraction target of 0.2.

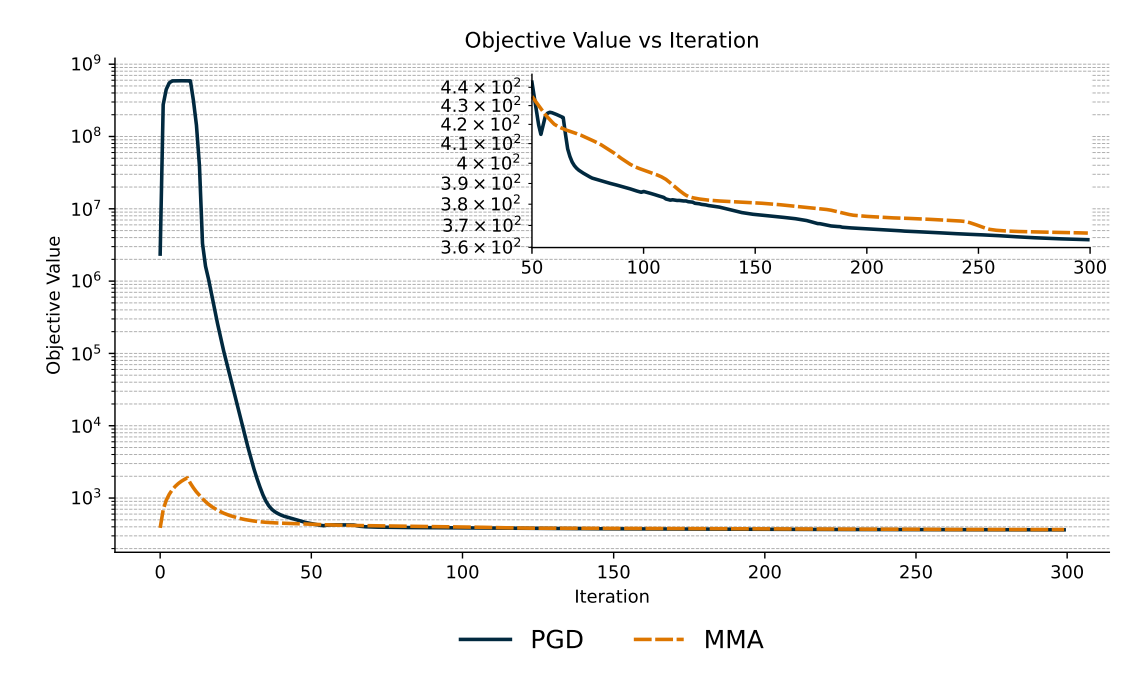


Fig. A62: The value of the objective function measured at each iteration for all solvers. The plots show a 10-iteration moving average to remove noise and make the plots easier to follow. The inset plot provides a rescaled plot for the same axes after 50 iterations, where solvers have stabilized and the plot is scaled more suitably.

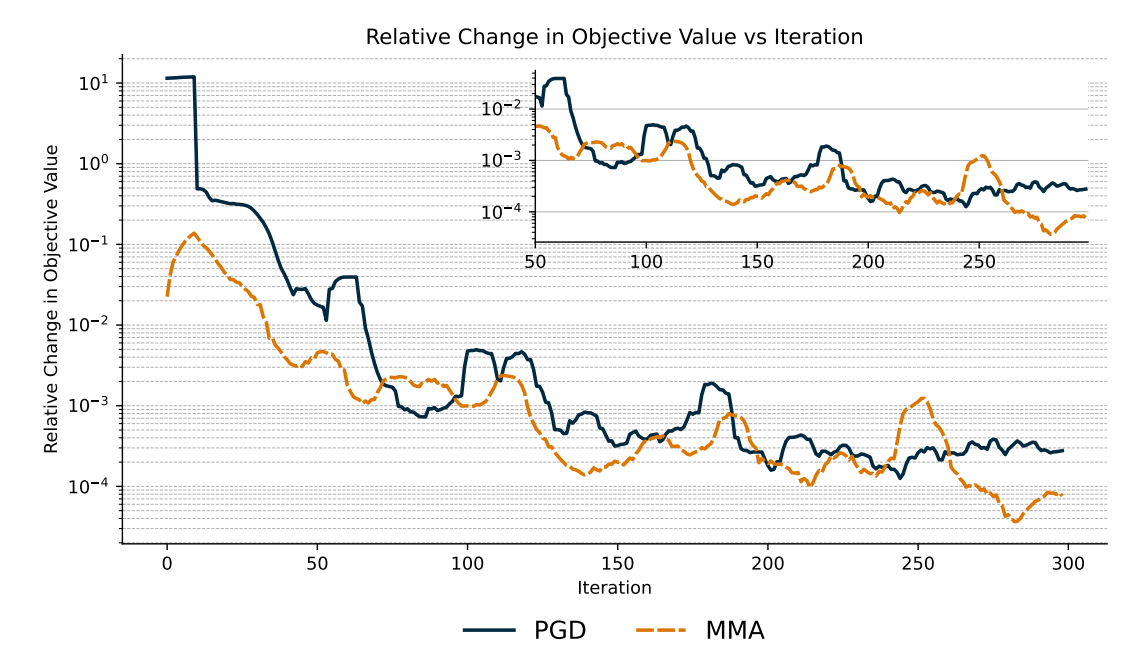


Fig. A63: The value of the relative change in the objective function measured at each iteration for all solvers. The plots show a 10-iteration moving average to remove noise and make the plots easier to follow. The inset plot provides a rescaled plot for the same axes after 50 iterations, where solvers have stabilized and the plot is scaled more suitably.

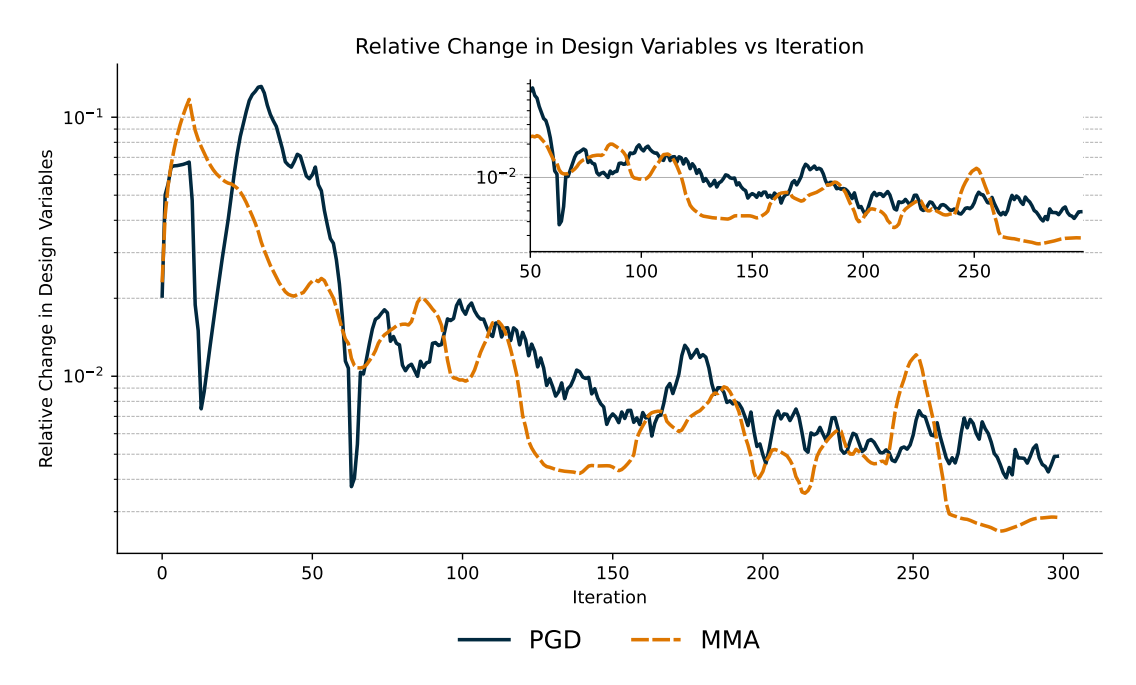


Fig. A64: The value of the relative change in the design variable norm measured at each iteration for all solvers. The plots show a 10-iteration moving average to remove noise and make the plots easier to follow. The inset plot provides a rescaled plot for the same axes after 50 iterations, where solvers have stabilized and the plot is scaled more suitably.

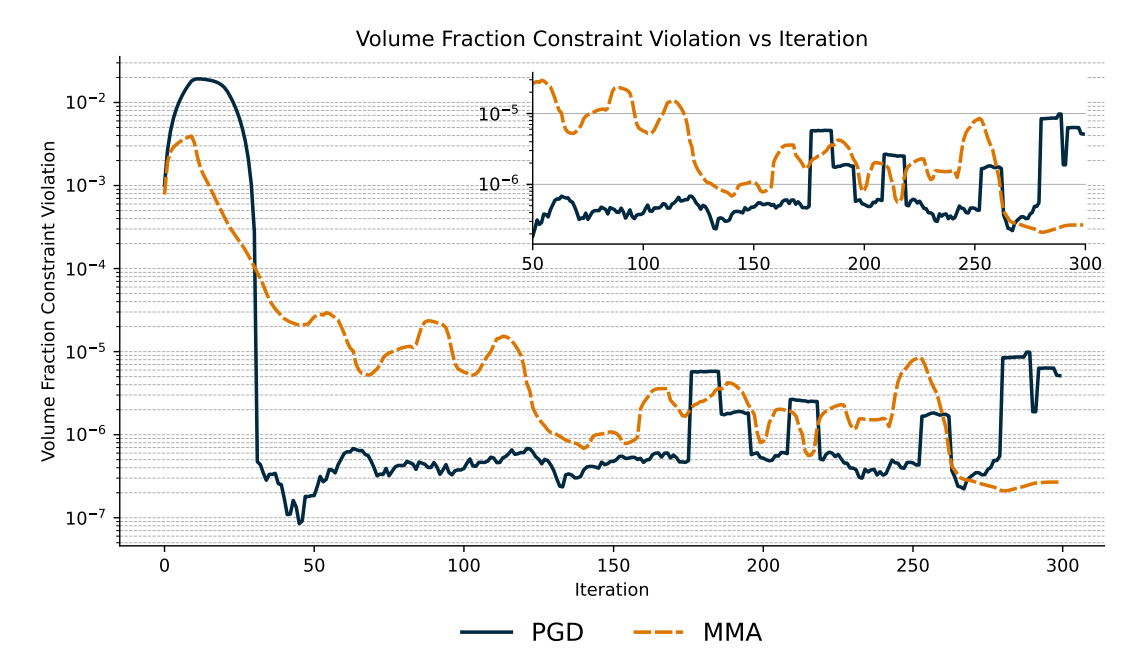


Fig. A65: The value of the constraint violation (volume constraint) at each iteration for all solvers. The plots show a 10-iteration moving average to remove noise and make the plots easier to follow. The inset plot provides a rescaled plot for the same axes after 50 iterations, where solvers have stabilized and the plot is scaled more suitably.

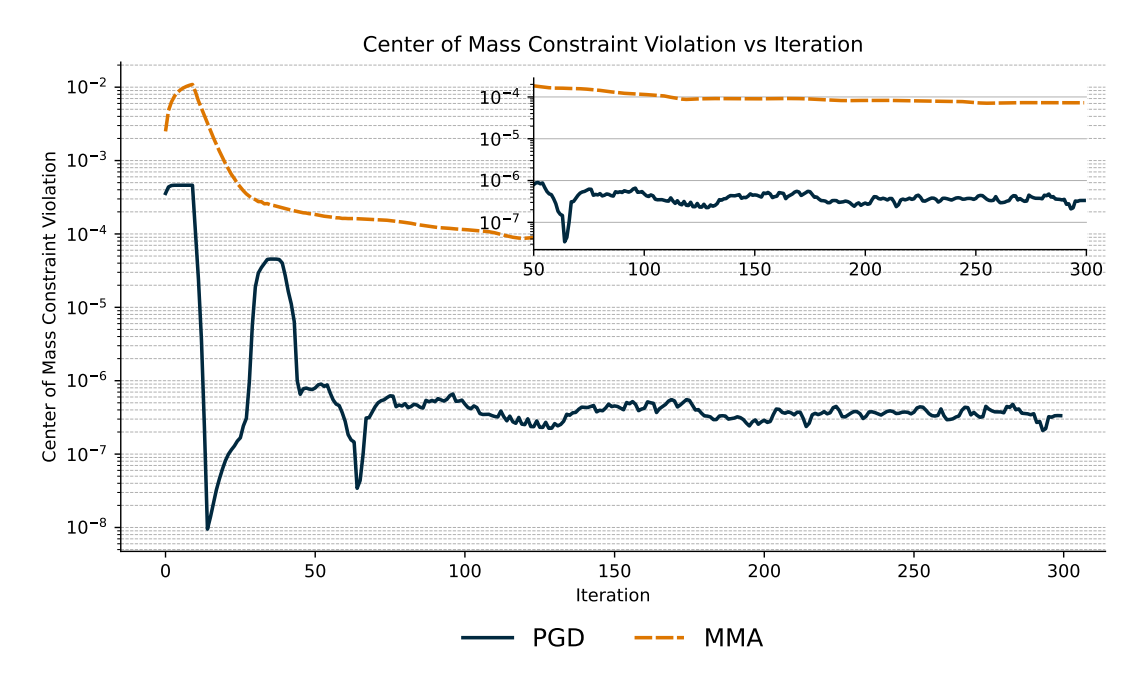


Fig. A66: The value of the constraint violation (center of distance deviation) at each iteration for all solvers. The plots show a 10-iteration moving average to remove noise and make the plots easier to follow. The inset plot provides a rescaled plot for the same axes after 50 iterations, where solvers have stabilized and the plot is scaled more suitably.

Fine Mesh Results

Here we provide figures for the results of running each optimizer for the coarse 512×256 mesh.

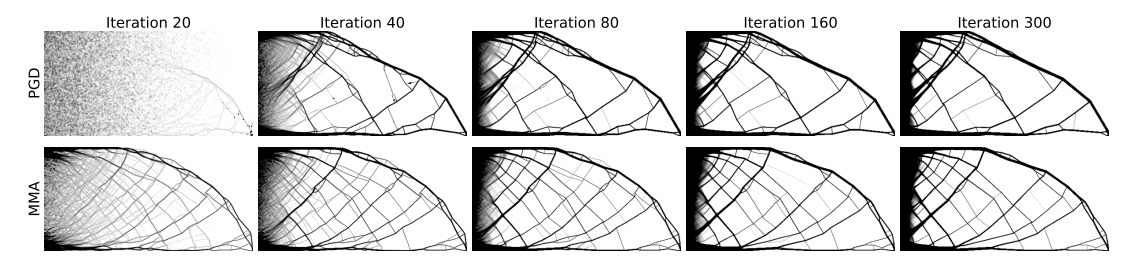


Fig. A67: The designs each optimizer produces at five log-spaced iterations. Here, we visualize the solutions each optimizer produces for the volume & weight constrained minimum compliance problem on the cantilever beam problem with a volume fraction target of 0.2.

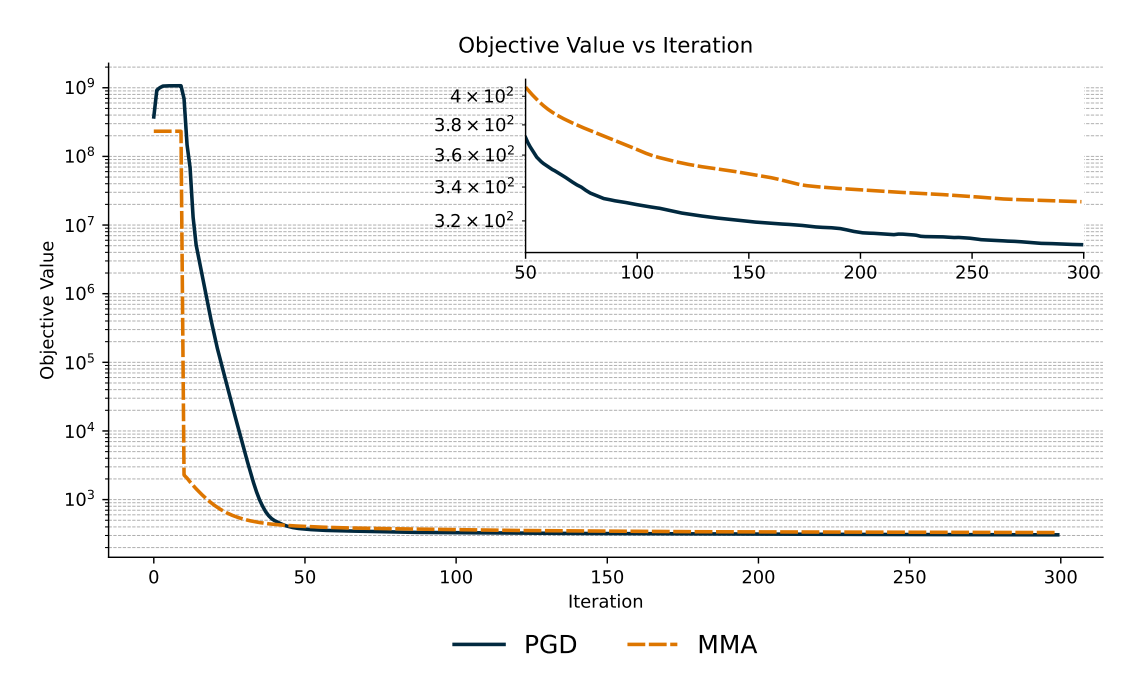


Fig. A68: The value of the objective function measured at each iteration for all solvers. The plots show a 10-iteration moving average to remove noise and make the plots easier to follow. The inset plot provides a rescaled plot for the same axes after 50 iterations, where solvers have stabilized and the plot is scaled more suitably.

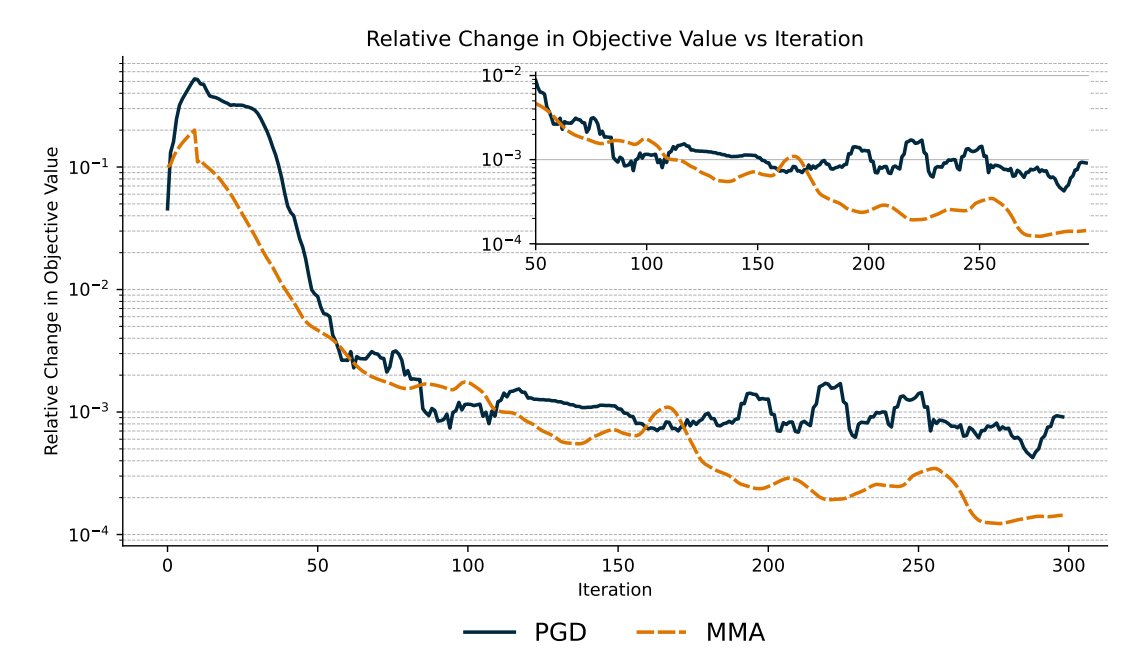


Fig. A69: The value of the relative change in the objective function measured at each iteration for all solvers. The plots show a 10-iteration moving average to remove noise and make the plots easier to follow. The inset plot provides a rescaled plot for the same axes after 50 iterations, where solvers have stabilized and the plot is scaled more suitably.

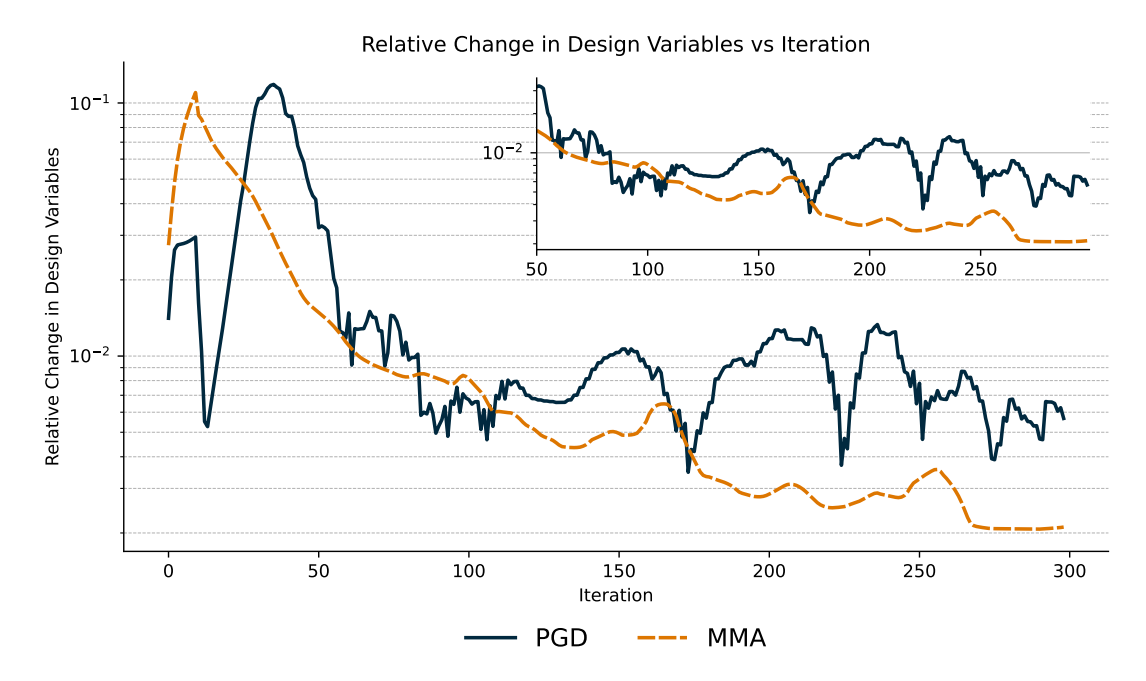


Fig. A70: The value of the relative change in the design variable norm measured at each iteration for all solvers. The plots show a 10-iteration moving average to remove noise and make the plots easier to follow. The inset plot provides a rescaled plot for the same axes after 50 iterations, where solvers have stabilized and the plot is scaled more suitably.

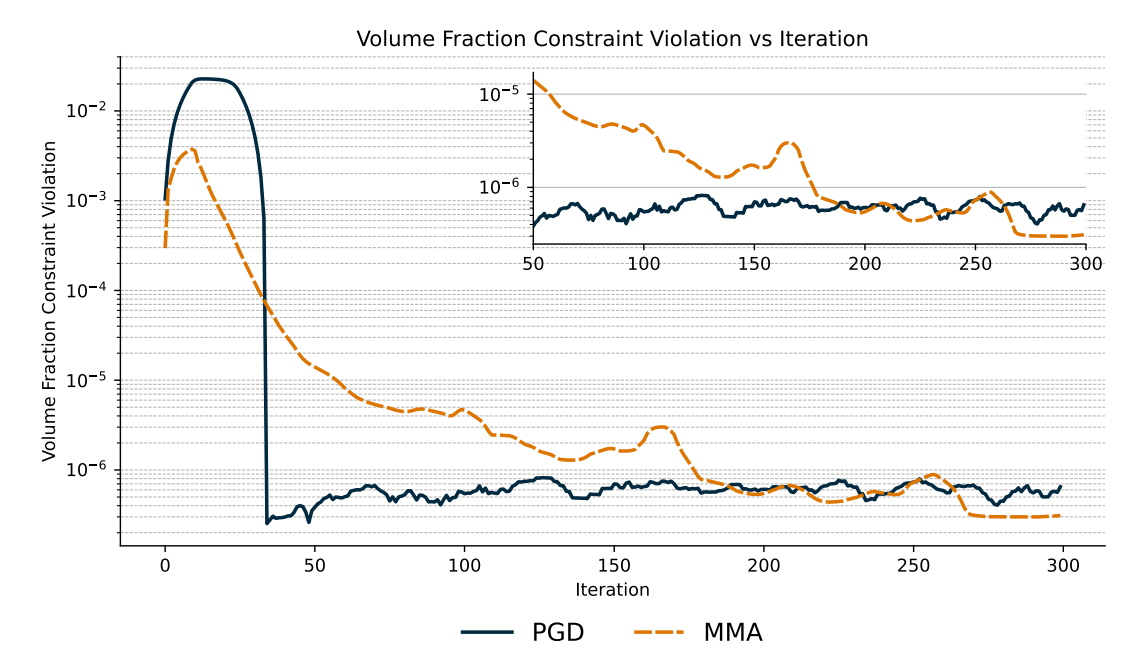


Fig. A71: The value of the constraint violation (volume constraint) at each iteration for all solvers. The plots show a 10-iteration moving average to remove noise and make the plots easier to follow. The inset plot provides a rescaled plot for the same axes after 50 iterations, where solvers have stabilized and the plot is scaled more suitably.

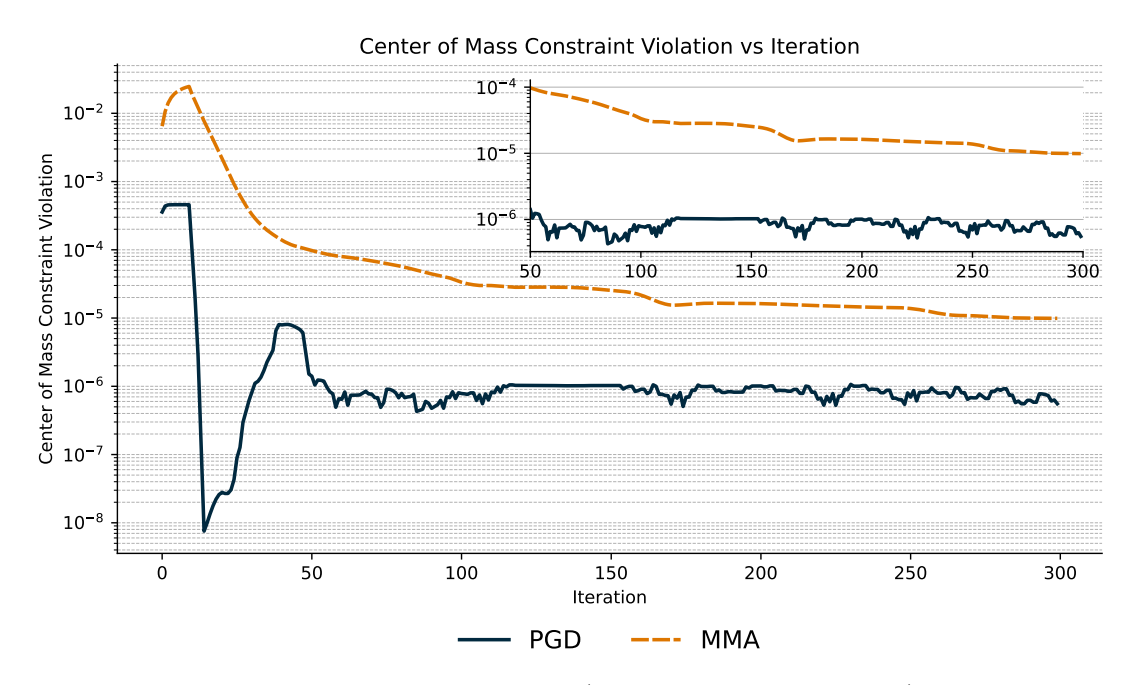


Fig. A72: The value of the constraint violation (center of distance deviation) at each iteration for all solvers. The plots show a 10-iteration moving average to remove noise and make the plots easier to follow. The inset plot provides a rescaled plot for the same axes after 50 iterations, where solvers have stabilized and the plot is scaled more suitably.